Numerical Investigation of the Effects of Split Winglet on Aerodynamic Performance of Horizontal Axis Wind Turbine: A Case of Adama I Wind Turbine

Amlaku Birara Admasu

A Thesis Submitted to the Department of Mechanical Engineering,

School of Mechanical, Chemical and Materials Engineering

Presented in Partial Fulfilment of the Requirement for the Degree of Master of Science in Thermal Engineering

Office of Graduate Studies

Adama Science and Technology University

July, 2024

Adama, Ethiopia

Numerical Investigation of the Effects of Split Winglet on Aerodynamic Performance of Horizontal Axis Wind Turbine: A Case of Adama I Wind Turbine

Amlaku Birara Admasu

Advisor: Dr. Addisu Bekele

Associate Professor in Thermal Engineering

A Thesis Submitted to the Department of Mechanical Engineering,

School of Mechanical, Chemical and Materials Engineering

Presented in Partial Fulfilment of the Requirement for the Degree of Master of Science in Thermal Engineering

Office of Graduate Studies

Adama Science and Technology University

July, 2024

Adama, Ethiopia

Declaration

I hereby declare that this Master Thesis entitled “Numerical Investigation of the Effects of Split Winglet on Aerodynamic Performance of Horizontal Axis Wind Turbine: A Case of Adama I Wind Turbine” is my original work. That is, it has not been submitted for the award of any academic degree, diploma or certificate in any other university. All sources of materials that are used for this thesis have been duly acknowledged through citation.

Amlaku Birara Admasu	________________________	________________
Name of student	Signature	Date

Recommendation of Advisor

I, the advisor of this thesis, hereby certify that I have read the revised version of the thesis entitled "Numerical Investigation of the Effects of Split Winglet on Aerodynamic Performance of Horizontal Axis Wind Turbine: A Case of Adama I Wind Turbine" prepared under my guidance by Amlaku Birara Admasu submitted in partial fulfilment of the requirements for the degree of Master of Science in Thermal Engineering. Therefore, I recommend the submission of revised version of the thesis to the department following the applicable procedures.

Dr. Addisu Bekele	________________________	________________
Advisor	Signature	Date

Approval Page

I, the advisor of the thesis entitled "Numerical Investigation of the Effects of Split Winglet on Aerodynamic Performance of Horizontal Axis Wind Turbine: A Case of Adama I Wind Turbine" and developed by Amlaku Birara Admasu, hereby certify that the recommendation and suggestions made by the board of examiners are appropriately incorporated into the final version of the thesis.

Dr. Addisu Bekele	____________________	______________
Advisor	Signature	Date

We, the undersigned, members of the Board of Reviewers of the thesis by Amlaku Birara Admasu have read and evaluated the thesis entitled "Numerical Investigation of the Effects of Split Winglet on Aerodynamic Performance of Horizontal Axis Wind Turbine: A Case of Adama I Wind Turbine" and examined the candidate during open defense. This is, therefore, to certify that the thesis is accepted for partial fulfilment of the requirement of the degree of Master of Science in Thermal Engineering.

__________________________	______________	_____________
Chairperson	Signature	Date
__________________________	______________	_____________
Internal Examiner	Signature	Date
__________________________	______________	_____________
External Examiner	Signature	Date

Final approval and acceptance of the thesis is contingent upon submission of its final copy to the Office of Postgraduate Studies (OPGS) through the Department Graduate Council (DGC) and School Graduate Committee (SGC).

__________________________	______________	_____________
Department Head	Signature	Date
__________________________	______________	_____________
School Dean	Signature	Date
__________________________	______________	_____________
Office of Postgraduate Studies, Dean	Signature	Date

ACKNOWLEDGEMENT

First and foremost, I would like to express my deepest gratitude for the Almighty God, whom have giving me strength and keeps me healthy. Also, I would like to give my genuine gratitude to my advisor Dr. Addisu Bekele for his abetter guidance and support in compilation of this study. His guidance helps me to prepare a good research work, especially his direction how researches are done and the way how I should see things in thesis work. I am also grateful to Adama Science and Technology University for give me this golden chance to pursuing my study in Master program. Lastly, I am very thankful for my family and friends for their motivation and advices.

TABLE OF CONTENTS

LIST OF TABLES

LIST OF FIGURES

ACRONYM

AC	Alternating Current
AOA	Angle of attack
BEM	Blade Momentum Method
CFD	Computational Fluid Dynamics
CL	Lift Coefficient
CD	Drag Coefficient
DC	Direct Current
DNS	Direct Numerical Simulation
EEP	Ethiopian Electric Power
HAWT	Horizontal Axis Wind Turbine
k-ε	Turbulence Model
k-ω	Turbulence Model
LES	Large Eddy Simulation
MW	Mega Watt
NACA	National Advisory Committee of Aeronautics
NREL	National Renewable Energy Laboratory
N-S	Navier-Stokes
PS	Pressure Side of Blade
RANS	Reynolds-average Navier-Stokes
SIMPLE	Semi-Implicit Method for Pressure-Linked Equations
SS	Suction Side of Blade
SST	Shear Stress Transport
S810	S-series airfoil profile
S813	S-series airfoil profile
S820	S-series airfoil profile
WPP	Wind Power Plant
WTGS	Wind Turbine Generator System
W-1	Winglet-1
W-2	Winglet-2
W-3	Winglet-3
W-4	Winglet-4
W-5	Winglet-5
W-6	Winglet-6

SYMBOLS

A	Area	p	Pressure
α	Angle of attack	∇^2	Laplacian operator
B	Number of blades	S_m	Source term
β	Blade twist angle	μ	Dynamic viscosity
β_{root}	Blade twist at max. chord	ρ	Density
c	Chord length	$\tilde{G}_k$	Generation of *k*
C_{opt}	Optimum chord length	G_ω	Generation of *ω*
C_{root}	Maximum root chord length	Γ_k	Effective diffusivity of *k*
C_l	Lift coefficient	Γ_ω	Effective diffusivity of *ω*
L	Blade length	Y_k	Dissipation of *k*
Ω_r	Rated rotational speed	Y_ω	Dissipation of *ω*
R	Radius of rotor	D_ω	Cross-diffusion term
r_i	Radius at span wise location of the blade	P_i	Local static pressure
U	Rated wind speed	P_∞	Free stream static pressure
U_∞	Free stream wind speed		
W	Relative wind speed		
Λ	Tip speed ratio		
ϕ	Angle of relative wind		
V	Velocity vector		
∇	Gradient Operator		
T	Time		

ABSTRACT

This paper explained research which was performed numerically to evaluate the effect of split winglet on the aerodynamic performance of Adama I wind turbine blade. Winglets are used to minimize blade tip vortex and induced drag on the blade at blade tip. The study was hypothesized, addition of split winglet on the conventional turbine blades tip of Adama I wind turbine was going to improve its aerodynamic efficiency or not. The blade design was performed using Blade Element Momentum (BEM). This theory was used to optimize the chord length and twist angle distributions of the blades. A 3D model of the turbine blade without split winglet and with 6 different configurations of split winglet were design on SOLIDWORKS software. These winglets were designed from two different airfoil profiles and three different cant angle, and rest of winglet parameters were same for all winglets. On the designed blades with and without split winglets a rectangular flow domain was constructed to catch the flow around the blade. The flow domain and blade were meshed with a proper mesh size for accurate numerical solutions. A numerical simulation was performed using ANSYS Fluent. This simulation was conducted at different angle of attacks and wind velocities. The aerodynamic performance (lift to drag coefficient ratio) values of the baseline blade and blade with winglets were determined. A comparison on different cant angle and twist angle of winglet had done. The maximum aerodynamic performance was recorded by S813 airfoil profile, 50º cant angle and 10º twist angle winglet at 15 m/s wind speed and 0º angle of attack with 5% lift to drag coefficient ratio improvement than baseline blade.

***Key words**: Angle of Attack, Aerodynamic Performance, Split Winglet, Chord Length, Twist Angle.*

CHAPTER ONE

INTRODUCTION

1.1 Background of the Study

In the past few years, the global energy production shifts from fossil fuel technologies (which are cause for emission of CO_2 and Greenhouse gases) to sustainable alternatives of renewable energy. Renewable energies play great role shifts away from carbon emission to achieve a net zero emission of carbon. Wind energy is one of renewable energies in energy production sector. As per cost effectiveness, despite globally there is a rising of equipment costs and contract prices in wind energy production, the cost of wind energy generation remains lower than fossil fuel alternatives. The current price of natural gas and coal is very high (IEA, 2021).

In Ethiopia the energy infrastructure development plan sector, Ethiopian Electric Power (EEP) plans to generate power from hydropower plant 90%, geothermal energy 6% and wind energy 4% of the countries power supply to ensure more reliable and secure energy supply throughout the country. Ethiopia has an estimated 45,000 MW energy potential from hydropower, 10,000 MW energy potential from Geothermal and 1350 GW energy potential from wind (United Nations Economic Commission for Africa, 2015). From this high wind energy potential Ethiopian Electric Power aims to produce 1190 MW capacity by using the completed and planed wind power plants (WPPs). Adama I WPP, Adama II WPP, Ashegoda WPP and Aysha WPP are fully (the first three) and partially (the fourth one) completed wind power plants with a production Capacity of 51 MW, 153 MW, 120 MW and 300 MW respectively. Also, Messobo WPP, Assela WPP and Debre Birhan WPP with a capacity of 42 MW, 100 MW and 100 MW respectively are planned to build (Hailu & Kumsa, 2021).

Adama I Wind Power Plant is one of Ethiopian wind power plant located about 3.91 km northwest of Adama city, Oromia Region, Ethiopia. The elevation of the wind farm is about 1824m to 1976m above sea level. The power plant is developed by Hydro-China international corporate with Ethiopian Electric Power in 2012. It produces 51 MW energy of electricity from 34 installed GOLDWIND 77/1500 wind turbines of 65m hub height. Each unit has 1.5 MW energy production capacities with a rotor diameter of 76.9 m and 3 numbers of blades. The rotor has cut-in, rated and cut-out wind speeds of 3 m/s, 11m/s and 22 m/s respectively.

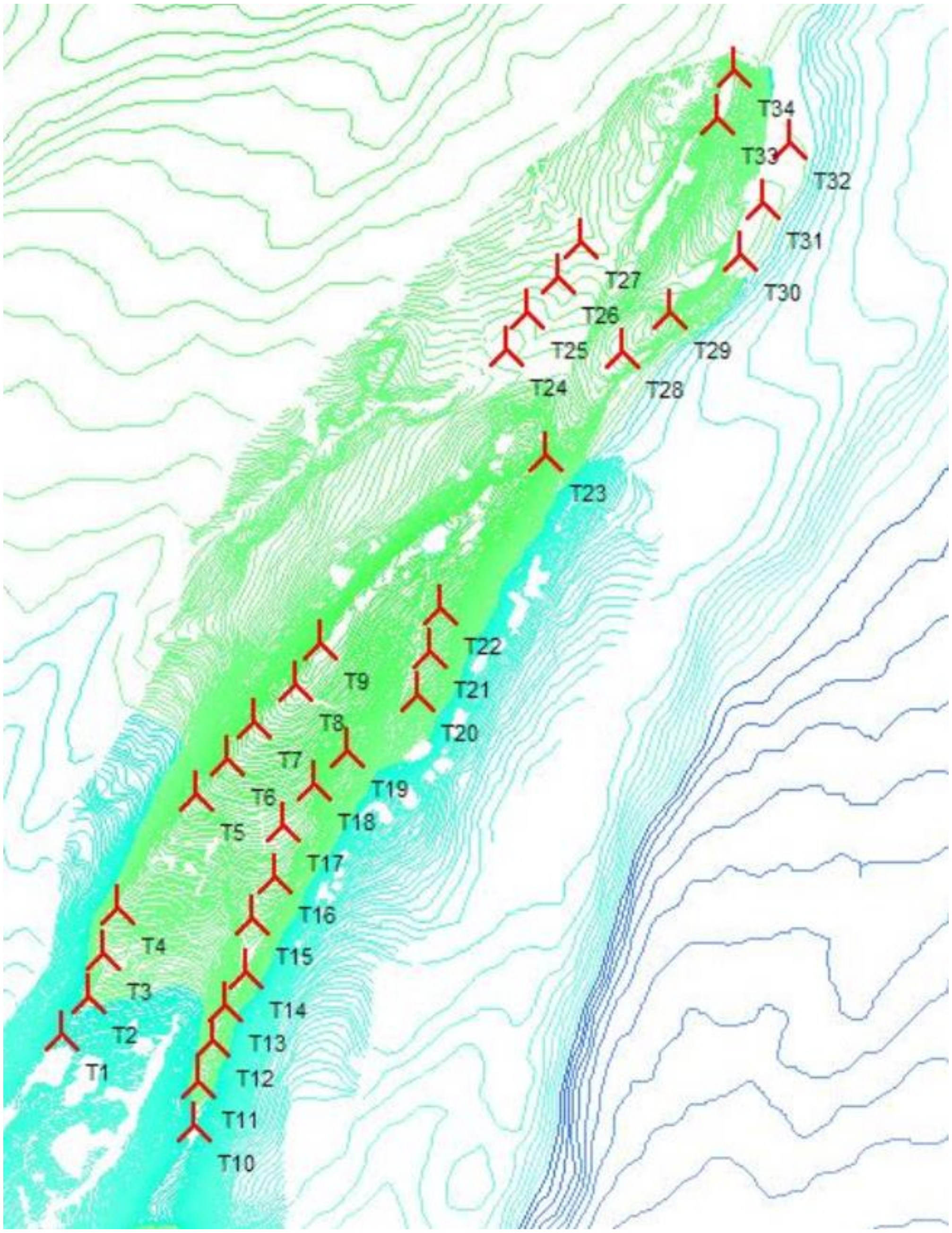

Figure 1.1 WTG layouts of Adama I Wind Farm (Goldwind & TianYuan, 2011).

During generation of electricity from wind energy wind turbines play a great role in harnessing wind energy. One of mostly used wind turbine is a horizontal axis wind turbine (HAWT), which is also used in Adama I WPP. The plant turbine is assembly of blades attached to a hub and the hub is directly attached with the generator (direct drive system). Goldwind 1.5MW wind turbine generator system (WTGS) adopts 3 blades with a suit of pitch system for each blade. These blades are mainly made of four materials including resin, glass cloth, adhesive and core materials

Figure 1.2 Adama I WPP Turbine Blade (Goldwind, 2011).

Winglets

Winglets are a small extension which is adds at the tip of turbine blade with a blade airfoil shape configuration and with its own parametric design. Adding winglet at the blade tip is one of the ways modifying the blade tip geometry to minimize blade tip vortex. Winglets are used to reduce the pressure difference at the blade tip and induced drag on the blade. It also used to improve lift to darg ratio and power coefficient (Khaled et al., 2019). Self-starting velocity of horizontal axis wind turbine is less when optimized winglets are added at its blade tip, which is one of the main advantage of winglets to be performed in low wind speed regimes (Saravanan et al., 2013). The design considerations of winglet include the arrangement, height, cant angle, toe angle, twist angle, sweep angle and curvature radius.

Figure 1.3 Winglet on HAWT blade tip (Weatherguardwind.com, 2020).

1.2 Statement of the Problem

Adama I wind turbine faces a challenge in harnessing wind energy efficiently. As per the plant's wind condition, the production capacity of the plant should be more than the present value. the plant has been working for 12 years so some components efficiency reduced due to aging, in addition this the wind turbine blade of the plant has factors which reduce turbine capacity. Especially the blade experiences unnecessary induced drag at the blade tip. This induced drag is created by a blade tip vortex, which forms at the tip of rotating blade due to the pressure difference between the suction and pressure side of the blade (Sorensen and Shen, 2002). This induced drag is a reason to reduce lift force, power output and efficiency of the turbine and cause vibration and fatigue on the tower.

The first problem that should be resolved should be the induced drag at the tip of the blade. This could be happened by modifying the blade tip of the turbine by adding winglet. Winglet could able to minimize the induced drag and enhance the captured energy, maximizing lift and improve the overall efficiency of the turbine if it was utilized on the blade tip.

1.3 Hypothesis

The hypothesis of this study is basically aimed to know how different parameters of split winglet add effects on the performance of Adama I wind turbine blade. Specifically, it was hypothesised that airfoil profile and cant angle of split winglet parameters are going to improve or not the lift to drag coefficient blade.

It was expected that the efficiency of split winglets varies based on wind speed and angle of attack. This study aimed to identify those influences on the split winglet and characterize the dependence on them.

1.4 General and Specific Objectives

1.4.1 General Objective

The general objective of this study was to evaluate the effect of split winglet on the aerodynamic performance of Adama I wind turbine blade numerically.

1.4.2 Specific Objectives

The general objective was signified through the achievement of the following specific objectives:

- Design wind turbine blade by adding different split winglet geometries and shapes on Adama I wind turbine blade.
- Numerically examine the aerodynamic performance of blade with and without Split winglets.
- Compare the aerodynamic performance of the blade with and without Split winglets.
- Identify a best performed blade with split winglet.
- Evaluate cant angle and twist angles of best performed winglet and set its parameters properly.

1.5 Significance of the Study

This study aimed to significantly influence on the following parts:

- Identifying split winglet that added on baseline blade design, which could able to enhance the aerodynamic efficiency of Adama I wind turbine blade.

- Provides awareness into how split winglet designs perform under different wind speeds and operational parameters.
- Exploring Knowledge about the impact of split winglets to fill gap on wind turbine technology.

1.6 Scope and Limitations of the Study

1.6.1 Scope of the Study

This study was aims to investigate the effect of split winglets on Adama I wind turbine blade by using computational fluid dynamics (CFD). Mainly it includes the effect of airfoil profile and cant angle of split winglet parameters. The scope is summarized on the following key points:

- Investigating on different airfoil profile and cant angle of the split winglet.
- Focused on Adama I Wind Power Plant farm wind condition.
- Comparative analysis of aerodynamic performance (lift to drag coefficient ratio) on the Adama I wind turbine blade with and without split winglet.

1.6.2 Limitations of the Study

Besides to the work which was performed on this study, there was some limitations or works those did not performed here. These are:

- The aero-elastic (deformation and vibration), Wake interface and aero-acoustic (noise) effects of the split winglet was not performed in this study.
- Evaluation of winglet parameters was conducted only on bases of different airfoil profiles, cant angles and twist angles.

CHAPTER TWO

LITERATURE REVIEW

2.1 Introduction

For improving the efficiency of wind energy conversion an optimum design of Horizontal Axis Wind Turbines (HAWTs) was the key research idea that most of research works aimed. By keeping this in mind, I would like to review researcher works on the effect of Winglet on aerodynamic performance of HAWT. This idea brings great enhancement on wind turbine technology. Over the years, researchers have studied how various winglet designs enhance aerodynamic efficiency, reduce drag, and improve power output. This literature review tries to set point of understanding on the idea that researchers develop on the HAWT aerodynamics performance enhancement specifically concern on winglet technology at blade tip of the turbine.

2.2 Overview on Winglet at Blade Tip

Gupta & Amano (2012) performed an investigation on the effect of winglet height and its relation with cant angle on a wind turbine blade numerically using CFD. Four winglet configurations have been selected for the comparison; those are 45° and 90° cant angle with 2% and 4% of rotor radius height for each cant angle. A 20% increment of power output is obtained with 45° cant angle and 4% rotor height as it compared to the straight blade without winglets. As per this study the tip vortex velocity is decreases as cant angle decreases.

Farhan et al. (2019) performed a numerical study on S809 and PSU 94-097 airfoils with winglet by comparing with National Renewable Energy Laboratory (NREL) phase VI rotor as a baseline using CFD. A rectangular and elliptical winglet planform with 5, 10 and 15 cm height and 45° and 90° cant angle were studied to evaluate the effect of the winglet planform on the aerodynamic characteristics of blade. The rectangular planform with S809 airfoil shape, 15cm height and 45° cant angle has 9.8% power improvement. As per the study a rectangular planform has better effect than elliptic one, since the rectangular planform for can able to extract more energy than elliptical planform.

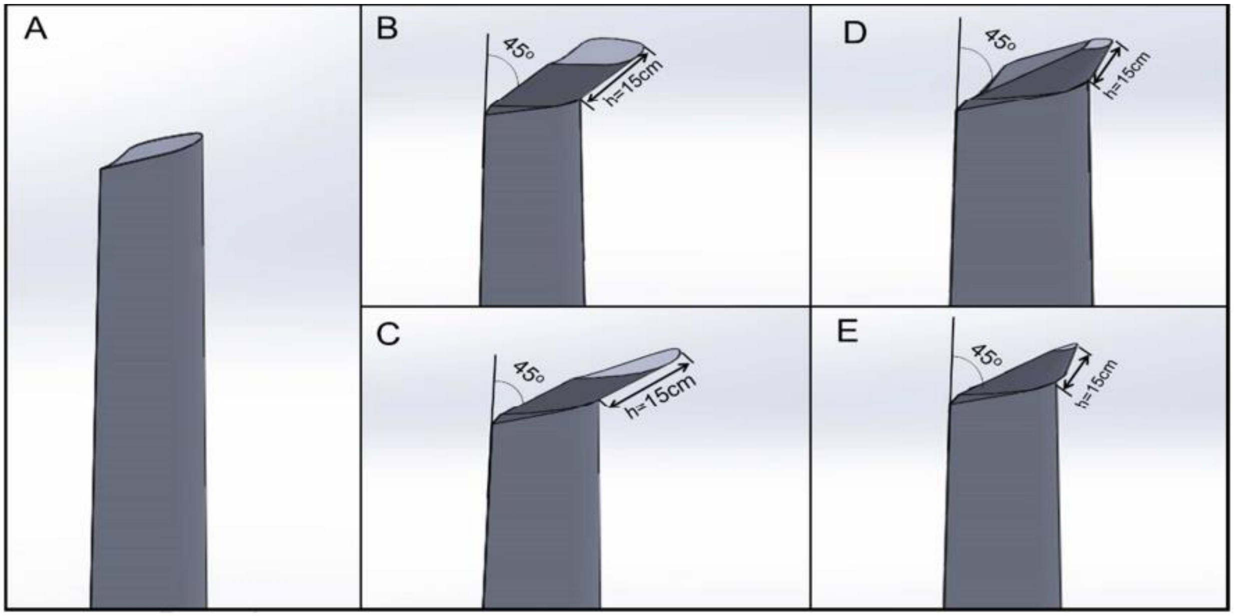

Figure 2.1 A) Baseline blade, B) Rectangular winglet with S809 airfoil, C) Rectangular winglet with PSU 94-097 airfoil, D) Elliptical winglet with S809 airfoil, and E) Elliptical winglet with PSU 94-097 airfoil profile (Farhan et al., 2019).

Khalafallah et al. (2019) performed a numerical analysis on three different types of blade shape using ANSYS Fluent CFD code. For comparison a baseline blade model of a blade profile NREL S826 is used. A winglet added on straight and swept blade shapes to the suction side or pressure side of the blade. Each blade has studied for a twist angle of -2°, 2°, and 10° with different cant angles of 20°, 40°, and 60°. An increasing of power coefficient by 1.75% on a straight blade get for winglet pointing to suction side with a cant angle of 60° and a twist angle of 2°. Also, an increasing of power coefficient by 4.39% on a downward swept blade get for winglet pointing to pressure side with a cant angle of 40° and a twist angle of 10°.

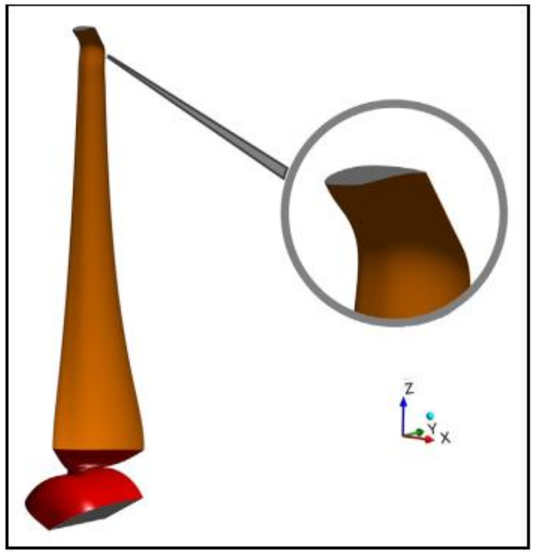

Figure 2.2 Blade with a pressure side winglet with 40° and 10º cant and twist angles (Khalafallah et al., 2019).

Mourad et al. (2020) evaluated the effect of height and toe angle, which is the angle of attack between tangential velocity component and winglet profile, of winglets at 90º cant angle using CFD. The winglet height had been taken 0.8%, 2%, 4% and 8% of rotor radius. For the same tip speed ratio values 0.8% r/R winglet height have best effect on power coefficient than the others, indeed for tip speed ratio value of 6 and 7 the power coefficient value of 4% and 8% r/R winglet height shows decreasing value from the baseline rotor.

The toe angle effect studied at 0º, 10º, 20º and 30º for upwind and downwind winglets at a height of 0.8% r/R values. Upwind winglets show best improvement at 20º toe angle with 2 - 6% and 4.6 - 9.8% values of power coefficient and thrust coefficient respectively. Further increase of toe angle does not improve the values of power coefficient. On this study they reported a downwind winglet configuration does not improve any efficiency (Mourad et al., 2020).

Kulak et al. (2020) conducted an experimental and CFD study on small wind turbine to explore the influence of winglets. The experiment conducted on a height of 4% of rotor radius towards suction side and 3%, 4%, and 5% of rotor radius towards pressure side winglets to compare with baseline blade. An increase in power coefficient of 35% is recorded in the experiment. On the other hand, the simulation result shows the winglet fail to improve the efficiency.

Khan and Islam (2021) conducted a computational and experimental study on a small horizontal axis wind turbine with circular arc blade section (CABS) to evaluate its the performance improvement with upstream and downstream winglet configuration. An improvement of power coefficient by 7.91% for upstream and 12.1% for downstream winglets from experiment; also, 9.79% for upstream and 14.36% for downstream winglets from computational studies were recorded. Downstream winglets improve both power and thrust coefficients than upstream winglets for the same winglet height and cant angle.

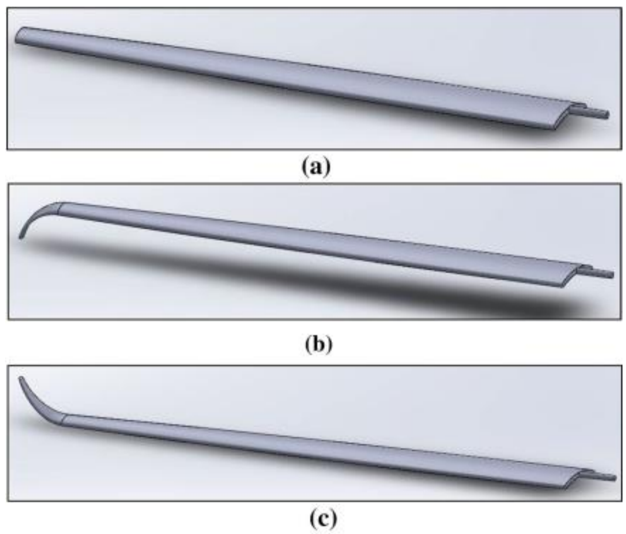

Figure 2.3 a) Blade with CABS profile, b) blade with pressure side winglet, and c) blade with suction side winglet (Khan and Islam, 2021).

Aravindkumar et al. (2021) performed a numerical analysis on a small horizontal axis wind turbine with NACA5514 airfoil shape by using BEM to optimize cant angle of winglet. A cant angle of 30^{o}, 40^{o}, 60^{o}, and 90^{o} used for the study to see the influence on power coefficient. As per the analysis a winglet with 90o cant angle produce more power than the other winglet compared to baseline blade. It gave 13% power improvement.

Pillai and Harikumar (2021) performed a numerical investigation on a wind turbine blade to find the change in lift coefficient to drag coefficient ratio due to winglets. The study aims to get the optimum winglet height and cant angle those able to give maximum result. A blade with NACA-4412 airfoil shape of 3m, 5m, and 7m length used for the study. For the 3m blade an aerodynamic efficiency (Cl/Cd) improvement 14 and 13.84 found with an optimum cant angle of 50^{o} and winglet height of 0.8m. Also, for 5m and 7m blade a maximum aerodynamic efficiency get at height of 1.3m and 1.8m respectively.

Verma et al. (2021) performed a numerical study by adding winglet on NREL phase VI horizontal axis wind turbine to check the aerodynamic performance improvement and the turbulence effect and structural response of the blade. The winglet has 30º sweep angle, 4% of R height and 20º cant angle with symmetric NACA 0018 airfoil. The output power of the turbine improved by winglets tip blade compared to baseline blade from 4.2% to 25% at different wind speed. Also, as the turbulence intensity increased by 10 times, The torque generation is reduced by 11% and 8.54% for a baseline blade and blade with winglet, respectively.

Dejene et al. (2023) numerically investigate the effects of S809 airfoil profile winglet on NREL Phase VI wind turbine using CFD. The study is conducted by adjusting the blade with 50 mm linear extension, 70 mm winglet length and 30º, 45º, and 60º cant angle and arc angle. With the wind speed of 5 to 13 m/s there is an average of 5.37% to 9.97% power output improvement compared to benchmark blade. Also, an axial thrust force is improved by 5% to 11.84% with winglet at wind speed 5 to 13 m/s as it compared with benchmark blade.

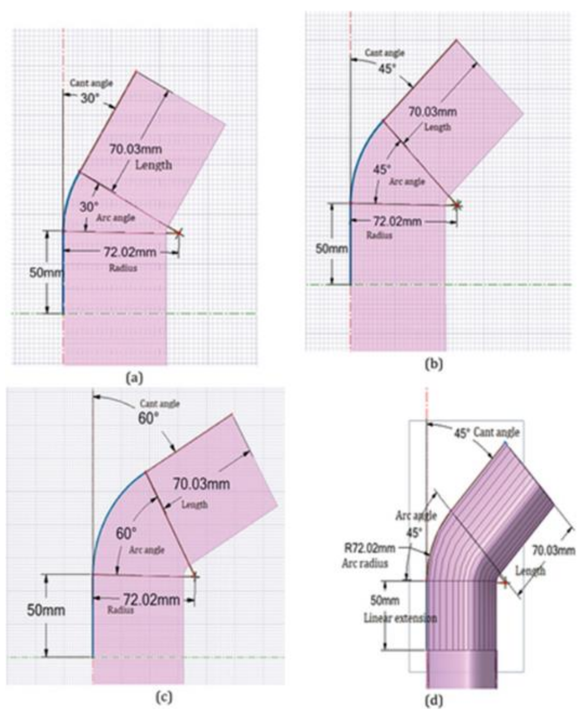

Figure 2.4 Sectional views of winglets at (a) 30º, (b) 45º, (c) 60° cant and arc angles, (d) isometric view with 45º cant and arc angle (Dejene et al., 2023).

Abdelghany et al. (2023) numerically examines the effect of adding bended winglet at the tip of HAWT blade using ANSYS Fluent. The winglets were designed at 90^o cant angle and 0.008R to 0.08R winglet height. An aerodynamic comparison of lift to drag coefficient ratio, power coefficient and trust force had been done. An improvement of lift to drag coefficient ratio, power and trust force at 0.042R winglet height recorded as 11.6%, 6.9% and 14.86% respectively.

Dejene et al. (2024) Numerically examines advantages of using winglet design with sharp and smooth bent configurations and how cant angle and length of winglet affects power production of NREL phase VI blade. They also evaluate the effects of simple linear extension and sharp bent with arced winglet planform. A cant angle 15^o to 90^o had been tested and for sharp bent winglets maximum power was recorded at 45^o cant angle and for smooth bent winglets the maximum power value was recorded at 30^o cant angle. As smooth bent compared with sharp bent, the smooth bent performed better than sharp bent. A power augmentation of 7.07% to 18.37% with winglets compared to benchmark blade.

2.3 Overview of Split Winglets

Zhu et al. (2016) investigated the effect of direction of the winglet tip, those winglet directions were towards suction side, pressure side and both pressure and suctions side (split winglet) on NACA 63-812 blade shape profile using numerical method. For all winglet configurations the value of height, curvature radius, sweep angle and cant angle is 2.5%R, 1.2%R, 45^o and 90^o respectively. At different pitch angle and tip speed ratio the split winglet configuration produces more power than single winglets. The split winglet has maximum power improved value of 3.96% more as compared to the baseline blade.

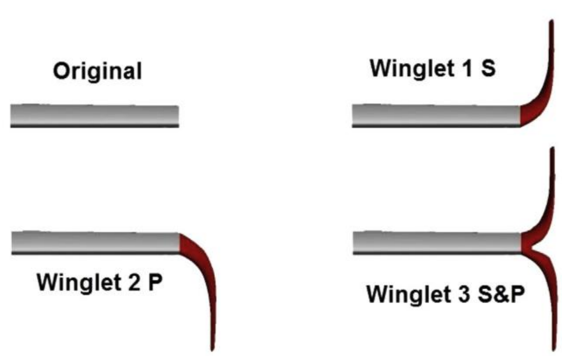

Figure 2.5 Single and Split winglet models (Zhu et al., 2016).

Sy et al. (2020) conducted a numerical study on NREL S809 airfoil section using CFD. The study was tested by modifying tip of wind turbine blade to single winglet and split winglet. The study shows an increasing of power output by 1.23% and 2.53% with winglet and split winglet respectively, when they compared with the extended blade. This shows a blade with split winglet has better power performance than single winglet. The reason that the split winglet shows better performance than single winglet is that split winglet can able to generate additional lift than the single one.

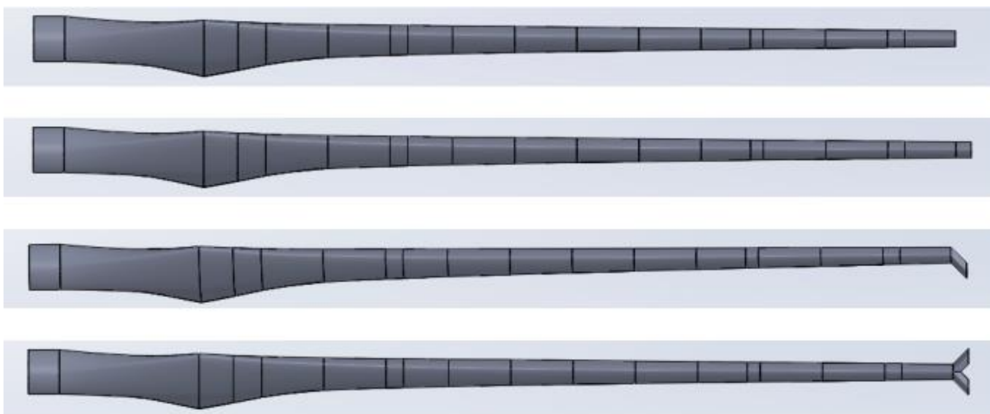

Figure 2.6 Top to bottom: baseline blade, a blade with 1.5% extension, a blade with 45° cant angle suction side winglet and blade with 45° cant angle split winglet.(Sy et al., 2020).

Zhang et al. (2023) conducted a numerical on NREL Phase VI horizontal axis wind turbine to investigate the performance improvement of the turbine by using S809 airfoil shape bent winglet. The study is conducted on a single winglet bend towards suction and pressure side, v shaped winglet and bent winglet. An improvement of 12.1%, 11.2%, and 14.1% had been recorded for single winglet, v shaped winglet and bent winglet respectively. The performance improvement of bent winglet is better than the others.

Mumu et al. (2023) experimentally investigates the effect of symmetrical an asymmetrical split winglets on a circular arc blade section HAWT blade tip at different tip speed ratios and pitch angles. A torque coefficient analysis was done to compare the aerodynamic effect of split winglets at 50° cant angle and 6% of rotor radius. A maximum torque improvement of 9.81% by symmetrical split winglet and 7.27% by asymmetrical split winglets at 2° pitch angle and tip speed ratio value of 4 recorded. Based on these results a symmetrical split tip winglet was more advantageous compared to the baseline blade.

2.4 Literature Summary

These literature reviews can be summarized in table as follows.

Table 1. Literature Summary

Reference	**Airfoil shape**	**Method**	**Dir.**	**Design variables**	**Obj.**	**Improvement**
Gupta and Amano (2012)	NACA 4412	CFD	SS	Height and cant angle	Power	20%
Zhu et al. (2016)	NACA 63-812	CFD	SS, PS and SW	Comparing winglet and SW with same design variables	Power	3.96%
Farhan et al. (2019)	S809 and PSU 94-097	CFD	SS	Planform, height and cant angle	Power	9.8%
Khalafallah et al. (2019)	NREL S826	CFD	SS & PS	Cant angle and twist angle	Power	4.39%
Mourad et al. (2020)	SD8000	CFD	SS & PS	Height and toe angle	Power	2% - 6%
Sy et al. (2020)	NREL S809	CFD	SS & SW	Comparing winglet and SW with same design variables	Power	2.53%
Khan and Islam (2021)	CADS	CFD & EXP.	SS & PS	Comparison between SS & PS with same design variables.	Power	14.36%
Aravindkumar et al. (2021)	NACA-5514	BEM	SS	Cant angle optimization	Power	13%

Pillai and Harikumar (2021)	NACA-4412	CFD	SS	Height and cant angle	C_L/C_D	5.15
Verma et al. (2022)	NREL phase VI	CFD	SS	Single design variable	Power	4.2%-25%
Zhang et al. (2023)	NREL S809	CFD	SS, PS & SW	Comparison between different winglet	Power	14.1%
Dejene et al. (2023)	NREL S809	CFD	SS	Cant angle and arc angle	Power	5.37-9.97%
Mumu et al. (2023)	CADS	EXP.	SW	Symmetrical and Asymmetrical SW	Torque	9.81%
Abdelghany et al. (2023)	NACA-4418	CFD	SS	Height	C_L/C_D	11.6%
Dejene et al. (2024)	NREL S809	CFD	SS	Sharp and Smooth bent with cant angle	Power	7.07-18.37%

In the table for the winglet directed toward suction side (SS), pressure side (PS), and split winglet (SW). C_L/C_D for lift to drag coefficient. EXP for experiment.

Based on the reviewed literatures split winglet have better performance than single winglet. This split winglet for wind turbine blade do not get mech attention. In particular, there has not been much researches reported in the literature regarding the effects of varying parameters of the split winglet. On the initial idea of split winglets can improve the aerodynamic performance of wind turbines by decreasing tip vortices and reducing induced drag. Then different parameters of split winglet were studied on Adama I wind turbine blade design parameters and on the site's wind condition.

CHAPTER THREE

MATERIALS AND METHODS

3.1 Introduction

Adama I wind power plant has a Goldwind 1.5MW wind turbine generator system (WTGS). Technical parameters of Adama I wind pawer plant WTGS is shown below in Table 2. The Goldwind 1.5MW WTGS adopts the overall design scheme on synchronization of horizontal axis, three blades, upwind, pitch adjustment, direct drive and permanent magnet synchronous generator. It adopts the pitch-controlled system to control the power. When the wind speed exceeds the rated wind speed, the output of WTGS will be controlled within 1.5MW through the pitch angle changing so as to prevent the overload of generator and converter system. The generator is a multipole permanent magnet synchronous generator of outer rotor structure and the rotor directly connects to the generator rotor.

A variable-speed constant-frequency system adopts the AC-DC-AC converting method, and it changes the low-frequency alternating current sent by the generator into the pulsating direct current (AC/DC) through the rectification, and it outputs stable DC voltage, and then it converts into the alternating current of the same frequency and same phase with the power grid through the DC/AC inversion, at last, it is connected to the grid to transmit the electric energy.

An automatic yaw system of WTGS can determine the direction of WTGS automatically based on the signal provided by the wind vane. When the wind direction changes, the control system will make the WTGS face the wind by the Yaw reducer of the yaw motor drive. The yaw system has a damping control when it works to make the rotation more stable. The hydraulic system is composed of the hydraulic pump, electromagnetic element, accumulator, brake equipment and connection pipelines, and it supplies power for the yaw brake system and the rotor brake system. With a view to different WTGSs, the automatic lubrication system includes the yaw lubrication, centralized lubrication of generator bearing and of pitch bearing. Each lubrication system is mainly composed of the lubricant pump, oil distributor and lubrication pipelines and used for the automatic lubrication at specified locations. The braking system of the complete WTGS adopts the blade feathering to realize the pneumatic brake and reduce the rotation speed of rotor.

The design of nacelle adopts a people-oriented design scheme, and it has a large working space for the operators to carry out inspection and maintenance, meanwhile, it also has the electric lifting device for the conveying of tools and spare parts. The overall WTGS is controlled by PLC and the data is self-collected and processed. The WTGS can operate automatically which can be remote-monitored.

Table 2. Technical parameters of wind turbine generator system (WTGS) (Goldwind, 2011).

WTGS model	GW77/1500kW
Wind turbine class	IEC II A
Rated power	1500kW
Inverter output voltage	620V
Diameter of rotor	76.84m
Swept area	4637.3m^2
Hub height	65m
Rated rotation speed of rotor	17.3 rpm
Rated wind speed	11 m/s
Cut-in wind speed	3 m/s
Cut-out wind speed	22 m/s
Maximum survival wind speed (3 seconds)	59.5 m/s
Maximum allowable maintenance wind speed	11m/s
Operating temperature	21 ℃
Survival temperature of WTGS	-40 ℃ – +50 ℃
Design service life	≥20 years
Lightning protection design standard	IEC61400-24; IEC62305

3.1.1 Baseline Blade

Adama I wind turbine blade was manufactured by LM wind power company. The blade called LM 37.3 P2 blade. In Table 3 below some of blade design parameters of LM37.3 P2 blade are listed.

Table 3. Blade design Parameters

Blade length (exclude root flange)	L	37300 mm	± 37 mm
Maximum root chord length	C_{root}	3097mm	± 20 mm
Blade twist at maximum chord length	β_{root}	14.0 °	± 0.5 °
Airfoil profiles		NACA 634-421	

Rest of the blade design was expressed by finding the value chord length and twist angle of the blade at some specific points through the blade span length. Obtaining chord length and twist angle distribution is based on the tip speed ratio of Adama I wind power plant.

Tip speed ratio can be calculated as:

$$\lambda = \frac{\Omega_r \times R}{U}$$

where: Ω_r = Rated rotational speed (17.3 rpm) = (2π/60) X 17.3 = 1.812 s^{-1}

R = Rotor radius (38.42 m)

U = Rated wind speed (11 m/s)

$$\lambda = \frac{1.812\ s^{-1}\ \times\ 38.42\ m}{11\ m/s} = 6.33$$

For a turbine with B number of blades of at different section wise radius r_i the chord length c and blade twist angle β determined based on the following corelations. Both the chord length and the pitch angle may vary along the blade span. Let the blades be rotating at angular velocity Ω_r and let the wind speed be U_∞, this velocities and relative velocity of them shows in figure 3.2 relative to the blade chord line at random radius r (Burton et al., 2001).

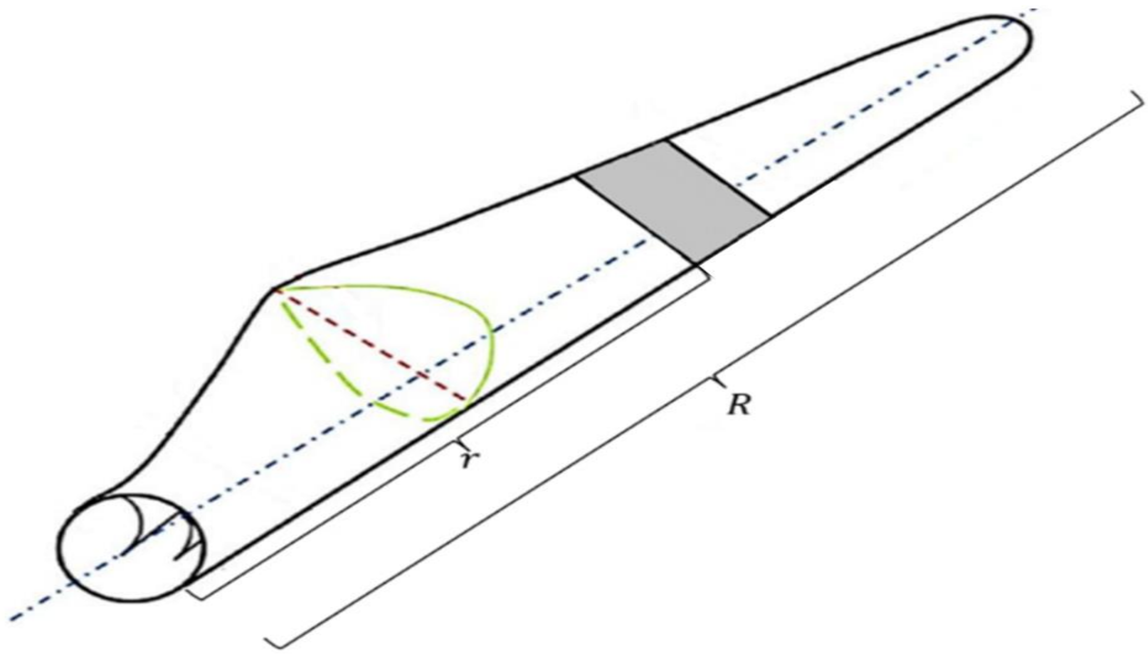

Figure 3.1: Diagram of blade (Contreras et al., 2022).

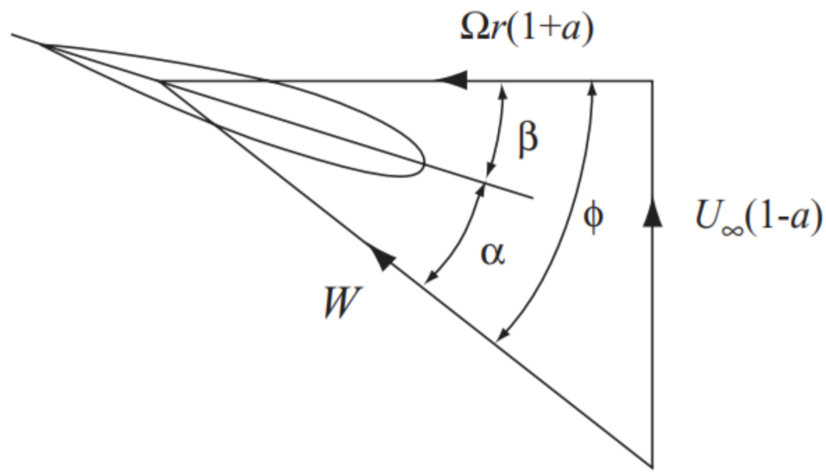

Figure 3.2 Blade Element Velocities and their Angles.

For a tip speed ratio, the blade should be designed to give a maximum possible power output. To get a maximized developed torque value at each blade station, the flow angle (ϕ) of the blade is expressed as below (Burton et al., 2001):

$$\phi = \tan^{-1}\left(\frac{1-\frac{1}{3}}{\lambda\mu_i\left(1+\frac{2}{3\lambda^2{\mu_i}^2}\right)}\right)$$

Where: ϕ = angle of relative wind

$\mu_i = {}^{r_i}/_{R}$,

r_i = radius of blade at any span wise location of the blade

R = rotor radius

Obtaining chord and twist distribution at tip speed ratio of the blade is depends on the flow angle of relative velocity, angle of attack, lift coefficient and numbers of blade as expressed below.

Optimum chord length (Manwell et al., 2009):

$$C_{opt_i} = \left(\frac{4\pi r_i}{BC_l}\right)\tan\phi\sin\phi$$

Blade twist angle:

$$\beta = \phi - \alpha$$

Based on the operating rotor designed tip speed ratio and a constant value of lift coefficient (Appendix-1) blade with Adama I wind turbine blade number (3) the angle of relative wind speed, blade twist angle and optimum chord length of the blade at different locations of blade in span wise length described in Table 4 and in figure 3.4 and 3.5 optimum chord length and optimum blade twist angle respectively. In figure 3.3 the blade 3D model is expressed based on the data calculated from the above equations.

Table 4. Chord length and twist angle distribution

r_i/R	Angle of relative wind in degree (ϕ)	Blade twist angle in degree (β)	Optimum chord length in meter (C_{opt})
0.1822	21.06	14.06	3.097
0.3	16.50	9.5	2.917
0.4	13.41	6.41	2.557
0.5	11.17	4.17	2.211
0.6	9.52	2.52	1.924
0.7	8.28	1.28	1.696
0.8	7.31	0.31	1.509
1	5.91	-1.09	0.4

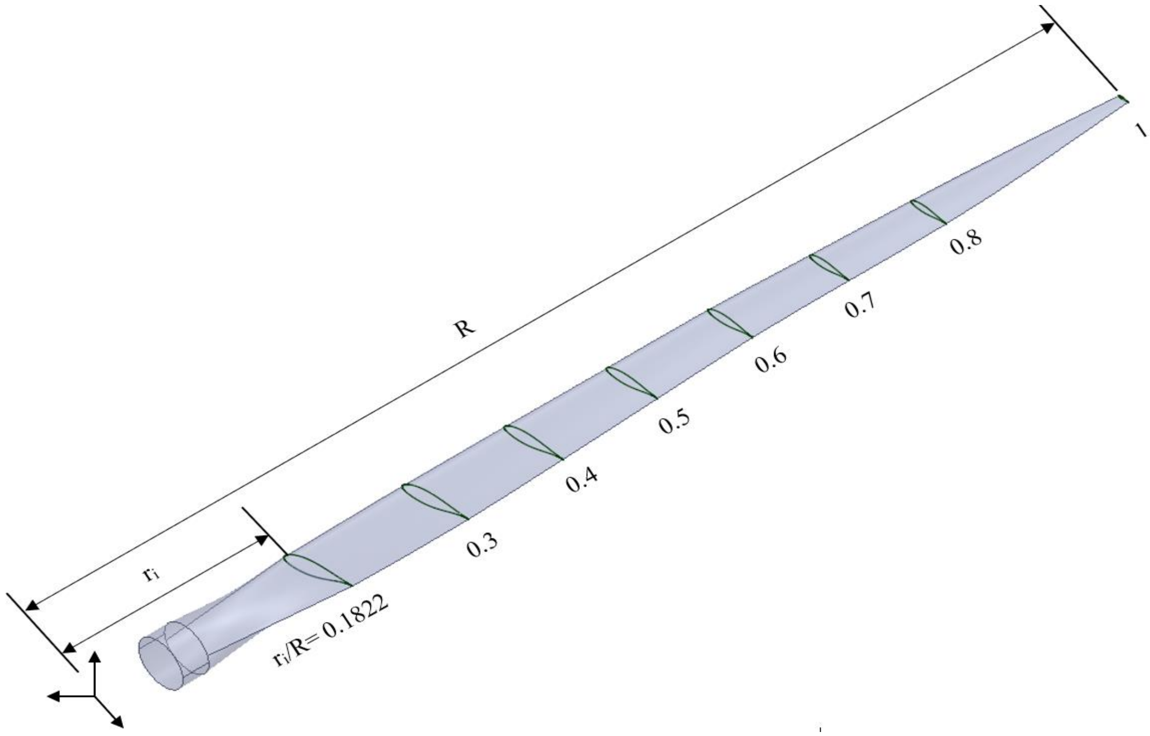

Figure 3.3 Isometric drawing of Baseline blade

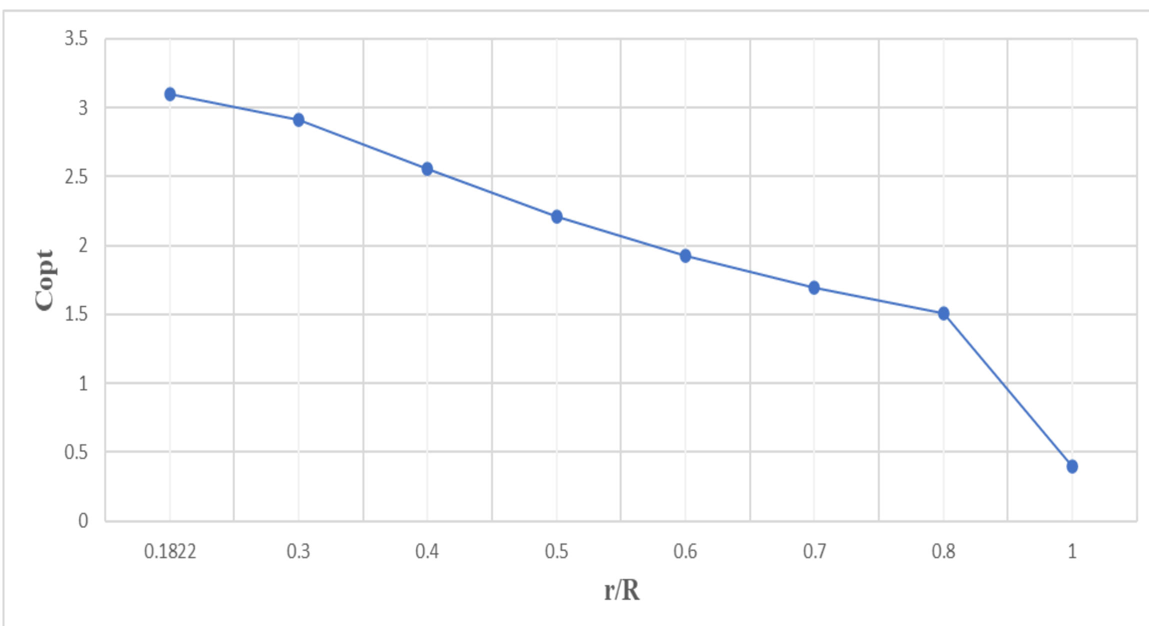

Figure 3.4 Optimum chord length verses span wise length

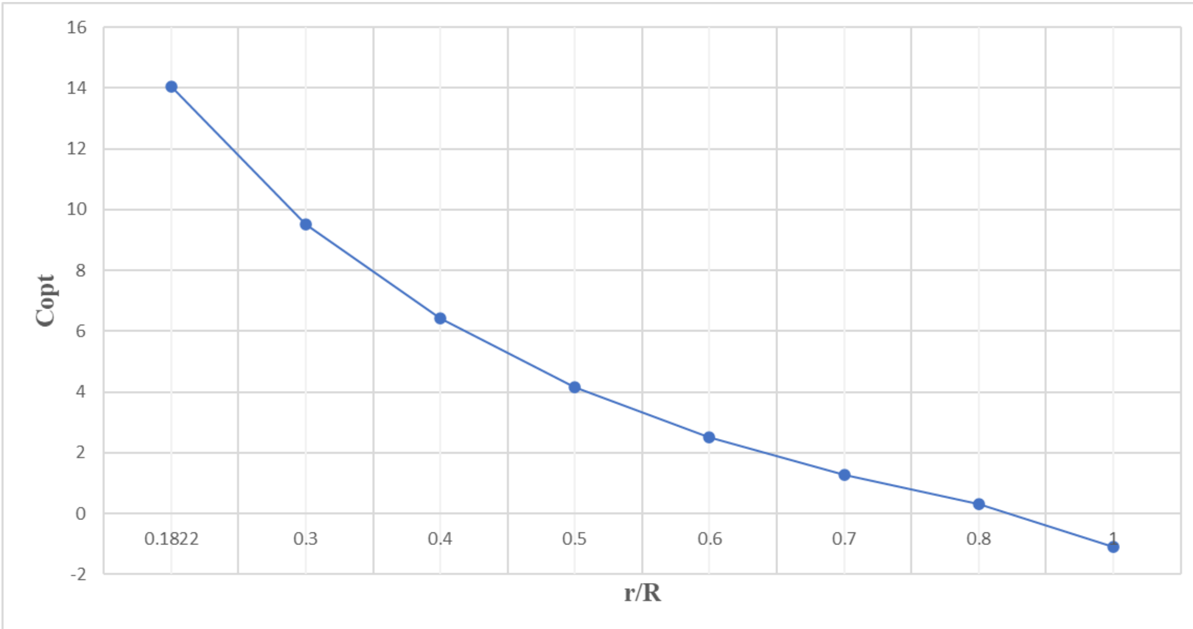

Figure 3.5 Optimum twist angle verses span wise length

3.2 Winglet design

During design of winglet there are so many parameters to be considered, such as airfoil profile, height, cant angle, sweep angle, twist angle, toe angle and curvature radius of the winglet. In this study the airfoil profiles and cant angle of the winglet will be designed in different parameters to select the best performed winglet design. Other winglet parameters keep a fixed value for each different winglet designs.

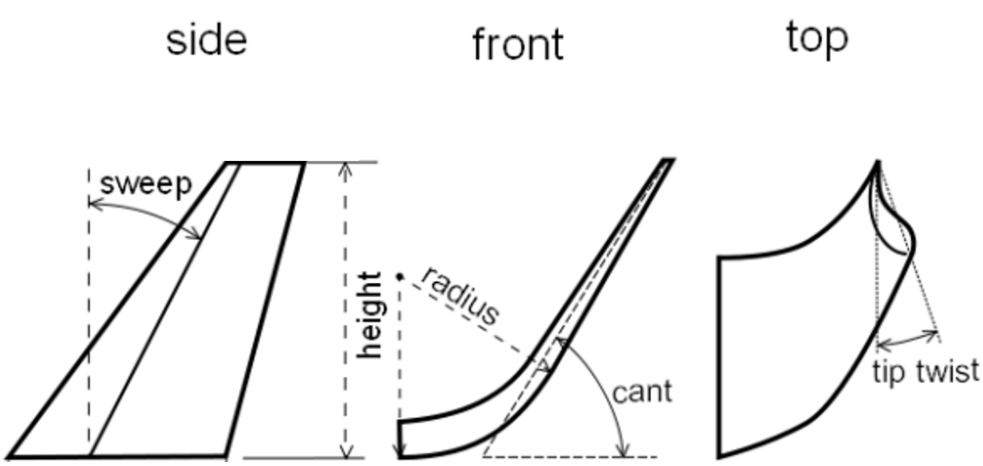

Figure 3.6 Design variables used to define winglet geometry (Weierman & Jacob, 2010).

- **Airfoil profile of winglet**

The power generation of a HAWT is function of different parameters manly number of blades of the rotor, ratio of lift to drag coefficient of the selected airfoil, and tip speed ratio of the rotor. Thus, one of the design goal of a HAWT to maximize the power generation is maximize the lift to drag coefficient ratio (He & Agarwal, 2014).

Over the past years commonly NACA 44XX, NACA 23XXX, NACA 63XXX, and NASA LS(1) series airfoils families have been used for HAWT. This airfoil families suffer an energy loss due to performance degradation from roughness effects results from leading-edge contamination. This loss caused by reduction of maximum lift coefficient of the HAWT along the blade. To maximize the lift coefficient and minimize the loss of the HAWT National Renewable Energy Laboratory (NREL) develop special purpose airfoils. These airfoils are designed to have a maximum lift coefficient. (Tangier & Somers, 1995).

For proper design of the winglet two different airfoils have to be selected. One of the winglet's airfoil profile is similar to the baseline blade, which is a NACA 634-421 airfoil. And the other one should have high lift to drag coefficient value.

From NREL S-series airfoil families S810, S813 and S820 airfoils are recommended for blade tip design (Tangier & Somers, 1995). Based on XFOIL prediction of lift and drag coefficient values, S813 have maximum values of lift to drag coefficient ratio than the others. So, the second one of winglet's airfoil profile is S813. All XFOIL prediction graph is shown in APENDIX.

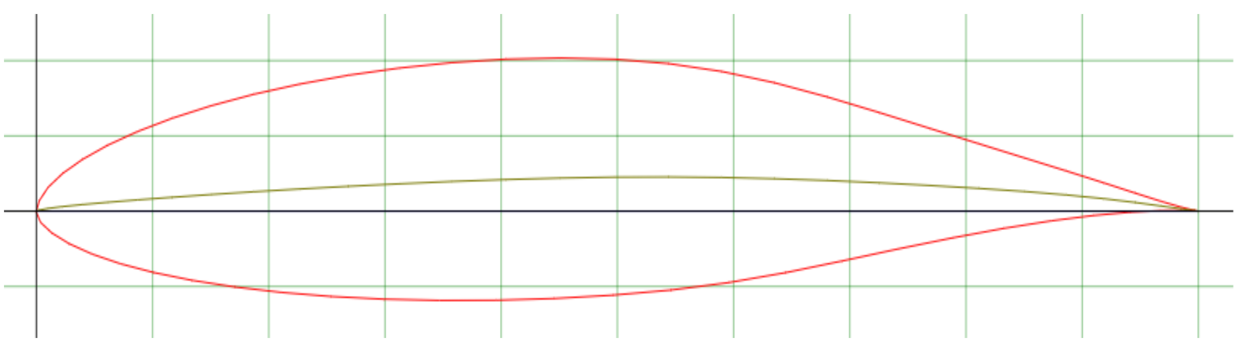

Figure 3.7 S813 airfoil profiles (AirfoilTools.com, 2024).

- **Cant Angle of Winglet**

A cant angle of a winglet is an angle which the winglet is tilted from the horizontal axis to suction side or pressure side of the wind turbine blade. A cant angle of winglets should be properly design to improve the aerodynamic performance of the HAWT. The optimum cant angle is depended on different factors, but the first objective of the study is to reduce the aerodynamic losses caused by the tip vortices.

Different cant angles give different effects on the aerodynamic performance of the HAWT. Besides to the value of cant angle, on which side of the blade (suction or pressure side) the winglet tilted also matters. Winglets tilted to suction side shows more increase in power than winglets tilted to pressure side (Khalafallah et al., 2019). This study is designed a split winglet which tilted both suction and pressure side. For single winglet which, suction side tilted winglets cant angle range of 20^o to 60^o shows an aerodynamic performance improvement than angles which are tilted at 90^o (Farhan et al., 2019; Gupta & Amano, 2012; Khalafallah et al., 2019). Winglets with an angle below 20^o and above 60^o could lead to imbalances between lift and drag forces. Cant angles below 20^o cannot able to reduce vortex sufficiently, while angles above 60^o led to create additional drag force.

Since there are no sufficient studies on how cant angle of split winglets add effects on aerodynamic performance of the blade, split winglets which is tilted at 30^o, 40^o and 50^o of cant angle to both suction and pressure side of the blade are designed.

- **Height of winglet**

The height of a winglet is the vertical distance between the tip of the baseline blade to the tip of tilted winglet. The value of winglet's height should be selected properly. If its value is higher or lower than the optimum value, it may cause aerodynamic performance decrement. The winglet height value described as a ratio of rotor radius. As the winglet height increases the power output also increases and vice versa, but if it exceeds the optimum value the power output decreases (Saravanan et al., 2013). At a ranges of 2%R to 5%R of winglet height values shows better aerodynamic performance than others and the maximum is recorded at 4%R value (Abdelghany et al., 2023; Gupta & Amano, 2012; Kulak et al., 2020; Mourad et al., 2020). This study will be conducted by using winglet heights of 4% values of rotor radius for both suction and pressure side.

Other winglet parameters

In this study the value of sweep angle, toe angle and twist angle of winglet will keep constant value. Sweep angle is the angle between the plane perpendicular to the HAWT blade axis and the line which connects the trilling edge of base and tip of the winglet. When sweep angle value of winglet increases starting from zero the aerodynamic performance decreases (Farhan et al., 2019). This is due to reduction of winglet planform area as sweep angle increases. In order to get the aerodynamic advantage of full winglet area this study will conducted on 0^o sweep angle. Toe angle is the angle at which the winglet is positioned relative to the baseline blade. The value of this angle also keeps 0^o in this study. Twist angle of the winglet keeps 10^o to minimize the drag effect which is created due to the addition of winglet on the baseline blade.

Based on the above discussion in Table 5 there are six different types of wiglet configurations labelled using two different airfoil profiles and three different cant angles with the same parametric values of other winglet parameters.

Table 5. Design parameters of winglets

Winglet name	Airfoil profile	Cant angle (^{o})	Height (%R)	Sweep angle (^{o})	Toe angle (^{o})	Twist angle (^{o})
Winglet 1 (W-1)	NACA 634	30	4	0	0	10
Winglet 2 (W-2)	NACA 634	40	4	0	0	10
Winglet 3 (W-3)	NACA 634	50	4	0	0	10
Winglet 4 (W-4)	S813	30	4	0	0	10
Winglet 5 (W-5)	S813	40	4	0	0	10
Winglet 6 (W-6)	S813	50	4	0	0	10

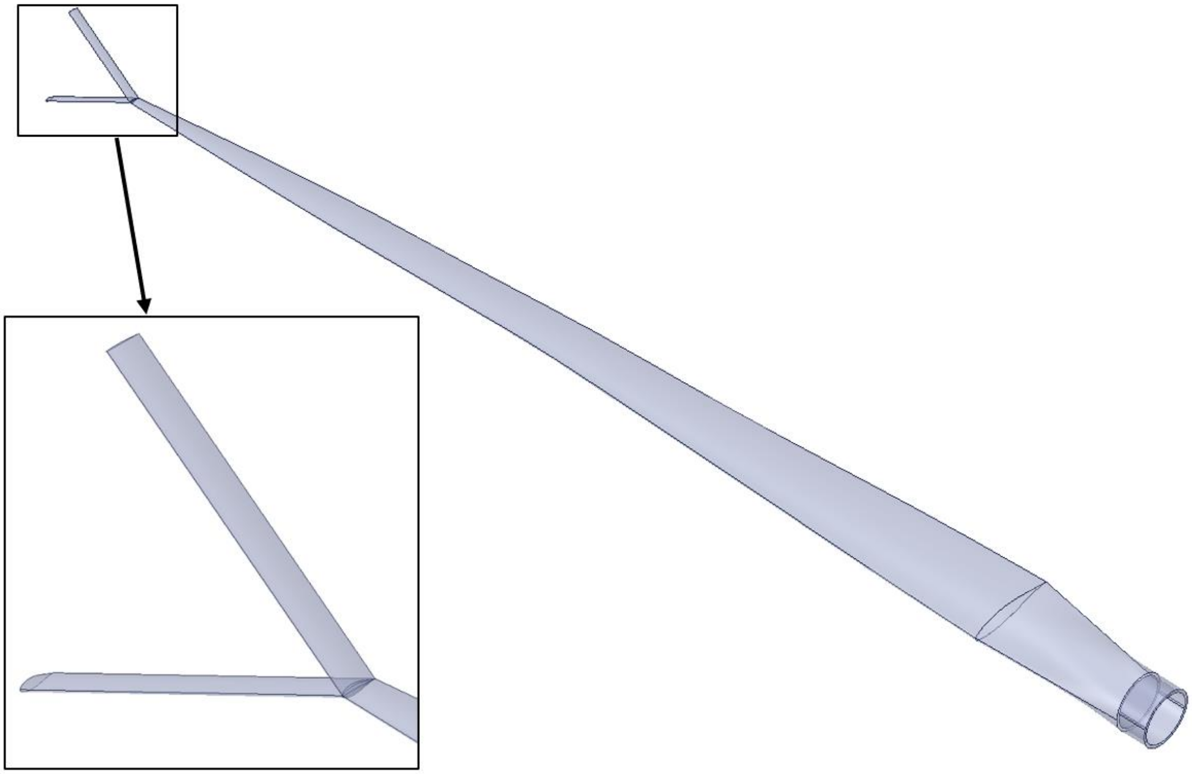

Figure 3.8 Isometric drawing of blade with winglet 1

3.3 Aerodynamics Performance of Wind Turbine Blade

Aerodynamic performance of wind turbine blade can be determine by finding lift to drag coefficient ratio of the blade. The lift to drag coefficient ratio is the key parameter to that determines the efficiency of the wind turbine blade wind energy to rotational mechanical energy (Fikade et al., 2020).

In order to produce power, the wind turbine have to rotated. This rotation if caused by due to the lift force which is applied on turbine blade. the lift force is acts perpendicular to the relative wind direction. The reason that creates this lift force is the existence of pressure difference between pressure and suction side of the blade. In addition to this lift force there is a darg force which is acted parallel to the relative wind direction. This drag force is created due to unnecessary vortex and friction between blowing wind and blade surface (Sayed et al., 2012). The primary goal of this research is maximizing the lift to drag coefficient to maximize the power. The formula for lift coefficient (C_l) and drag coefficient (C_d) could be defined as follows:

$$C_l = \frac{F_l}{1/2\rho {u_\infty}^2 A}$$

$$C_d = \frac{F_d}{1/2\rho {u_\infty}^2 A}$$

Therefore, lift to drag coefficent ratio can be defines as:

$$\text{Lift to drag coefficent ratio} = \frac{C_l}{C_d}$$

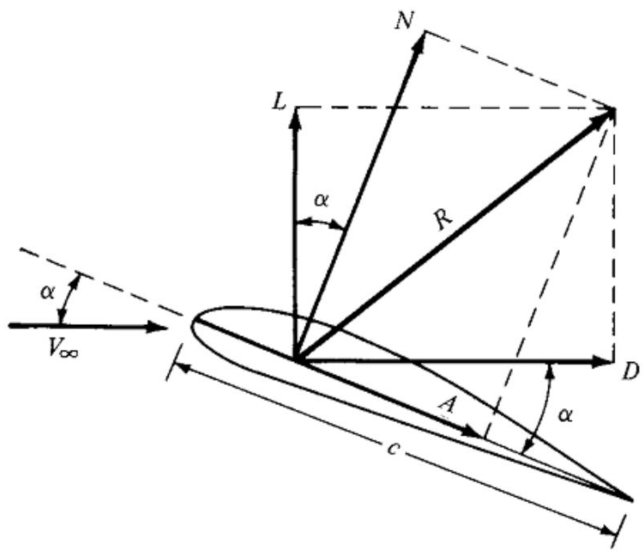

Figure 3.9 Resultant aerodynamic force and its components (Talukder et al., 2016).

In addition to lift and drag coefficients pressure coefficient of the fluid flow could used to demonstrate the aeroynamic performance. This pressure coefficient gives an information how pressure varies at different section of the blade (Dejene, Ancha, et al., 2024; Zhang et al., 2023). For this thesis the formula used to find pressure coefficient was:

$$C_{p_i} = \frac{P_i - P_\infty}{0.5\rho {u_\infty}^2}$$

Where, i stands for the i^th blade section, P_i is the local static pressure, P_∞ is the free stream static pressure, ρ for air density, and u_∞ for the inlet velocity.

3.4 Numerical Performance Analysis

Numerical performance analysis methods are used to determine the power performance, lift and drag forces, trust force and structural integrity of wind turbine blades. To analyse the aerodynamic and structural performance of wind turbine blade computational fluid dynamics (CFD) technique is utilized in numerical performance analysis.

Computational fluid dynamics or CFD analysis is involved in analysis of fluid flow, heat transfer and associated phenomena such as chemical reactions systems by using computational computer simulation. This technique a powerful way, which able to minimize loads in industrial and non-industrial activities (Versteeg & Malalasekera, 2007). One of its application areas is in the analysis and optimization of wind turbine blade performance. CFD have been playing a great role for simulating and studying the flow of air around wind turbine blades. Using this approach the flow filed characteristics, aerodynamic forces, power output, and structural loads experienced by the blades can be explained in detail. The information gathered from CFD are helps for efficient and reliable designs of wind turbines.

3.4.1 Governing Equations

In CFD the mathematical description of the flow of air is based on fundamental conservation lows:

- conservation of mass
- conservation of momentum and
- conservation of energy

The set of equations that describes fluid flow condition is known as the Navier–Stokes equations. Since Adama I wind power plant operational wind velocity is between 3 to 22 m/s implies that Mach number of the plant is below 0.1. For a smaller Mach number (below 0.25), the density can be approximated as constant so the flow considered as incompressible and the conservation of energy can be eliminated from the governing equations. The remaining four equations (conservation of mass and the other three conservation of momentum) are sufficient to find the velocity filed and pressure (Snel, 2003). These equations for a Newtonian fluid can be written as follows (White, 2011):

Continuity equation:

$$\nabla \cdot V = 0$$

Momentum equation:

$$\rho\left(\frac{dV}{dt} + V(\nabla \cdot V)\right) = -\nabla \mathrm{p} + S_m + \mu(\nabla^2 \cdot V)$$

Where: V for velocity vector, ∇ for gradient, t for time, ρ for density, p for pressure, μ for the dynamic viscosity, S_m for the source term and ∇^2 for the Laplacian operator

Even though the equation we used to solve for the flow filed is an incompressible Navier-Stokes equations, it is difficult to solve its non-linear nature. There are different CFD methods to solve the Navier-Stokes equations for fluid flow over blade. The most commonly used methods to solve Navier-Stokes equations are Reynolds-averaged Navier-Stokes (RANS), Large Eddy Simulation (LES) and Direct Numerical Simulation (DNS). From these methods the most computationally expansive method is DNS, since it requires high number of nodes. The LES method could give a more accurate result than RANS, but due to its requirement of a finer mesh than RANS method LES requires a powerful computational Computer (Muiruri et al., 2019). This makes RANS method more preferred method.

The Reynolds-Averaged Navier-Stokes (RANS) equations are a set of equations used in Computational Fluid Dynamics (CFD) to simulate turbulent flows. They are derived by averaging the instantaneous Navier-Stokes equations over time, resulting in a time-averaged flow description. Due to the non-linearity of the equations, those the correlation between velocity components and between pressure and velocity components, the equations are not sufficient to determine the unknowns. The most common practice to determine the unknowns are to propose a turbulence model, which is a relation between main flow terms and the turbulence model corelations (Snel, 2003). The construction of such a model is usually based on some empirical information and a lot of physical intuition. The two equation models (k- ε, k-ω and k-w SST) are most commonly used turbulence models in wind turbine applications. Where k is specific turbulence kinetic energy), ε is the specific dissipation and ω is the specific dissipation rate.

These turbulence models depending on the properties of the blade and boundary conditions of flow model have different prediction capabilities. Due to this, from these turbulence models that give the most accurate CFD prediction should be chosen. The k-ω SST model prediction capacity for aerodynamic behaviour of the wind turbine blade is better than the other two turbulence models (Muiruri et al., 2019).

k-ω SST model

The *k-ω* SST turbulence model is a two-equation eddy-viscosity model developed by Menter, which uses the *k-ω* model in the near wall region and the *k-ε* model in the far field in the free streams. To achieve this, the *k-ε* model is converted into a *k-ω* formulation. This formation makes *k-ω* SST more accurate than both *k-ω* and *k-ε*. For flows like adverse pressure gradient flows, airfoils, transonic shock waves *k-ω* SST is more accurate and reliable than the other *k-ω* models (ANSYS, 2021). Generally, the *k-ω* SST model differ from the standard *k-ω* model is due to the following modifications:

- The standard *k-ω* model and the transformed *k-ε* model are both multiplied by a blending function and this blending function is designed to be standard *k-ω* model in the near-wall region and the transformed *k-ε* model away from the surface. The standard *k-ω* model is zero away from the surface and the transformed *k-ε* model activated.
- The standard *k-ω* model changes gradually to a higher Reynolds number version of *k-ε* model from the inner boundary layer to outer part of boundary layer.
- The SST model incorporates a damped cross diffusion derivative term in the *ω*-equation.
- The definition of the turbulent viscosity is modified to account for the transport of the turbulent shear stress.
- modified turbulent viscosity formulation to account for the transport effects of the principal turbulent shear stress.

The *k-ω* SST model is named to account the turbulent viscosity modification to transport of the turbulent shear stress. The *k-ω* SST model is used directly deep down to wall boundaries viscus sublayer and for low Reynolds turbulence model without any extra damping function. The *k-ω* SST also switches to a *k-ε* behaviour in the free-stream and thereby avoids the common *k-ω* problem that the model is too sensitive to the inlet free-stream turbulence properties. Other modifications include the addition of a cross-diffusion term in the *ω* equation and a blending function to ensure that the model equations behave appropriately in both the near-wall and far-field zones (Karim et al., 2011).

Transport equations for the *k-ω* SST model are given in the following two equations:

$$\frac{\partial}{\partial t}(rk) + \frac{\partial}{\partial x_i}(rku_i) = \frac{\partial}{\partial x_i}\left(\Gamma_k \frac{\partial k}{\partial x_i}\right) + \tilde{G}_k - Y_k + S_k$$

$$\frac{\partial}{\partial t}(r\omega) + \frac{\partial}{\partial x_i}(r\omega u_i) = \frac{\partial}{\partial x_j}\left(\Gamma_\omega \frac{\partial \omega}{\partial x_j}\right) + G_\omega - Y_\omega + D_\omega + S_\omega$$

where, $\tilde{G}_k$ is the turbulence kinetic energy generated due to mean velocity gradients, G_ω is the generated specific dissipation rate (*ω)*, Γ_k and Γ_ω is for effective diffusivity of k and ω, respectively, Y_k and Y_ω is for dissipation of *k* and *ω* due to turbulence, D_ω is for the cross-diffusion term, S_k and S_ω are source terms.

3.5 ANSYS Fluent CFD Analysis

The program used to solve the flow condition of the fluid over the blade was ANSYS Fluent 2021/R2. For finite volume code in order of describing turbulence flow models, ANSYS Fluent is a candidate commercially available computer program (Fikade et al., 2020; Muiruri et al., 2019).

3.5.1 Computational Domain

The study is conducted in rectangular shape flow tunnel computational domain. Lift and drag force and coefficient of a blade can be computed in a rectangular flow domain (Fikade et al., 2020). To create the computational domain, after the baseline blade and the blade with winglets are created by using SOLIDWORKS software they are imported to ANSYS Design-modeler. The blades ware placed inside a tunnel like flow domain. The domain created 2R (twice radius of turbine) distance from upstream side, 4R to downstream side, 1R form both suction side and pressure side of the blade, and 3R width. The flow domain is shown in figure below:

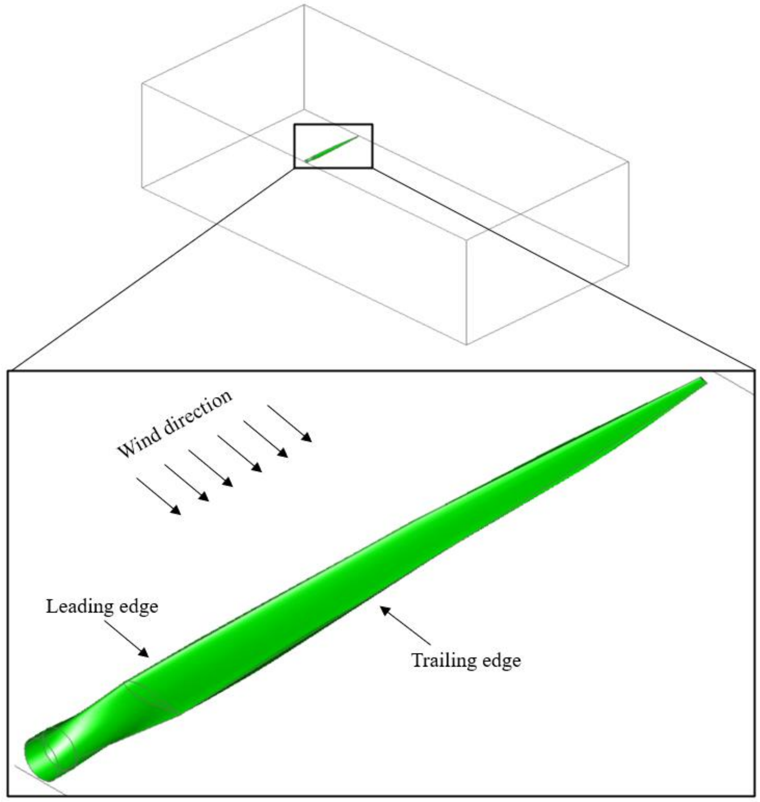

Figure 3.10 CFD computational domain

3.5.2 Meshing

The computational mesh was generated by discretizing the fluid domain in to a hybrid cells. This hybrid cells were composed of structured and unstructured mesh. The structured mesh was created around blade surface by using fifteen inflation layers with a transition rate of 0.272 and 1.1 growth rate. This inflation created structured mesh is used to assess the boundary layer on the blade surface.

The fluid domain was discretized using a sphere influence of 25 m radius a center point of mid length of the blade with a mesh size of 1.5 m. The remaining domain sized by 7 m mesh size. The blade surface was discretized by 0.08 m. Mesh generation was implemented using inside to outer strategy such that, first, blade faces were meshed followed by inflation layer around blade surface, then lastly, full flow domain. For each mesh generation, the quality of mesh elements was examined on the basis of 0.9 skewness.

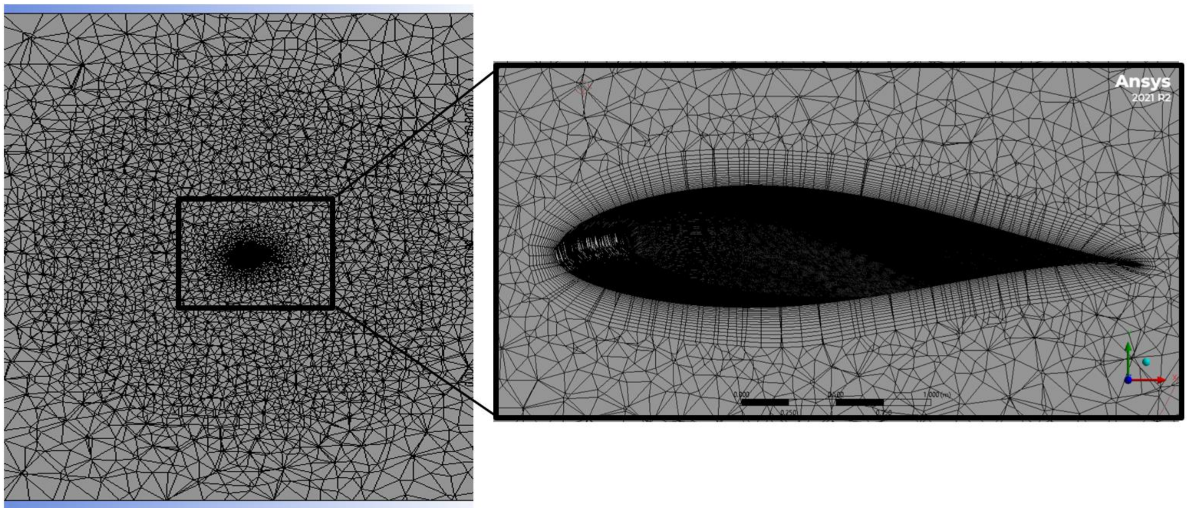

(a)

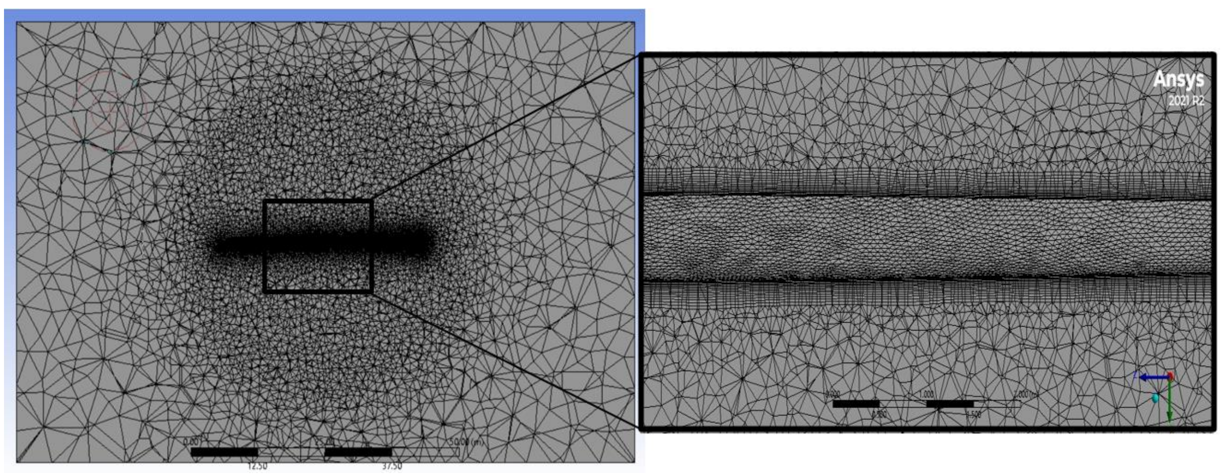

(b)

Figure 3.11 a) mesh across blade's chord and b) mesh across blade's span

3.5.3 Boundary Conditions

At the inlet of the flow domain a uniform inflow velocity was specified in all simulation. The flow was in the direction of positive x-axis (1, 0, 0). Based on the rated wind speed of Adama I wind turbine the inlet flow velocity was specified as 11 m/s for effect with AOA study.

The blade and winglet surface were specified as a stationary with no-slip boundary condition. At the outlet, the zero-gauge pressure was specified with turbulent intensity and turbulent viscosity ratio of 5% and 10% respectively in all simulations. Other four face were considered to be symmetry to take an advantage of considering the flow outside the domain.

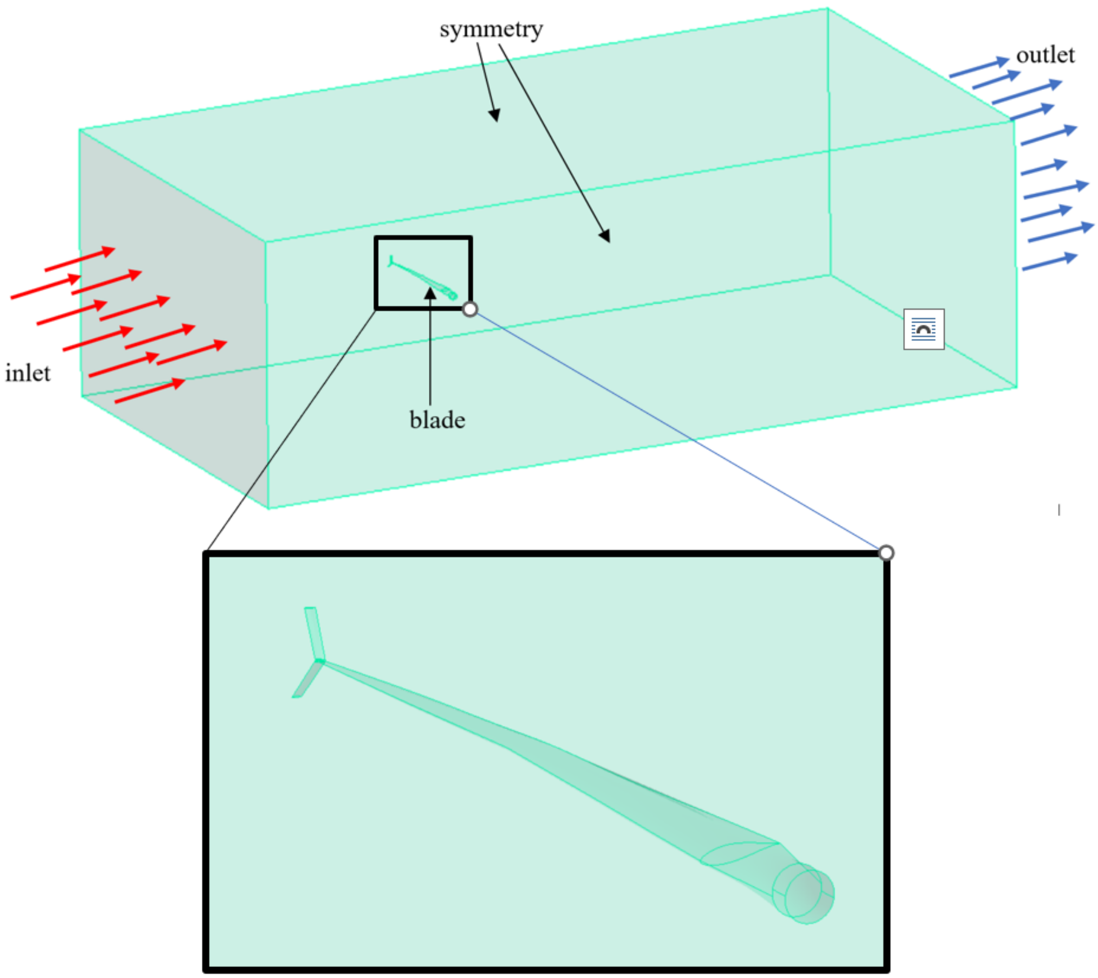

Figure 3.12 Boundary conditions

3.5.4 Grid Independence Test

The big concern during simulation of any system in ANSYS Fluent is the fineness of the mesh. If the mesh is not fine enough, it may cause a value difference. So, the surface mesh of the study model should be fine enough to eliminate any error. In order to evaluate the effect of the mesh size, it is rearranged from course to fine mesh until an approximated value found. Simulation on the baseline blade at 0° angle of attack was used to conduct the mesh independence test. The angle of attack was considered at maximum chord length. Since the solution near the blade surface was big concern then the mesh near the blade surface were tested from course to finer mesh size. The number of element cell of the mesh independence test is shown in Table 6 below.

Table 6. Number of cell element for mesh independence test

Mesh name	**Element size**	**Number of Element**	**C_l/C_d**
Mesh 1	0.25m	519,275	3.99801
Mesh 2	0.2m	617,862	4.1349
Mesh 3	0.15m	808,702	4.39087
Mesh 4	0.1m	1,315,878	4.59071
Mesh 5	0.08m	1,790,211	4.59558

As presented in Table 6 C_l/C_d value has only 0.005 difference between number of element size 1,315,878 and 1,790,2011, those elements have 0.1% error between them. So, mesh 5 element size was enough to compute the simulation work, since it was fair enough compared to the others. The result also presented in graph form in figure 3.13 below.

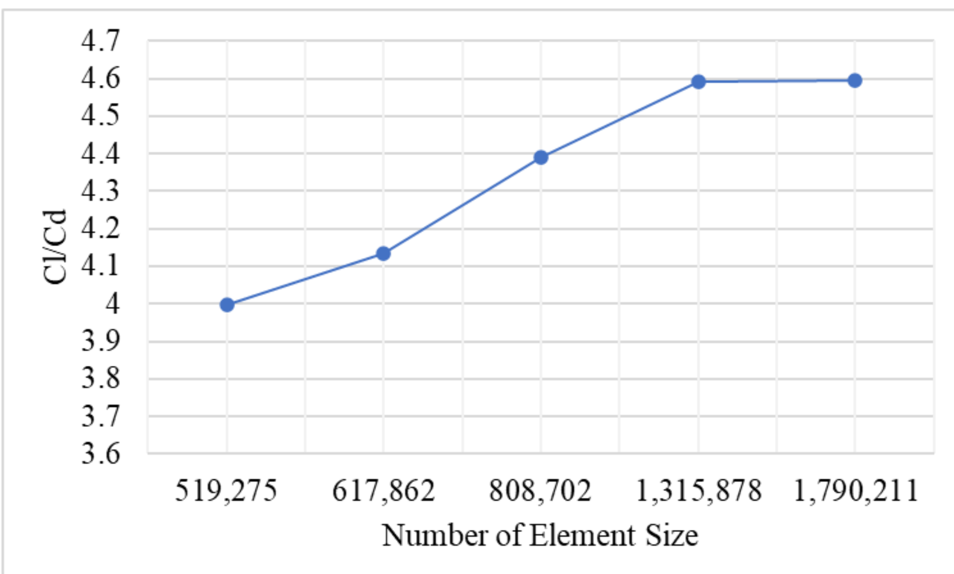

Figure 3.13 Grid independence test result

3.5.5 Solution Scheme

In this study ANSYS Fluent finite volume method was used in a three-dimensional setup with double precision and parallel scheme was applied in all simulations. A pressure-based type solver with an absolute velocity formation steady state flow condition was employed on the flow model. A *k-ω SST* turbulence model was applied which uses hybrid of both *k-ω* and *K-Ɛ*. *k-ω* performs near the blade surface and *K-Ɛ* for free streams.

In this thesis a Semi-Implicit Method for Pressure-Linked Equations (SIMPLE) method was used from its fast convergence and accuracy. A Semi-Implicit Method for Pressure-Linked Equations (SIMPLE) algorithm used to decouple velocity and pressure in a segregated manner (Muiruri et al., 2019). In this approach the continuity and momentum equations used implicitly, then the pressure variable was first computed using the pressure correction equation. Afterwards, velocity variables were obtained from the momentum equations explicitly. The pressure is computed using a second order method, momentum is in a second order upwind, and the turbulence kinetic energy and specific dissipation rate was computed by first order upwind method for its fast convergence.

CHAPTER FOUR

RESULTS AND DISCUSSIONS

4.1 Introduction

The result and discussion presented on the bases of ANSYS Fluent results of the baseline blade and blade with split winglets. This study was conducted on the fluid flow phenomena over the blades to show the aerodynamic effect of split winglets. The aerodynamic effect of adding split winglet on the blade will be compared with the baseline blade. This aerodynamic result will be supported by different graph and plots extorted from ANSYS Fluent.

4.2 Aerodynamic Characteristics of Baseline Blade

The aerodynamic characteristics of blade should be discussed to know how the fluid flow phenomena affect the aerodynamic efficiency of the blade specially the lift to drag coefficient of the blade. In this section of the study the flow characteristics of the baseline blade will be discussed based on the result extracted from ANSYS Fluent. The simulation conducted using designed wind velocity of Adama I wind turbine, which was 11 m/s.

4.2.1 Pressure Contour and Velocity Streamline

The fluid flow condition over the blades could be used to specify flow phenomena and the aerodynamic performance of the blade. The aerodynamic performance of a blade could be specified by the aerodynamic force which was affected by angle of attack and wind velocity. In this thesis aerodynamic force of the blades with and without split winglets was tested at -5^o, 0^o, 2.5^o, 5^o, 10^o and 15^o angle of attack. In this section the pressure contour and velocity streamline graph discussed as follows at 0.2R, 0.5R, 0.75R, and 0.95R length through the blade span and suction and pressure side of the blade.

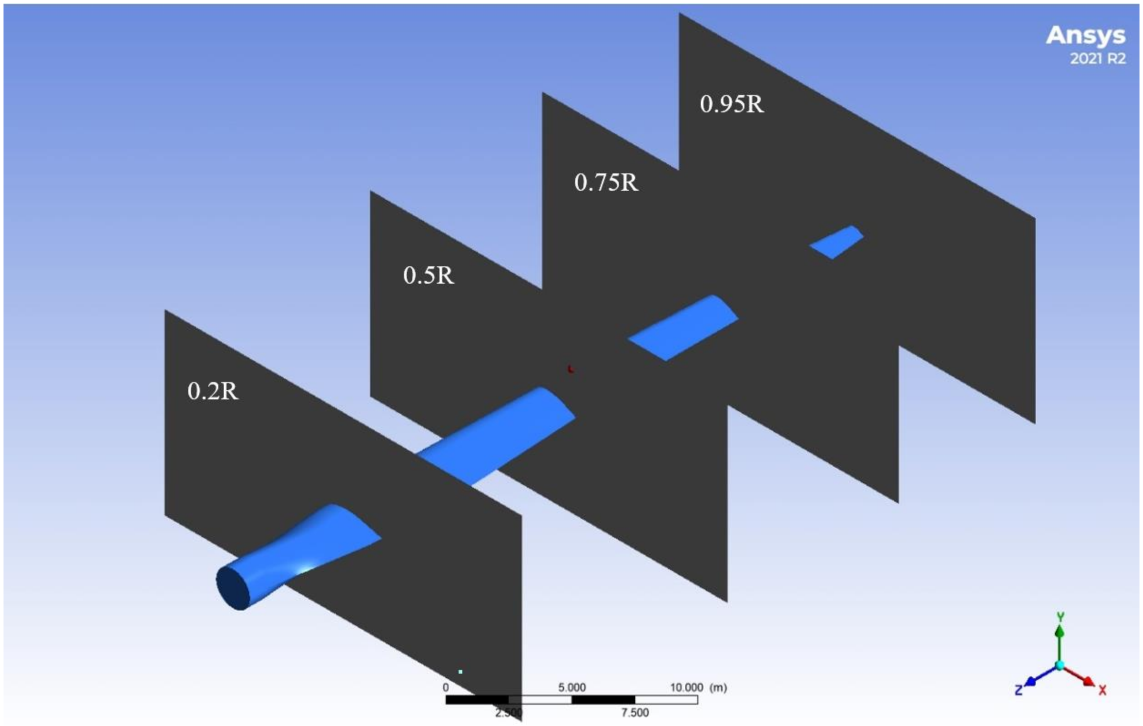

Figure 4.1 0.2R, 0.5R, 0.75R and 0.95R blade span wise location

Figure 4.1 shows the four span wise location planes which are used to express the pressure contour and velocity streamline of the fluid flow over the blade.

4.2.1.1 At -5° Angle of Attack

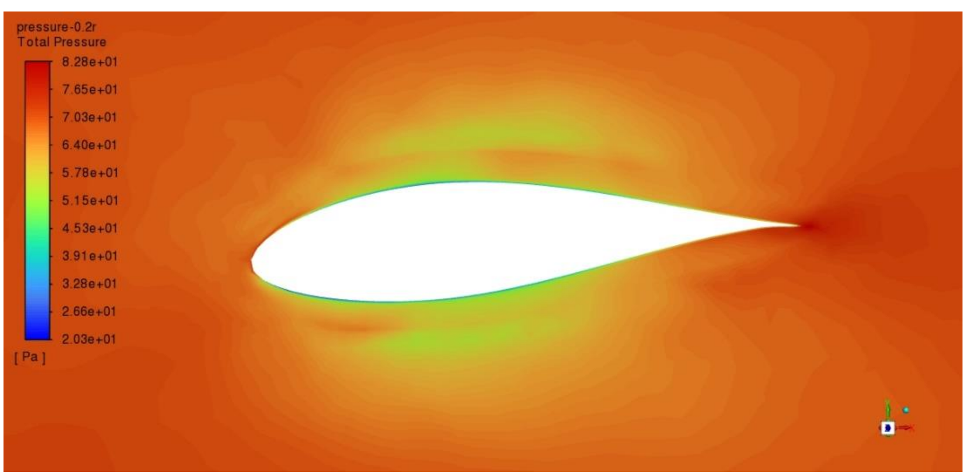

(a)

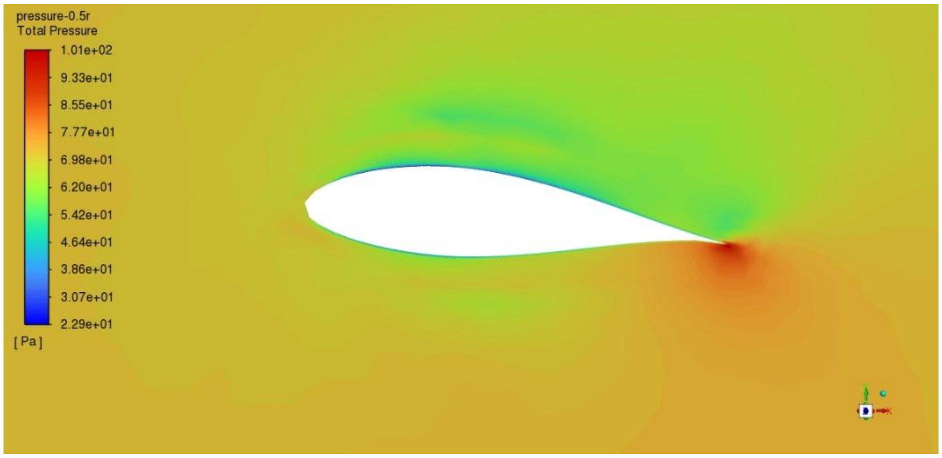

(b)

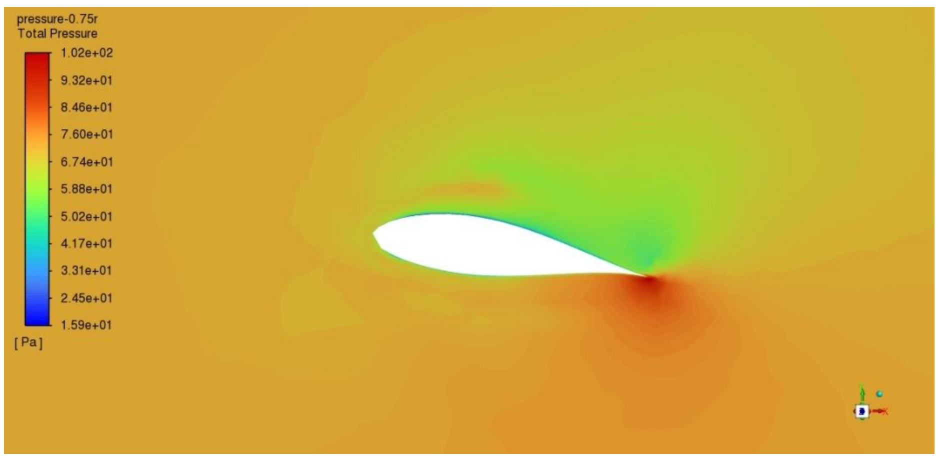

(c)

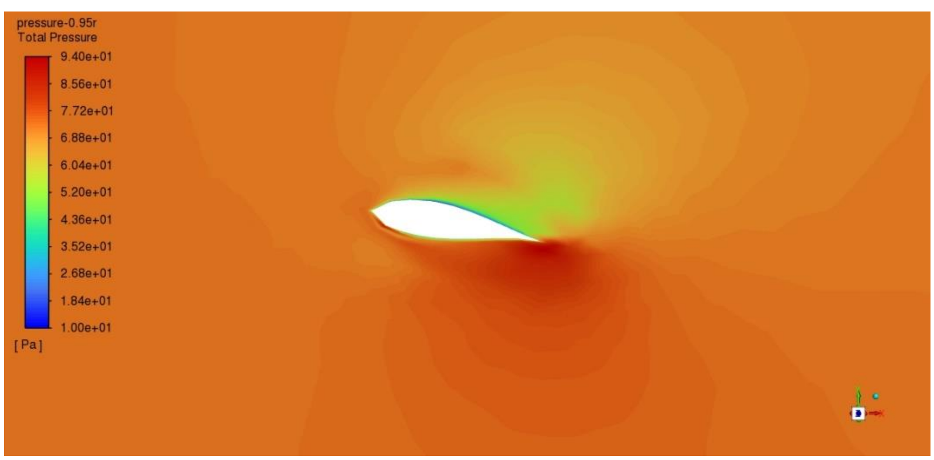

(d)

Figure 4.2 (a) 0.2R, (b) 0.5R, (c) 0.75R and (d) 0.95R Span wise length pressure contour view at -5º AOA

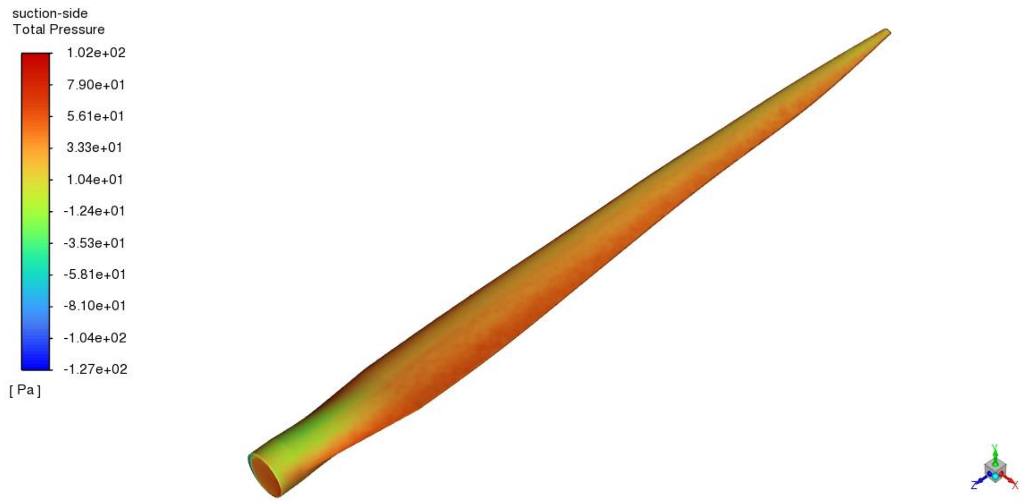

(a)

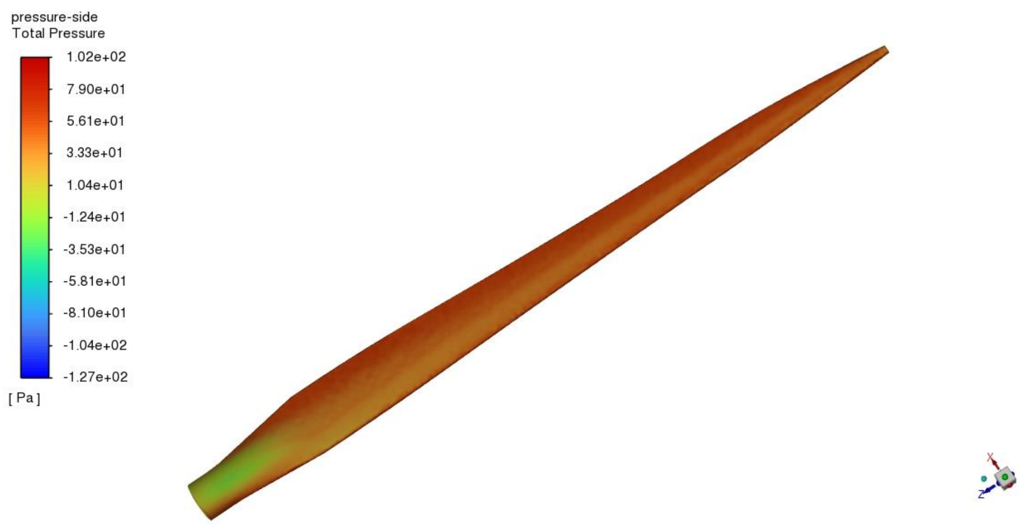

(b)

Figure 4.3 (a) suction side and (b) pressure side total pressure at -5° AOA

As shown in figure 4.2 (a) (at 0.2R span wise length) when the angle of attack is -5° the blade was experienced high-pressure force at leading edge near suction side of the blade. Even though it experienced high pressure at pressure side near the blade tip as shown in figure 4.2 (d) and figure 4.3 (b), its lift to drag coefficient was lower compared to other angle of attacks. This is due to most the blade area with experience high pressure was not pressure side of the blade.

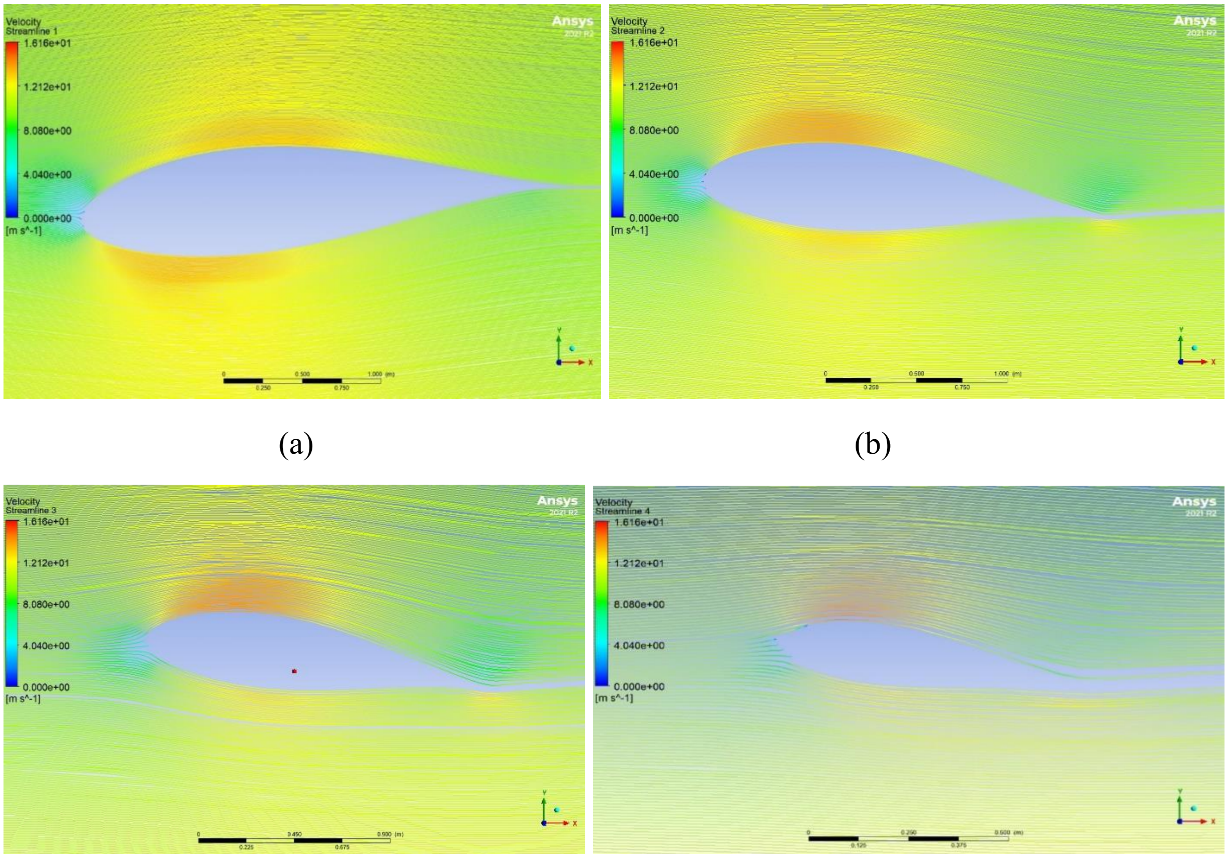

(a) (b)

(c) (d)

Figure 4.4 (a) 0.2R, (b) 0.5R, (c) 0.75R and (d) 0.95R Span wise length velocity streamline at -5° AOA

In figure 4.4 the velocity stream line plot shows at leading edge near the suction side was almost zero at 0.2R span wise distance and directly at leading edge for the other three span wise locations, so it was the reason to experience high-pressure around the leading edge. For an airfoil designed wind turbine blades in order to produce higher lift force the speed of wind at the pressure side of the airfoil have to be lower than suction side of the blade. even though the wind speed was higher at suction side than pressure side of the blade for 0.5R, 0.75R and 0.95R span wise location, since the wind speed is lower at suction side than pressure side for 0.2R span wise location then lift to drag coefficient ratio of the blade at -5° angle of attack was lower than at 0° angle of attack.

4.2.1.2 At 0º Angle of Attack

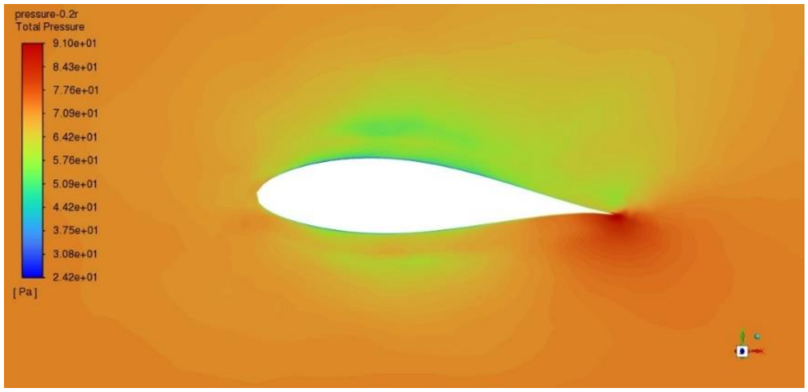

(a)

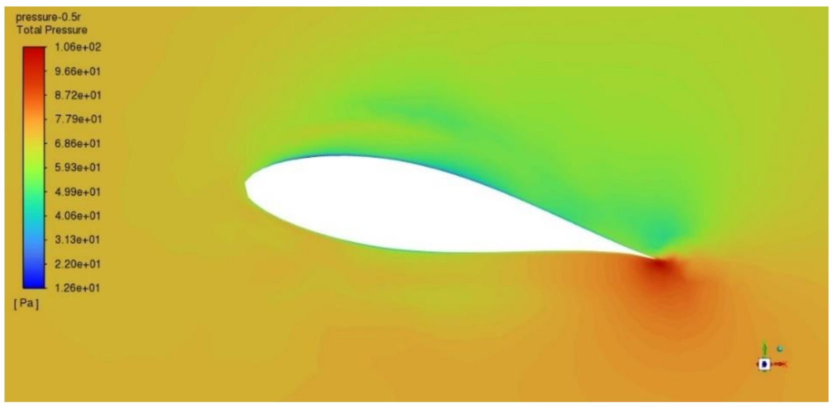

(b)

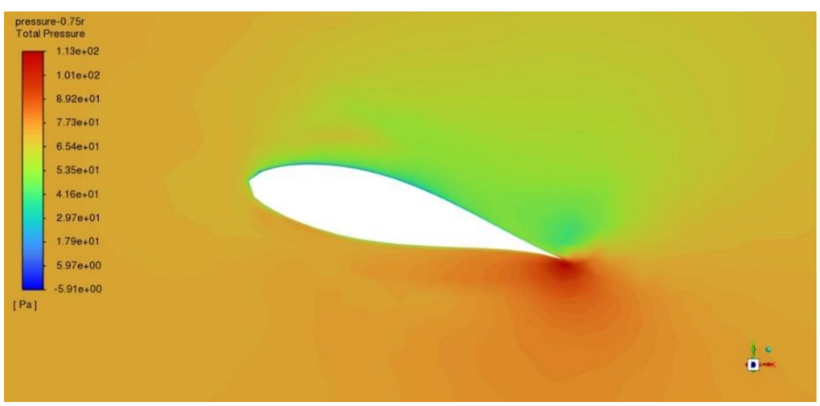

(c)

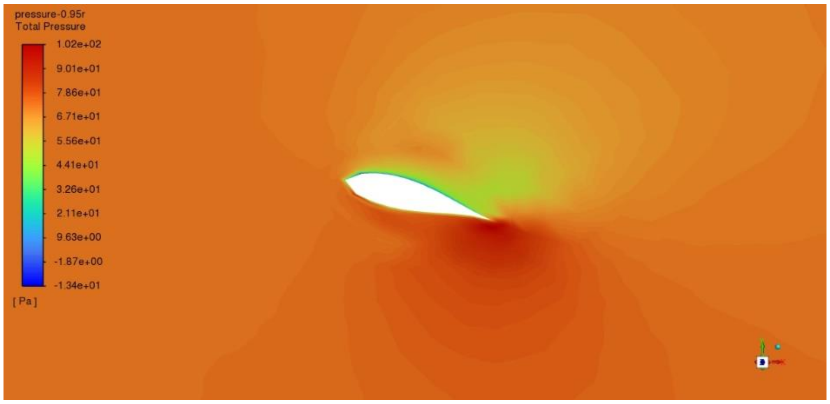

(d)

Figure 4.5 (a) 0.2R, (b) 0.5R, (c) 0.75R and (d) 0.95R Span wise length pressure contour view at 0^o AOA

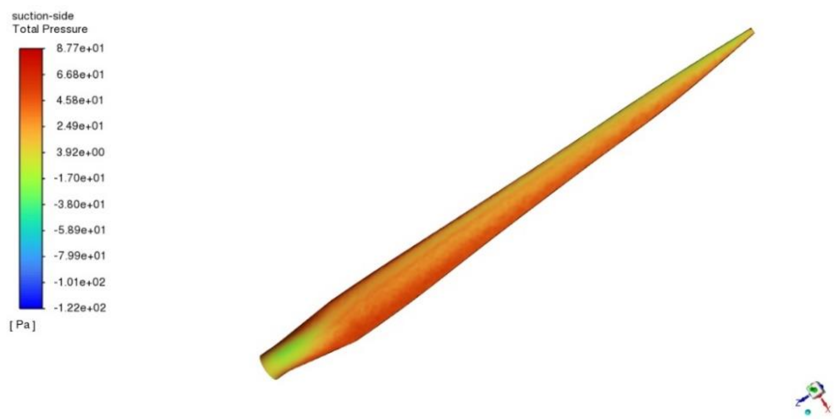

(a)

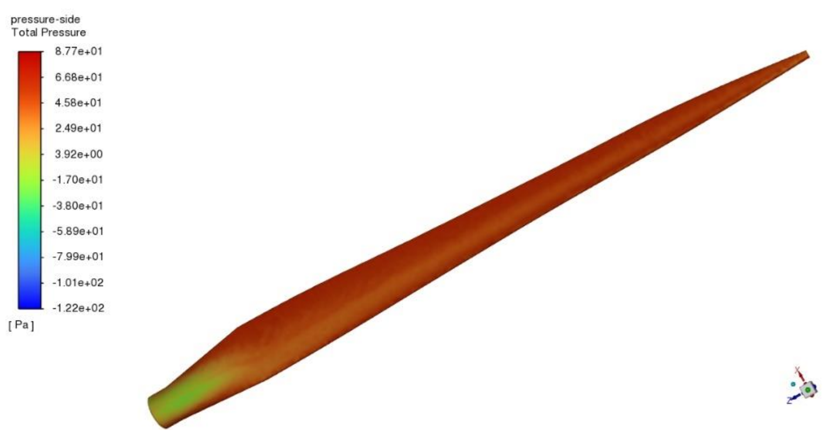

(b)

Figure 4.6 (a) suction side and (b) pressure side total pressure at 0^o AOA

As shown in figure 4.5 and 4.6 when the angle of attack is 0° the blade was experienced almost same pressure force at both suction and pressure side near root of the blade, but due to the blade twist angle at other spin wise length of the blade pressure at suction side was lower than pressure at pressure side of the blade. These makes the blade at 0° angle of attack to have higher lift to drag coefficient than -5° angle of attack.

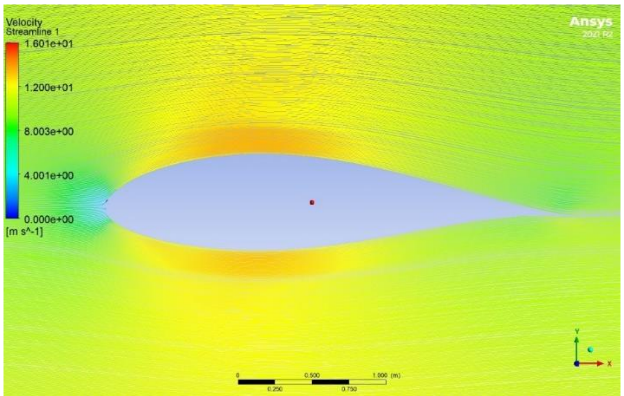

(a)

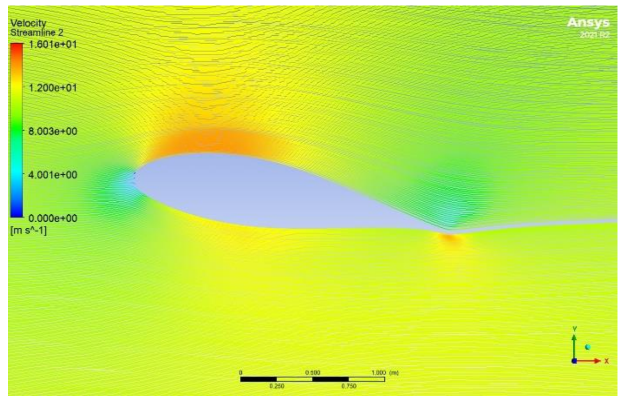

(b)

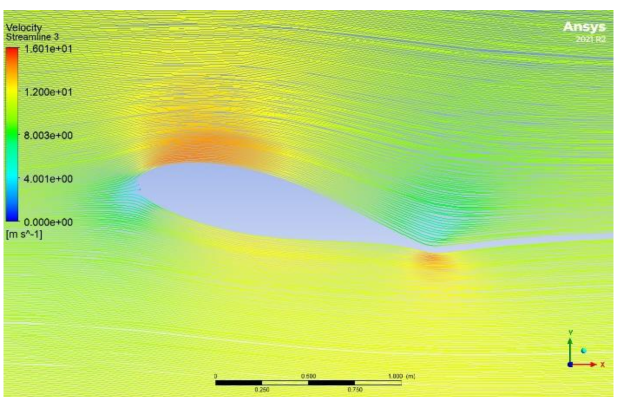

(c)

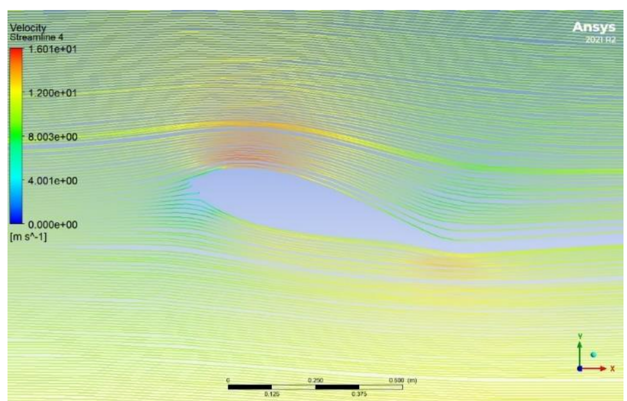

(d)

Figure 4.7 (a) 0.2R, (b) 0.5R, (c) 0.75R and (d) 0.95R Span wise length velocity streamline at 0° AOA

Figure 4.7 also shows the velocity is almost equal both suction and pressure side of the blade at 0.2R span wise length, but at other three span wise locations of blade flow was faster at suction side than pressure side. Due to this the pressure at suction side lower than pressure side at 0.5R, 0.75R and 0.95R span wise locations.

4.2.1.3 At 2.5º Angle of Attack

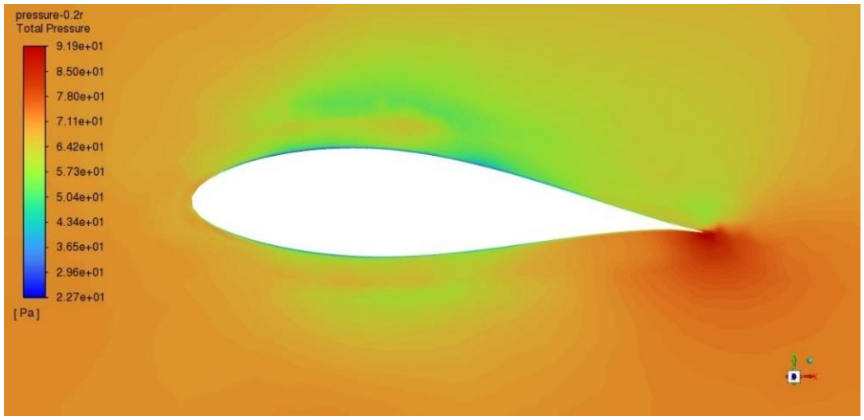

(a)

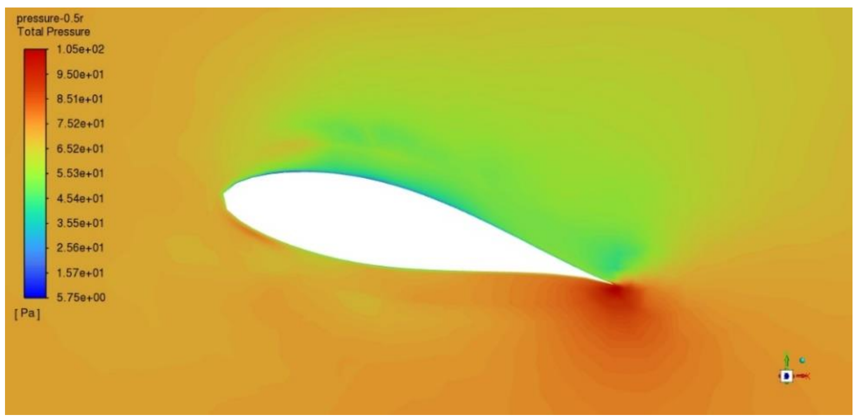

(b)

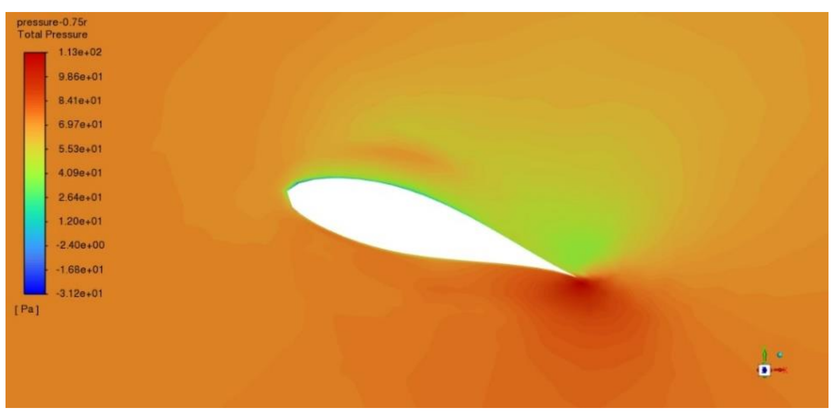

(c)

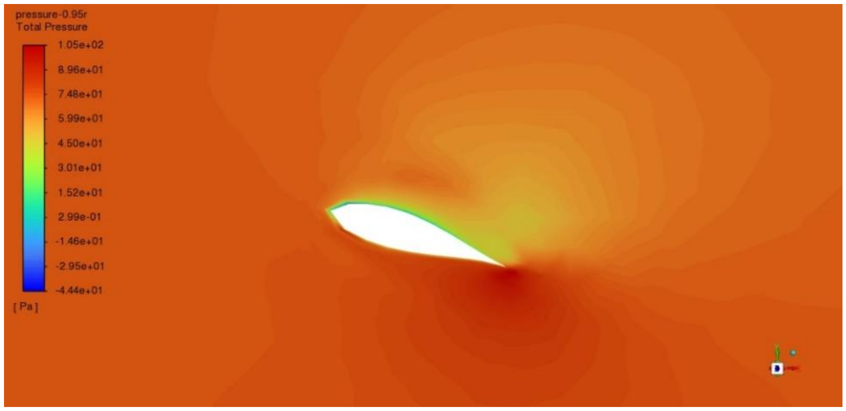

(d)

Figure 4.8 (a) 0.2R, (b) 0.5R, (c) 0.75R and (d) 0.95R Span wise length pressure contour view at 2.5º AOA

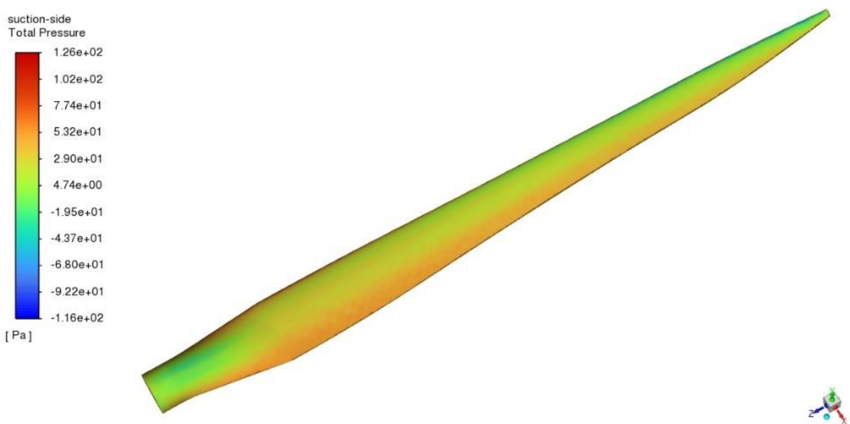

(a)

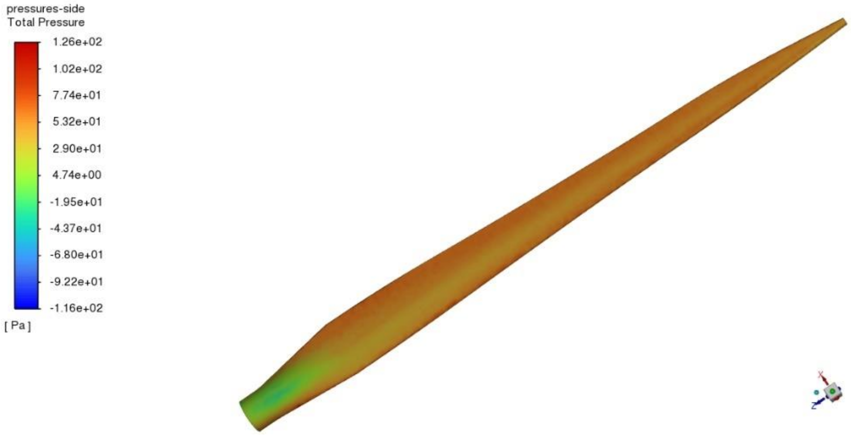

(b)

Figure 4.9 (a) suction side and (b) pressure side total pressure at 2.5º AOA

As shown in figure 4.8 and 4.9 when the angle of attack is 2.5° the blade was experienced almost same but a little bit higher pressure force at pressure side than suction side near root of the blade, but like 0° AOA the blade at 2.5° AOA has blade pressure force at suction side was lower than at pressure side of the blade. Even though at 2.5° AOA the blade had higher lift force than 0o AOA, its drag force also higher. So, the lift to drag coefficient of the blade was almost equal for both 0° and 2.5° AOA.

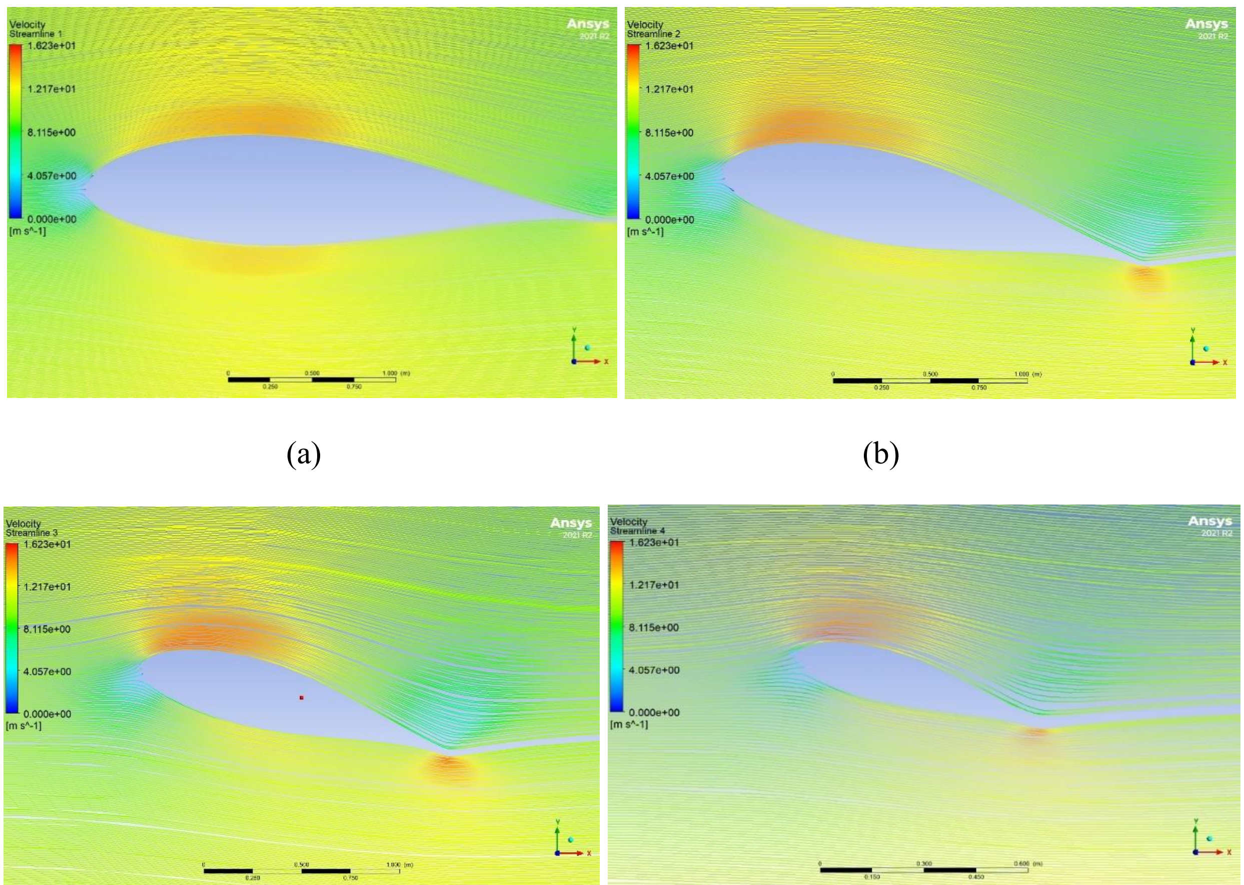

(a) (b)

(c) (d)

Figure 4.10 (a) 0.2R, (b) 0.5R, (c) 0.75R and (d) 0.95R Span wise length velocity streamline at 2.5° AOA

As shown in figure 4.10 the flow was faster at suction side of the blade than pressure side for all span wise location of the blade. From figure 4.10 (d) and figure 4.8 (d) could be conclude that the flow separation at 2.5° AOA creates little bit before 0° AOA, this was also evidence to the drag force higher at 2.5° AOA.

4.2.1.4 At 5° Angle of Attack

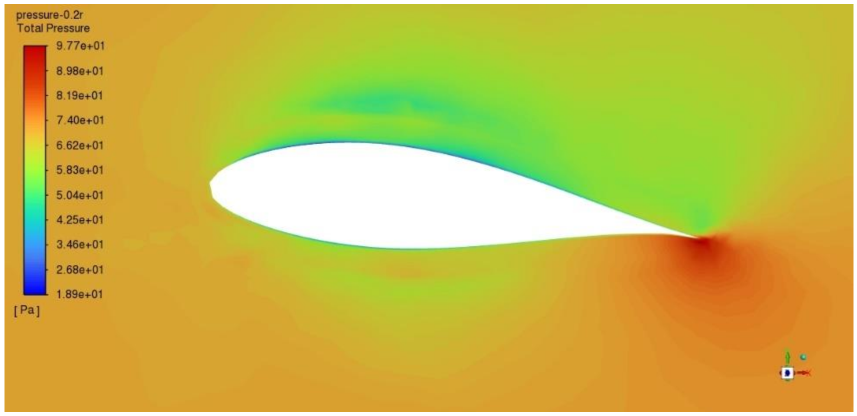

(a)

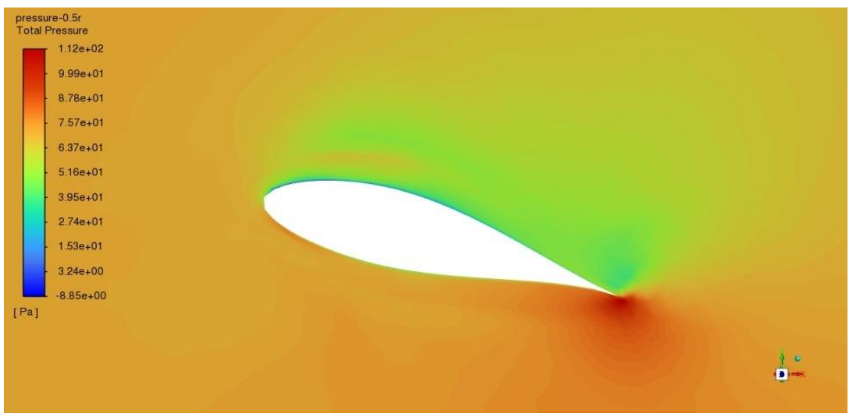

(b)

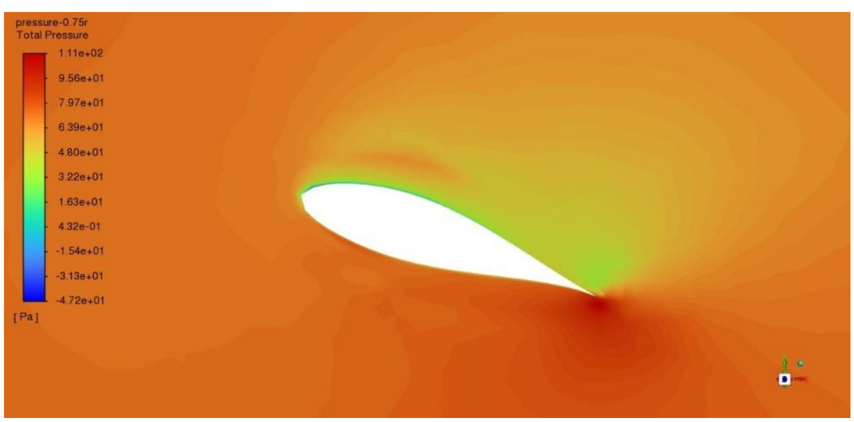

(c)

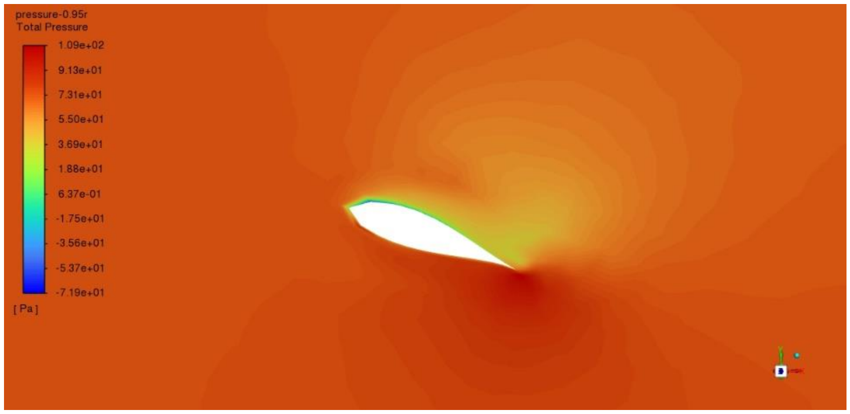

(d)

Figure 4.11 (a) 0.2R, (b) 0.5R, (c) 0.75R and (d) 0.95R Span wise length pressure contour view at 5° AOA

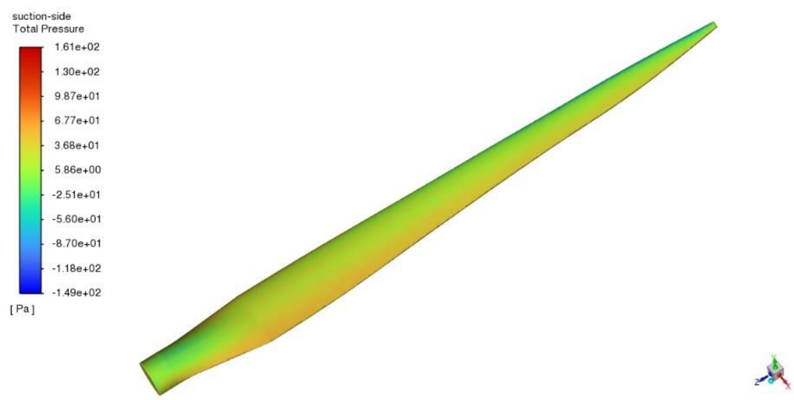

(a)

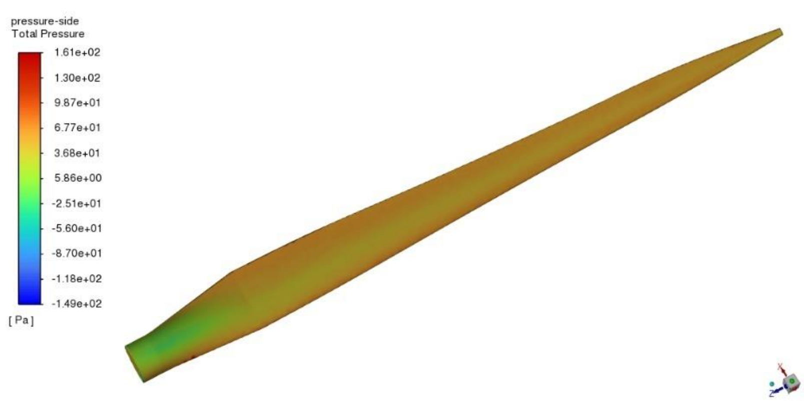

(b)

Figure 4.12 (a) suction side and (b) pressure side total pressure at 5° AOA

As shown in figure 4.11 and 4.12 the blade at 5º AOA experience more pressure force at pressure side than suction side of the blade. This makes at 5º AOA the blade to gave high lift force, also this angle of attack makes the blade to suffer high drag force than 0º and 2.5º AOAs. So, lift to drag coefficient of 5º AOA was lower than 0º and 2.5º AOAs.

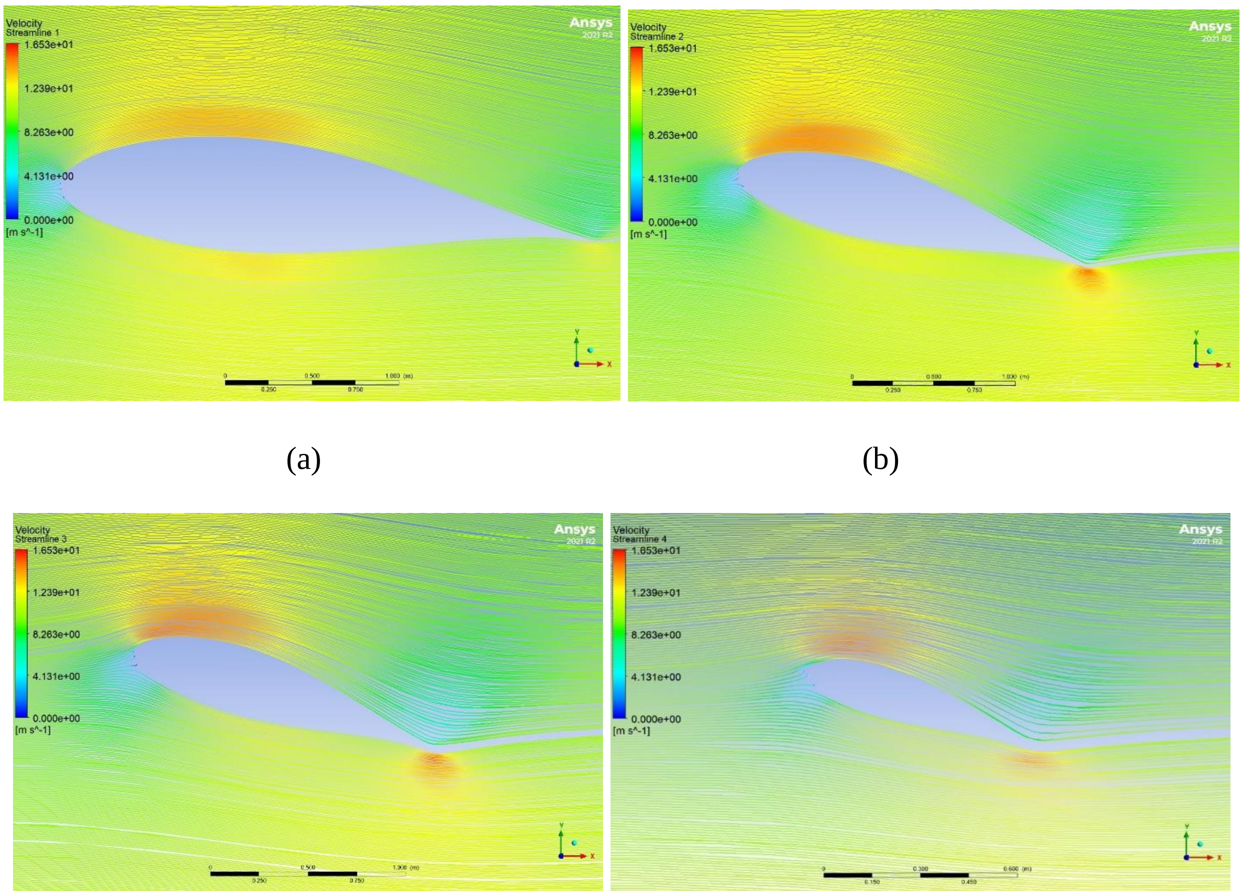

(a) (b) (c) (d)

Figure 4.13 (a) 0.2R, (b) 0.5R, (c) 0.75R and (d) 0.95R Span wise length velocity streamline at 5º AOA

In Figure 4.13 the velocity stream line plot shows that the flow was faster on suction side than pressure side at all span wise locations and also the flow at pressure side near the trailing edge becomes more faster at 0.5R, 0.75R and 0.95R than the previous AOAs. Due to this pressure at the trailing edge was more for this AOA and it was also the reason, it had lower lift to drag coefficient value than 0º and 2.5º angle of attacks.

4.2.1.5 At 10º Angle of Attack

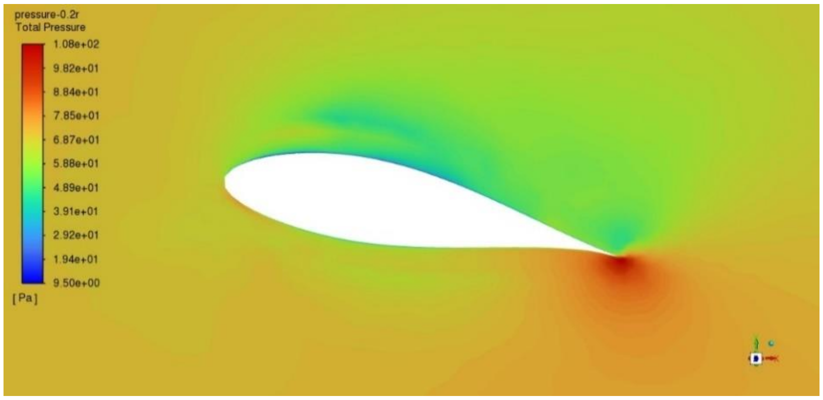

(a)

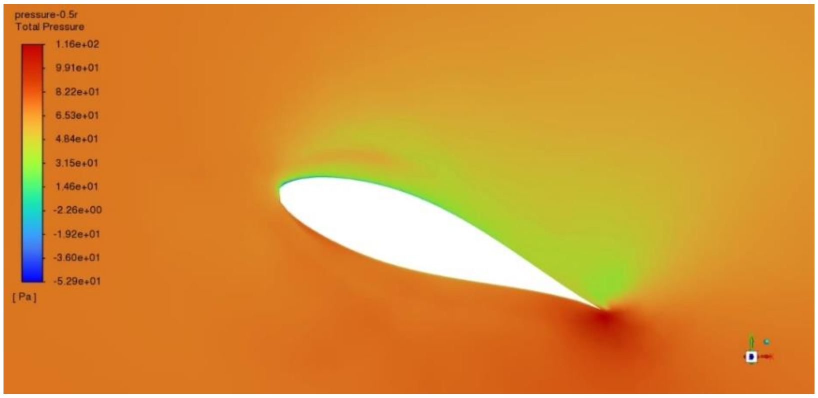

(b)

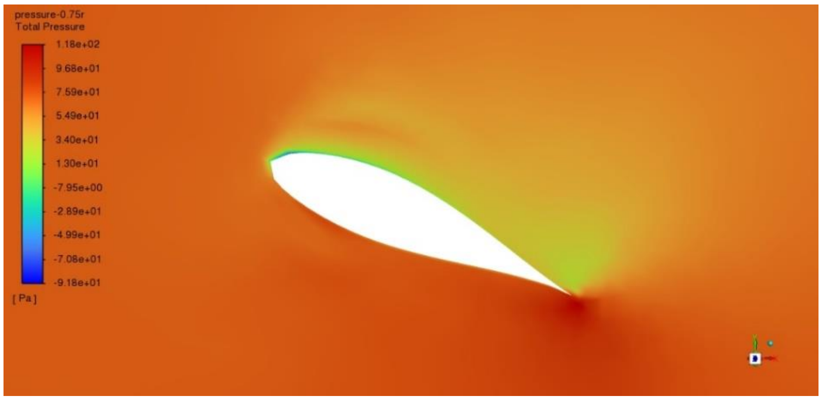

(c)

(d)

Figure 4.14 (a) 0.2R, (b) 0.5R, (c) 0.75R and (d) 0.95R Span wise length pressure contour view at 10º AOA

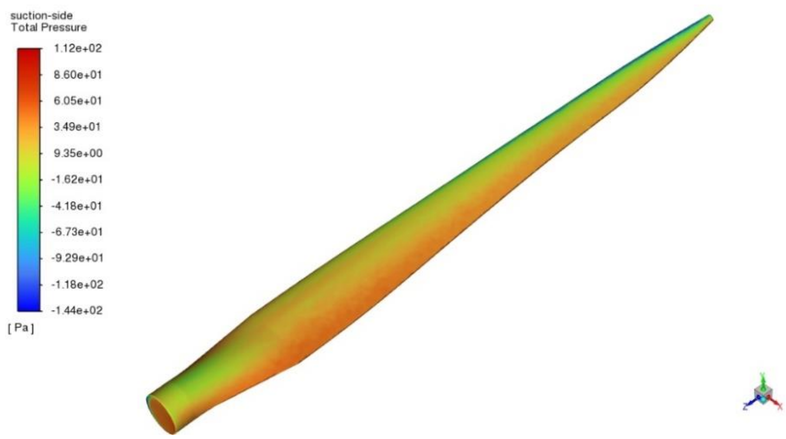

(a)

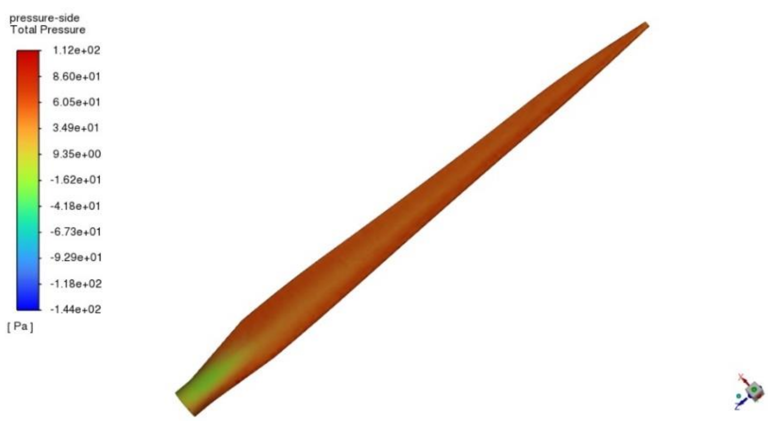

(b)

Figure 4.15 (a) suction side and (b) pressure side total pressure at 10º AOA

Figure 4.14 and 4.15 shows that blade at 10º AOA experience more pressure force at pressure side than suction side of the blade as compared with other AOAs. This makes at 10º AOA the blade to have high lift and drag force, even though lift to drag coefficient value at 10º AOA was much less than 0º, 2.5º and 5º AOAs. This was due to at 10º AOA the drag force was high relative to the produced lift force as it compared with the drag and lift force at 0º, 2.5º and 5º angle of attacks.

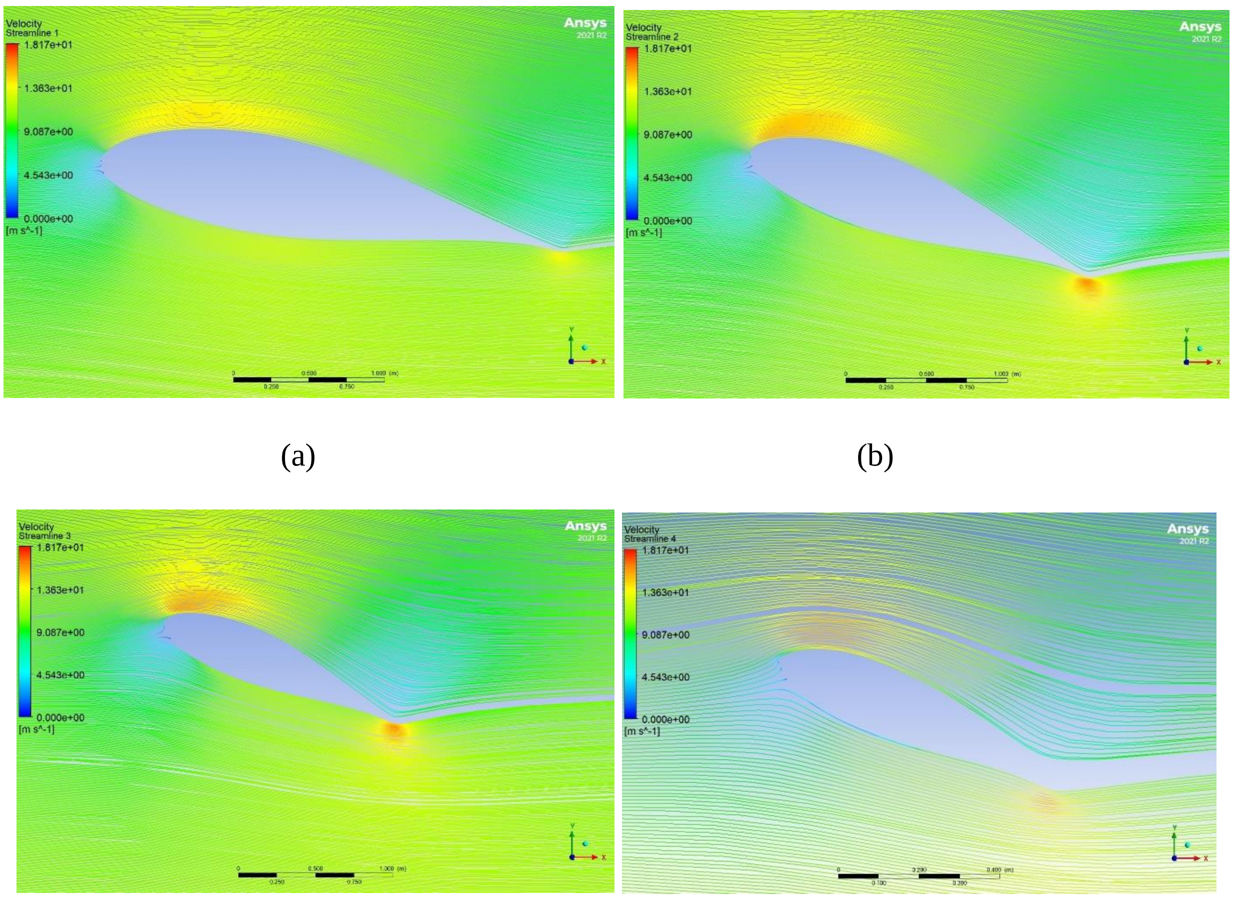

(a) (b)

(c) (d)

Figure 4.16 (a) 0.2R, (b) 0.5R, (c) 0.75R and (d) 0.95R Span wise length velocity Streamline at 10º AOA

In Figure 4.16 the velocity stream line plot shows that the flow was faster on suction side than pressure side at all span wise locations and also the flow at pressure side near the trailing edge becomes more faster at all span wise locations than the previous AOAs. Due to this pressure at the trailing edge was more for this AOA and it was also the reason that it had lower lift to drag coefficient value than 0º, 2.5º and 5º angle of attacks.

4.2.1.6 At 15° Angle of Attack

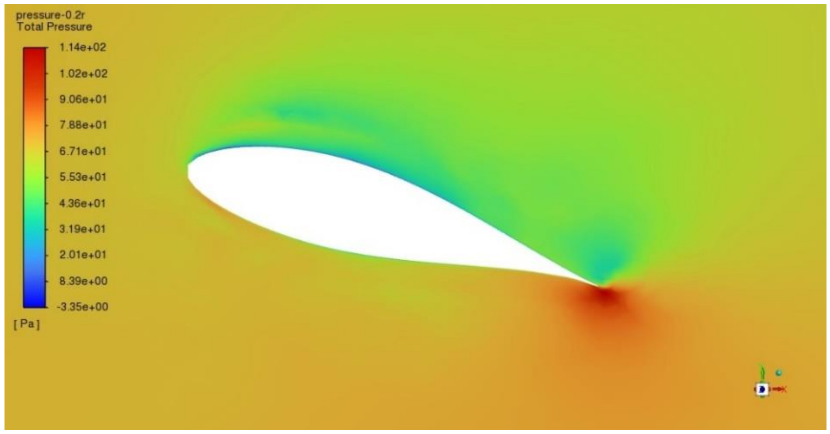

(a)

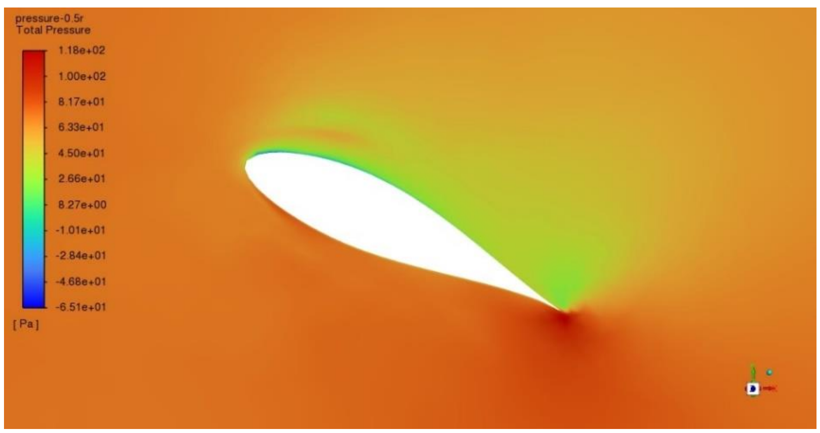

(b)

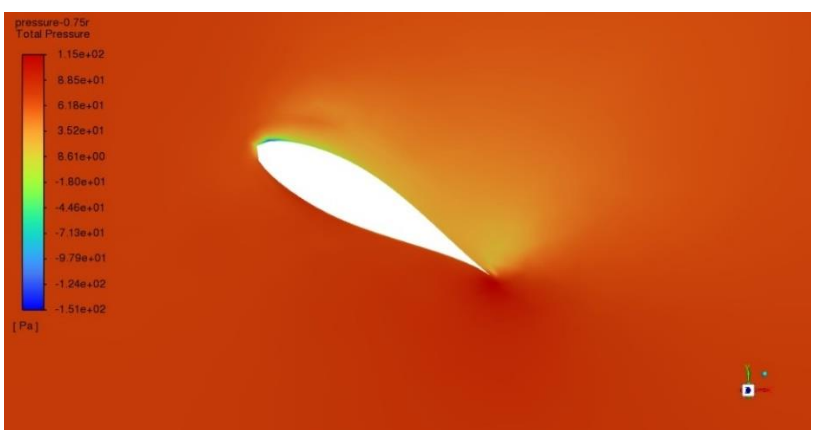

(c)

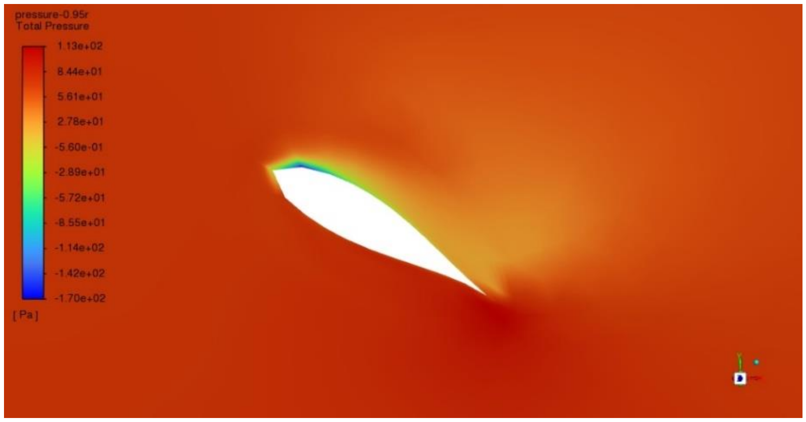

(d)

Figure 4.17 (a) 0.2R, (b) 0.5R, (c) 0.75R and (d) 0.95R Span wise length pressure contour view at 15º AOA

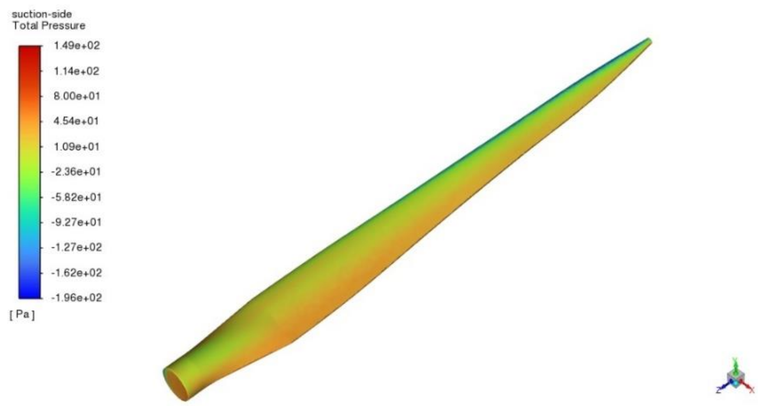

(a)

(b)

Figure 4.18 (a) suction side and (b) pressure side total pressure at 15º AOA

Figure 4.17 and 4.18 shows that blade at 10° AOA experience more pressure force at pressure side than suction side of the blade as compared with other AOAs. This makes at 15° AOA the blade to have high lift and drag force, even though lift to drag coefficient value at 15° AOA was much less than other angle of attacks. This was due to that, at 15° AOA the drag force was high relative to the produced lift force as it compared with the drag and lift force of other angle of attacks.

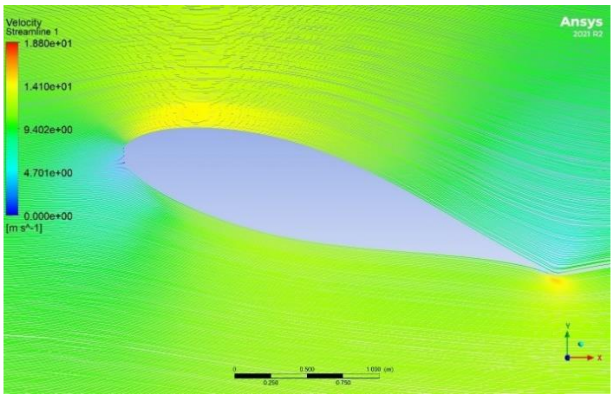

(a)

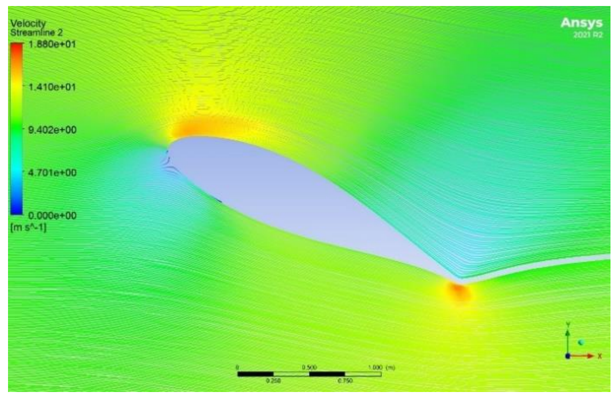

(b)

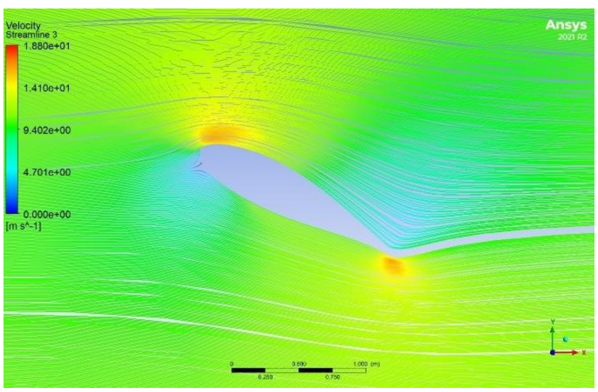

(c)

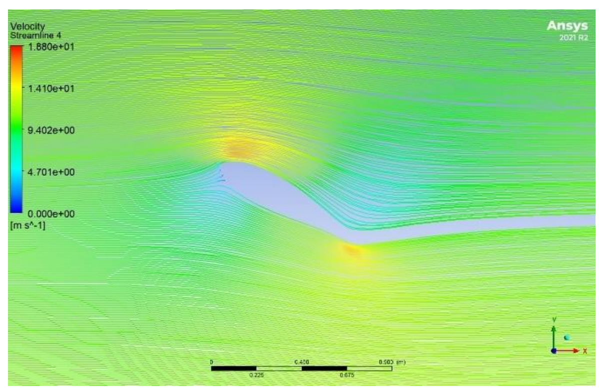

(d)

Figure 4.19 (a) 0.2R, (b) 0.5R, (c) 0.75R and (d) 0.95R Span wise length velocity streamline at 15° AOA

In Figure 4.19 the velocity stream line plot shows that the flow becomes more faster on suction side than pressure side at all span wise locations and also the flow at pressure side near the trailing edge becomes more faster and faster at all span wise locations than the previous AOAs, then the pressure at the trailing edge was more for this AOA. Due to curved nature of blade airfoil profile at trailing edge and this pressure the lift to drag coefficient value was lower than other AOAs.

4.2.2 Lift and Drag Coefficient of Baseline Blade

Aerodynamic performance evaluation of wind turbine blades, aircrafts, vehicles or any other device could be expressed by lift to drag force ratio (lift to drag coefficient ratio) of the device (Fikade et al., 2020). The baseline blade was tested in -5°, 0°, 2.5°, 5°, 10° and 15° angle of attacks in ANSYS fluent and lift and drag coefficient values were evaluated. The results data were extracted and plotted in graph as shown in figure 4.20 with respect to angle of attacks. All the CFD simulation plot of lift and drag coefficient is presented in Appendix (A-3).

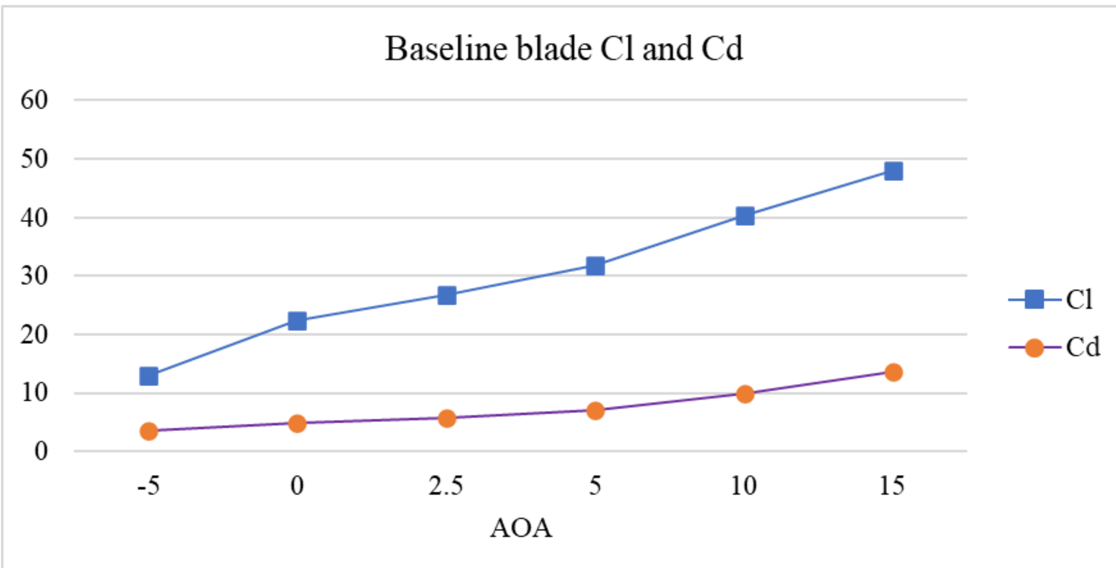

Figure 4.20 Baseline blade lift and drag coefficient verses angle of attack.

As discussed from section 4.2.1.1 to section 4.2.1.5 the baseline blade experienced low lift and drag force at lower angle and it was increased with angle of attack. This also could be visualised at figure 4.20. Though the lift force increased with angle of attack, the drag force also increased and a maximum lift to drag coefficient ratio was recorded at 2.5° angle of attack as shown in figure 4.21. so, the lift to drag coefficient ratio of the baseline blade was increased as angle of attack increases then reach at maximum value at 2.5° angle of attack after this it starts decreasing as angle of attack increases. The reason behind this was twisting behaviour of the blade, which leads the blade to experience more drag at higher angle of attacks.

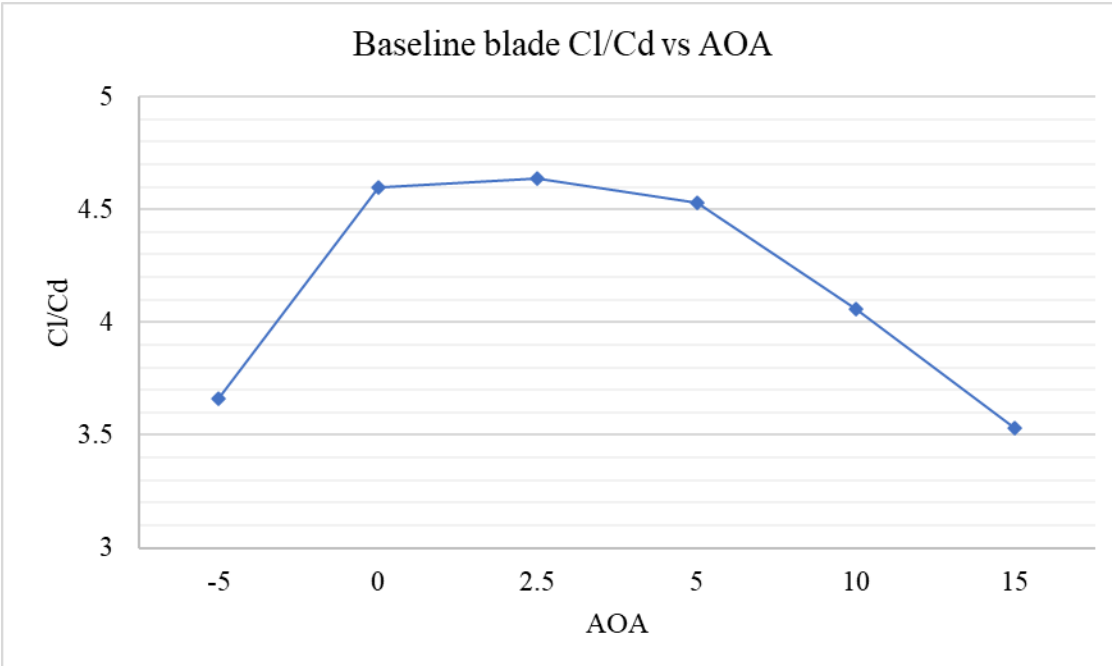

Figure 4.21 Baseline blade lift to drag coefficient verses angle of attack

4.3 Aerodynamic Performance of Blade with Split Winglet

Aerodynamic performance of the blade with split winglets was tested in a same flow condition as baseline blade at -5°, 0°, 2.5°, 5°, 10° and 15° of angle of attack. Six different blades with split winglet were tested. The first three winglets were designed with the same airfoil profile of the baseline blade with 30°, 40° and 50° cant angles, 4%R height, 0° sweep angle and 10° twist angle. The rest three winglets were designed with S813 airfoil profile with the same height, cant, sweep and twist angle of the first three blades.

The aerodynamic performance of the baseline blade and blade with winglets compared based on the amount of lift to drag coefficient ratio. The lift and drag coefficient values of blade with split wiglets were extracted from ANSYS Fluent results like the baseline blade and the plots are presented in Appendix (A-3).

As shown in figure 4.22 all blades with split winglets shows aerodynamic improvement at -5°, 0°, and 2.5° angle of attacks. The figure also demonstrates that at 5°, 10° and 15° angle of attacks blade with split winglet performance was lower than the baseline blade except the blade with winglet 6. Blade with winglet 6 in addition to its best performance over all tested angle of attacks, it was the best performed winglet design than other winglets over a range of high drag to lift coefficient recorded angle of attacks.

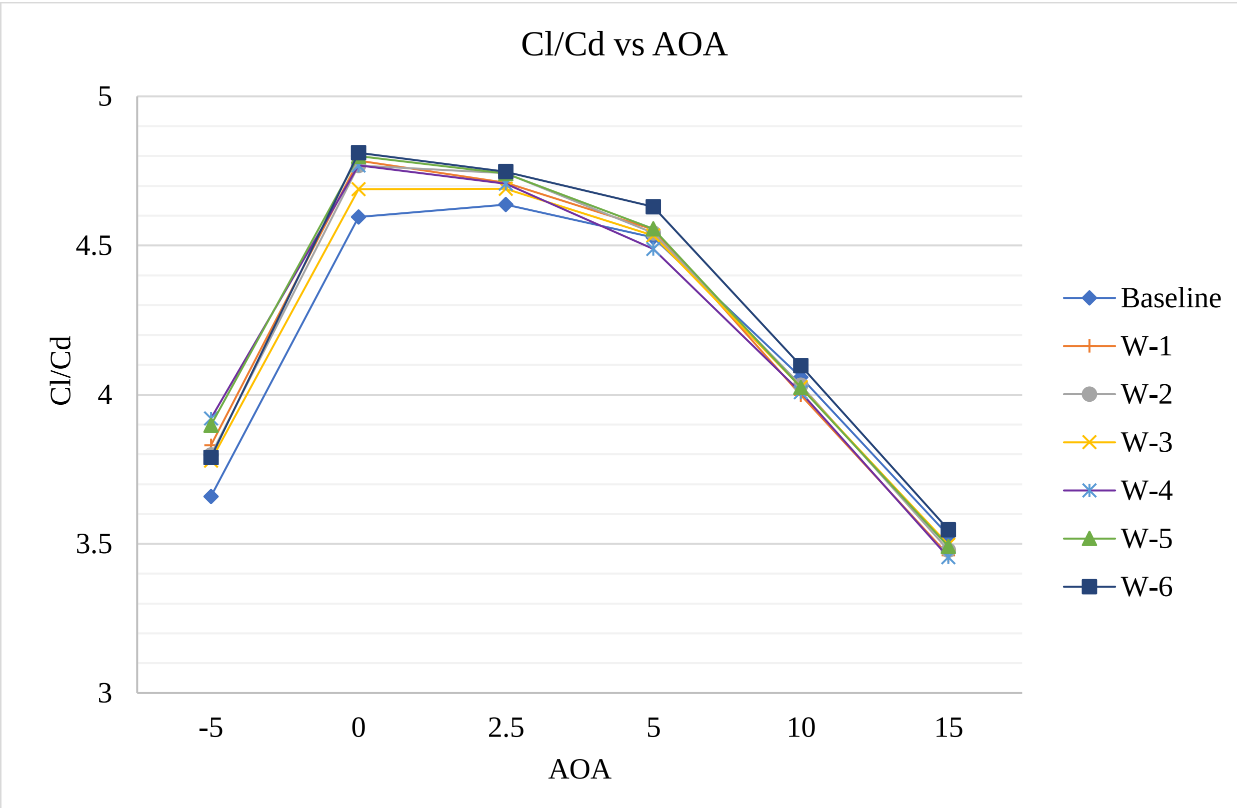

Figure 4.22 C_l/C_d comparison of baseline blade and blade with split winglets

The percentage variation of lift to drag coefficient ratio between baseline blade and blade with split winglets presented in Table 7 below. The aerodynamic performance improvement of up to 7.149% and decrement of -1.495% was recorded.

As shown in figure 4.22 above and also Table 7 demonstrates blades with winglets except blade with winglet 6 has a performance decrement at 10° and 15° angle of attacks compared to baseline blade. Blade with winglet 5 also shows a performance decrement at 5° angle of attack.

Table 7 also demonstrate that all blade with winglets (from winglet 1 to 5) have an improvement of aerodynamic performance from -5° to 5° angle of attacks except blade with winglet 5. For blade with winglet 6 the table shows it had an increment in all angle of attacks. Also, blade with winglet 6 shows maximum aerodynamic performance with an improvement of 4.686% at 0° angle of attack compared to the baseline blade.

Table 7. Percentage variation of lift to drag coefficient ratio between blade with and without split winglets.

Blade with split winglets	Percentage variation of lift to drag coefficient ratio (%)					
	Angle of Attacks					
	-5°	**0°**	**2.5°**	**5°**	**10°**	**15°**
W-1	4.686	4.112	1.574	0.590	-1.495	-1.886
W-2	3.800	3.753	2.273	0.350	-0.668	-1.409
W-3	3.281	2.039	1.142	0.147	-0.829	-0.888
W-4	7.149	3.767	1.514	-0.834	-1.262	-2.085
W-5	6.515	4.442	2.247	0.654	-0.865	-1.055
W-6	3.563	4.686	2.374	2.279	0.947	0.548

As shown in figure 4.23 colour map of pressure the blade with winglet 6 was experienced more pressure than baseline blade at pressure side of the blade. As visualised from the figures the blade with winglet 6 had 102 Pa pressure applied at pressure side of the blade, but for the base line blade it was only 87.7 Pa. The reason behind the aerodynamic performance improvement was this pressure difference which was created due to addition of winglet.

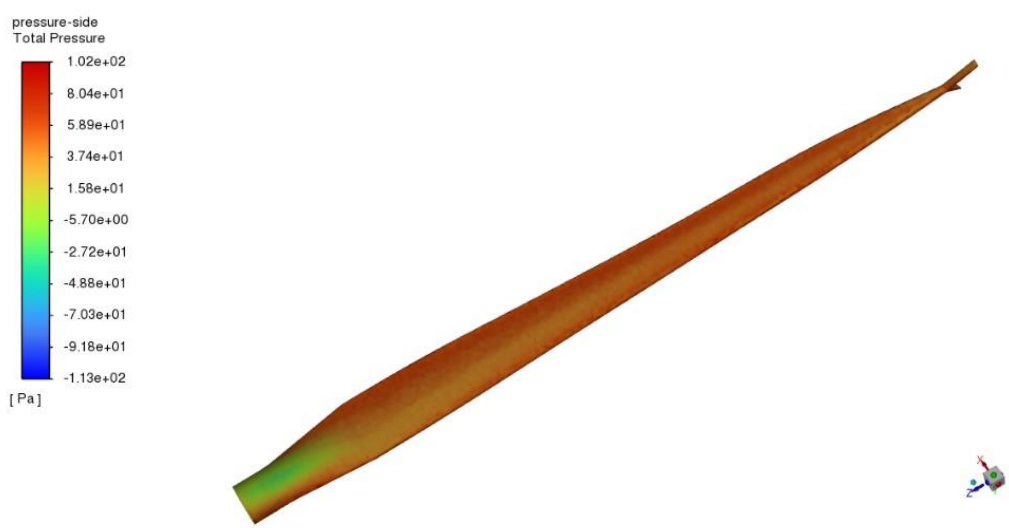

(a)

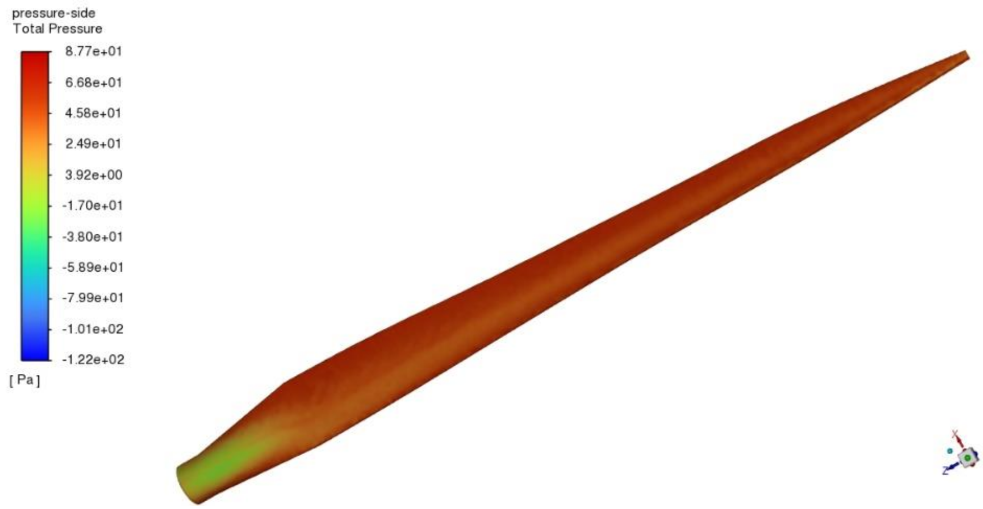

(b)

Figure 4.23 (a) blade with winglet 6 and (b) baseline blade pressure side total pressure at 0º AOA

Figure 4.24 also clearly demonstrated that addition of split winglet had an effect at tip of the blade. Pressure at suction side near tip of the blade was less, when split winglet was added on the blade. Also, pressure at pressure side near tip of the blade was higher, when split winglet was added on the blade. in addition to minimizing suction side pressure and maximizing pressure side pressure, the winglet gave an additional area to generate more lift.

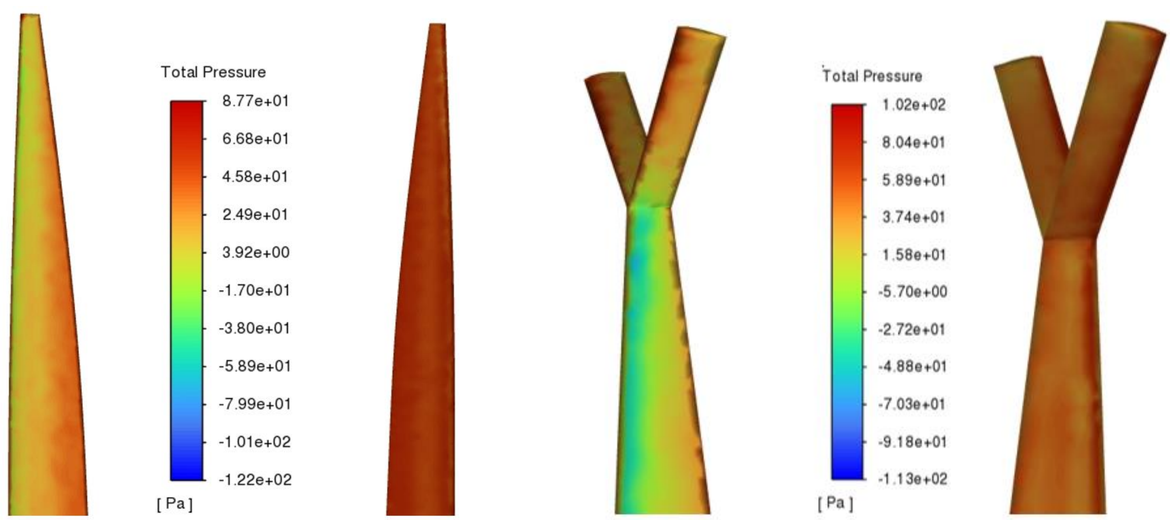

(a) (b)

Figure 4.24 (a) baseline blade and (b) blade with winglet 6 around blade tip suction and pressure side total pressure.

It was an additional conformation that in figure 4.25 the wind velocity of blade with W-6 was greater than baseline blade at suction side of the winglet. Since velocity and pressure are inversely proportional to each other, which mean that the pressure of blade with W-6 was higher than baseline blade at suction side of the blade.

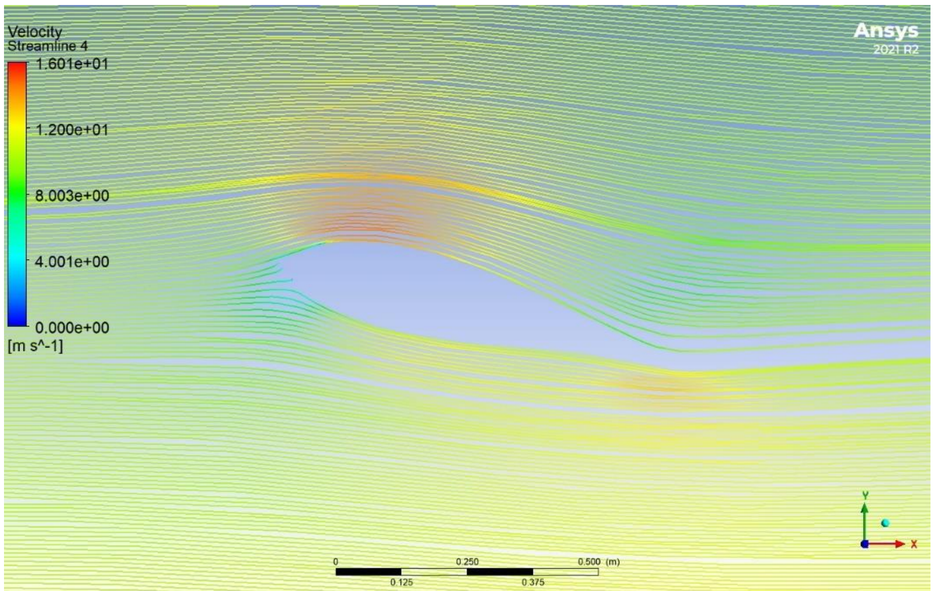

(a)

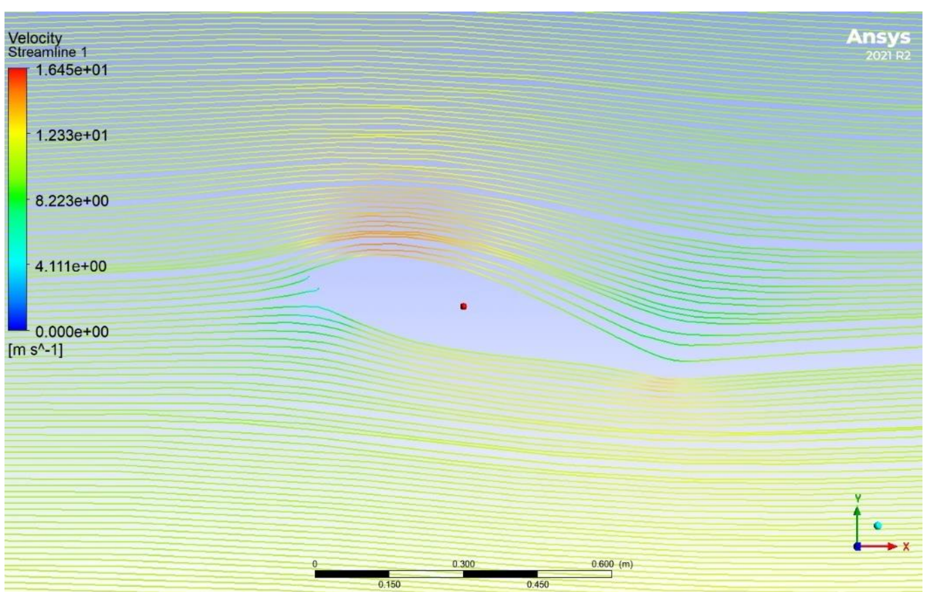

(b)

Figure 4.25 (a) baseline blade and (b) blade with winglet 6 velocity streamline at 0.95R span

4.3.1 Comparison of Winglet Parameter

As shown in the previous section blade with winglet 6 performs better than other winglets compared to baseline blade. For purpose of check this winglet parameter is better, its cant angle and twist angle of the winglet 6 was changed and tested. For purpose of comparison the flow condition was based on the same flow condition of this thesis. Since the lift to drag coefficient value continues decreasing above 10° then the study with split winglet is performed from -5° to 10° AOA in 5° intervals.

4.3.1.1 Cant Angle Comparison

Winglets W-4, W-5 and W-6 were design at 30°, 40° and 50° cant angle respectively. As demonstrated in Table 7 and figure 4.22 W-6 performed better than W-4 and W-5. An additional winglet called winglet 7 (W-7) is design at cant angle of 60° and tested with same flow condition. Other parameters were keeping constant.

As shown in figure 4.26 below winglet 7 performance was lower than winglet 6, this was due to that as the cant angle increases more than the optimum cant angle it causes an additional drag on the blade and decrement of aerodynamic performance. So, 50° cant angle was the optimum cant angle for split winglets.

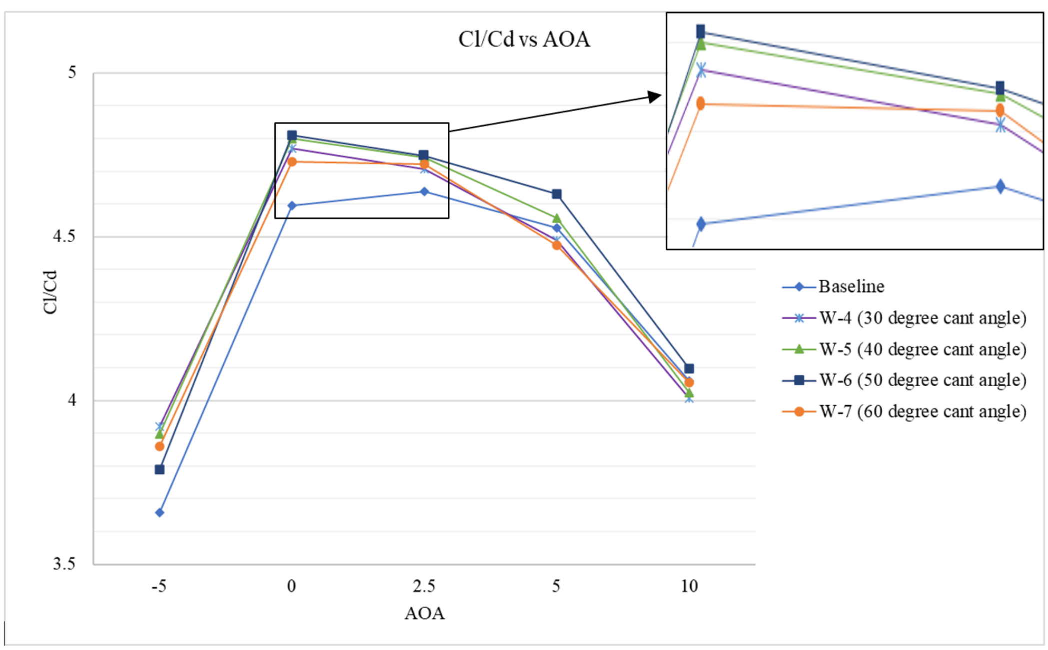

Figure 4.26 C_l/C_d comparison of winglet with S813 profile at 30°, 40°, 50°, and 60°

4.3.1.2 Twist Angle Comparison

The twist angle of winglet 6 was designed to be 10°. To determine either the twist angle was optimum or not, additionally winglet 6 is designed and tested at 0°, 5°, 15° and 20° angle of twist. As shown in figure 4.27 winglet 6 at 5° shows better performance at 2.5° AOA, but it had less performance than both W-6 at 10° and 15° twist angles on other AOA. Also, winglet 6 at 15° twist angle shows a little bit less performance than W-6 at 10° twist angle. The lift to drag ratio at 0° and 20° also shows lower than 5° and 15° respectively. So, winglet 6 with 10° twist angle have better performance than others.

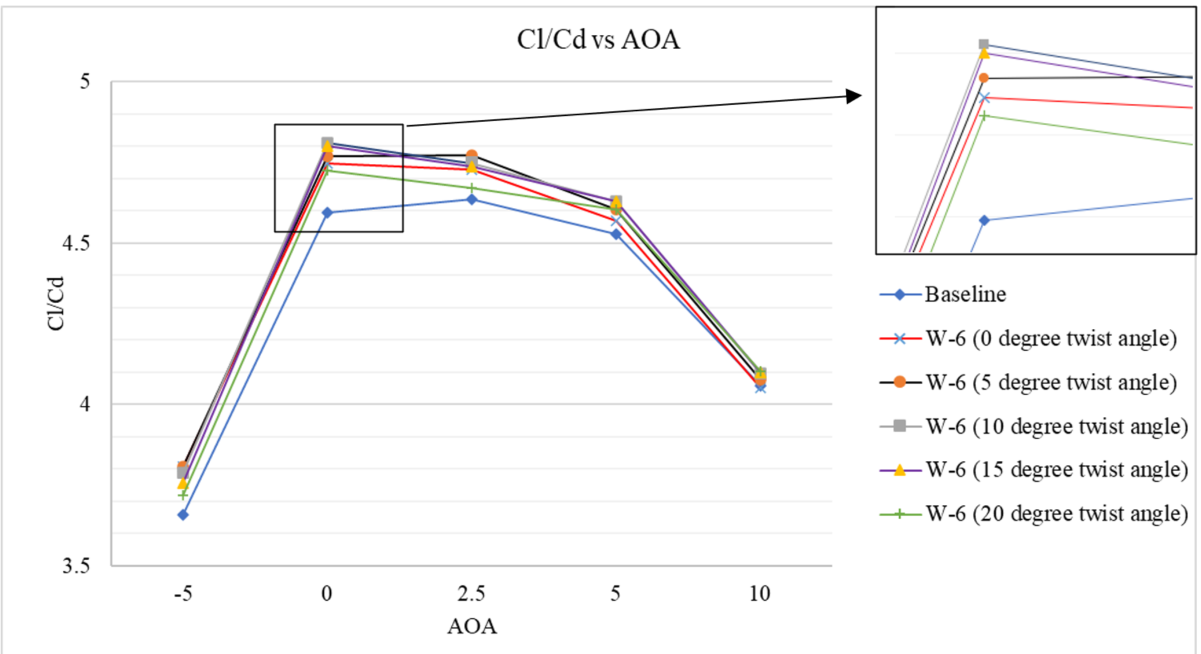

Figure 4.27 C_l/C_d values of blade with W-6 at different winglet twist angles

4.4 Performance Comparison Between Baseline Blade and Blade with Winglet 6

In order to decide the blade with winglet 6 have best performance than the baseline blade aerodynamic performance analysis with comparison based on angle of attack had been discussed in the previous section. In this section, the best performed blade with winglet (blade with W-6) was compared with baseline blade based on different wind speed. The test was conducted at 5m/s, 7m/s, 9m/s, 11m/s, 13m/s and 15m/s at 0° angle of attack, sine best performance of blade with W-6 was at 0° AOA.

As shown in figure 4.28 the lift to drag coefficient ratio of both baseline blade and blade with winglet 6 increases as wind speed increase. An aerodynamic performance improvement of 4.59% to 5% was recorded at different wind speed. Figure 4.28 also demonstrates that the lift to drag coefficient ratio of blade with winglet 6 is better than the baseline blade at all wind velocities.

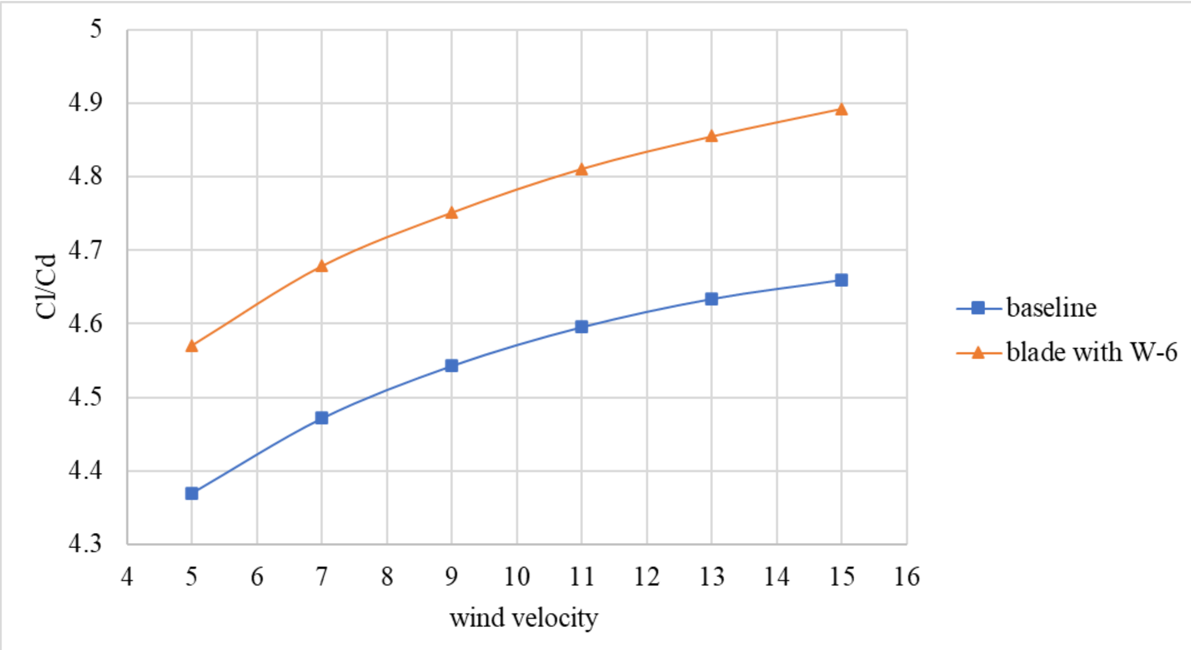

Figure 4.28 C_l/C_d verses wind speed of baseline blade and blade with W-6

The effect of adding winglet on the tip of baseline blade clearly demonstrated in the figure 4.30, 4.31 and 4.32 using a clear view of pressure at 0.95R span wise location of the blade. As shown in figure 4.30, 4.31 and 4.32 the baseline blade was experiencing less pressure than blade with winglet 6 at the pressure side. The colormap of total pressure of the figures indicates a light red for baseline blade and dark red for blade with winglet 6 at pressure side of the blade, which was 31.7-36.4 pa for baseline and 34.2-40 pa for blade with winglet 6 at 7 m/s wind speed. Same colormap effects also shown for 11 m/s and 15 m/s. This pressure difference was the reason that the blade with winglet could able to have higher lift to drag coefficient ratio value than baseline blade.

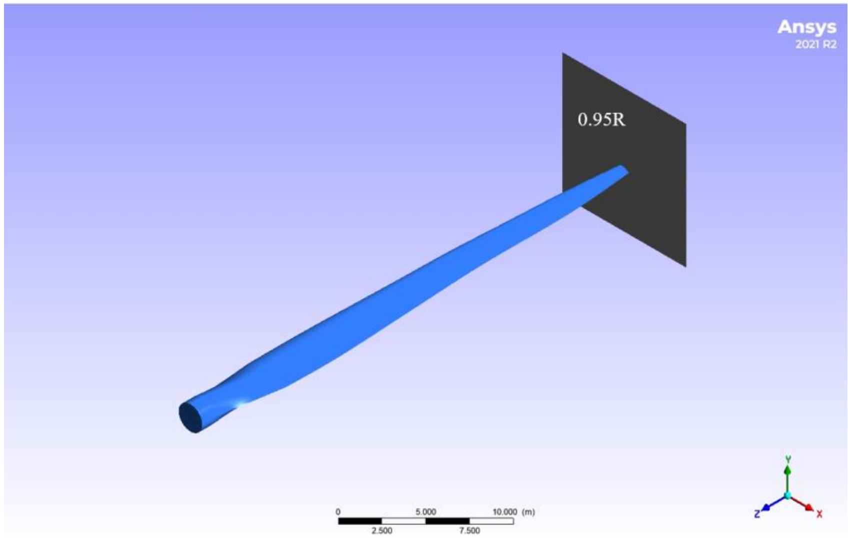

Figure 4.29 Plane at 0.95R of span wise location

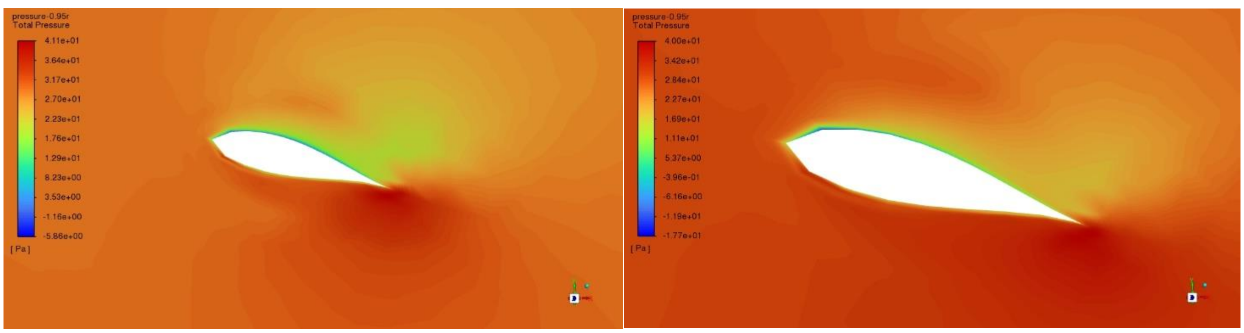

(a) (b)

Figure 4.30 (a) baseline blade and (b) blade with W-6 surface total pressure at 0.95R of blade span and 7 m/s.

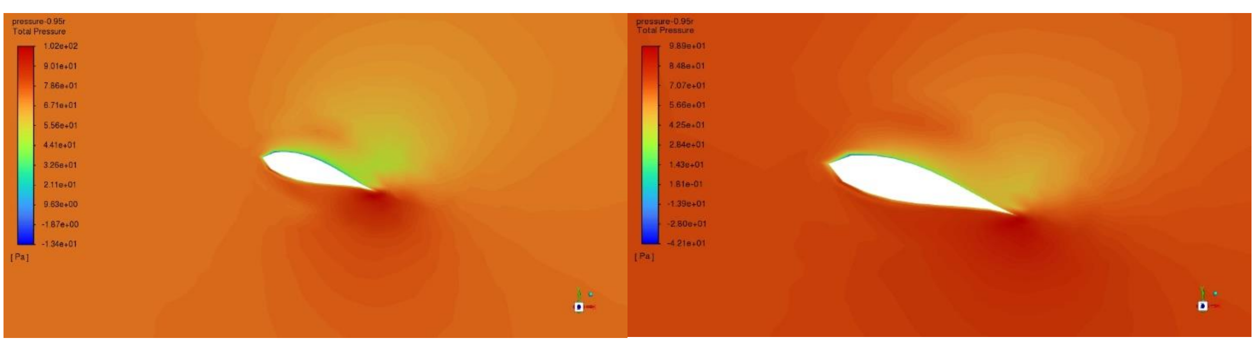

(a) (b)

Figure 4.31 (a) baseline blade and (b) blade with W-6 surface total pressure at 0.95R of blade span and 11 m/s.

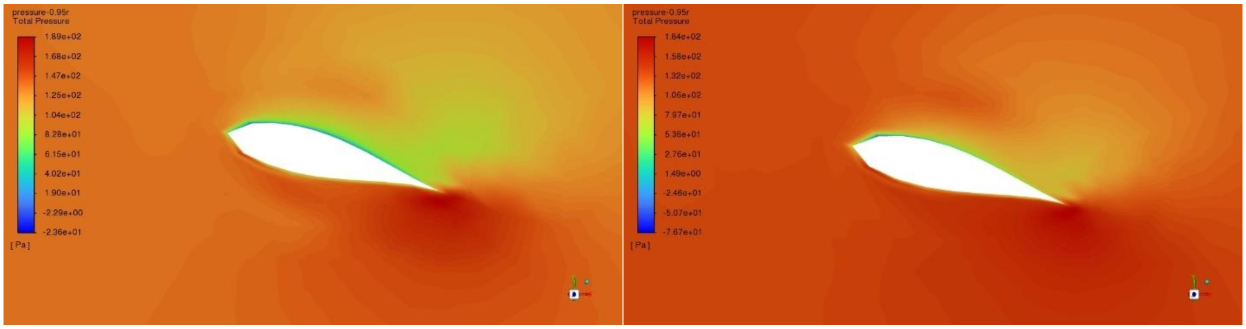

(a) (b)

Figure 4.32 (a) baseline blade and (b) blade with W-6 surface total pressure at 0.95R of blade span and 15 m/s.

Figure 4.33, 4.34 and 4.35 demonstrates that coefficient of pressure values at different sections of the blade. These figures shows that pressure coefficient of the baseline blade is more than blade with winglet 6 at suction side of the blades, which implies that at selected location of blade suction side of the baseline blade experience more pressure than blade with winglet 6. Also, the pressure coefficient of blade with winglet 6 had more values than baseline blade at pressure side of the blade. Which means at some points on pressure side of the blade, the blade with winglet 6 got more pressure than baseline blade.

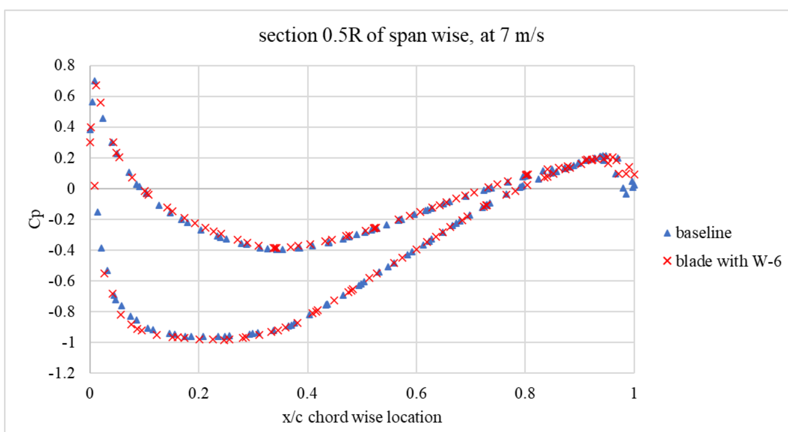

(a)

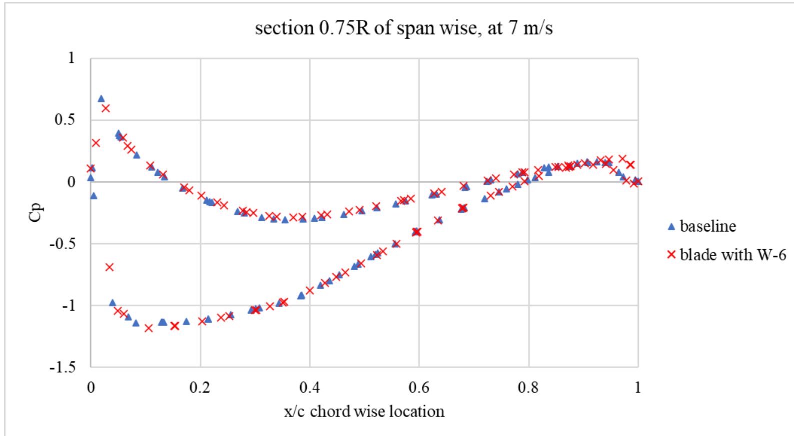

(b)

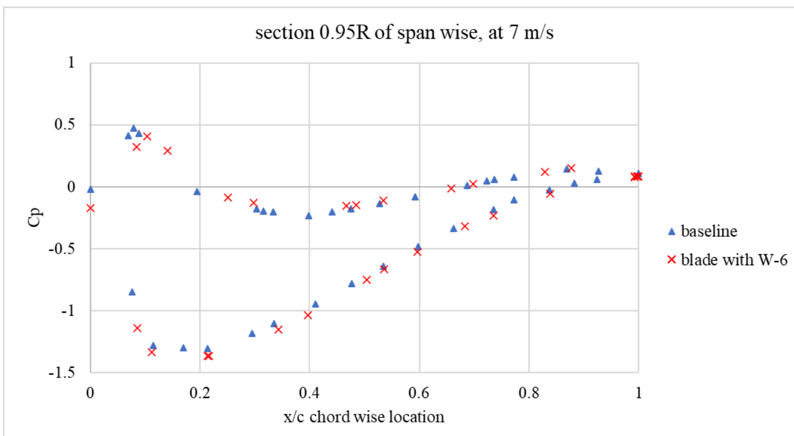

(c)

Figure 4.33 Pressure coefficient of baseline and blade with W-6 at 7 m/s (a) 0.5R, (b) 0.75R and (c) 0.95R span wise location.

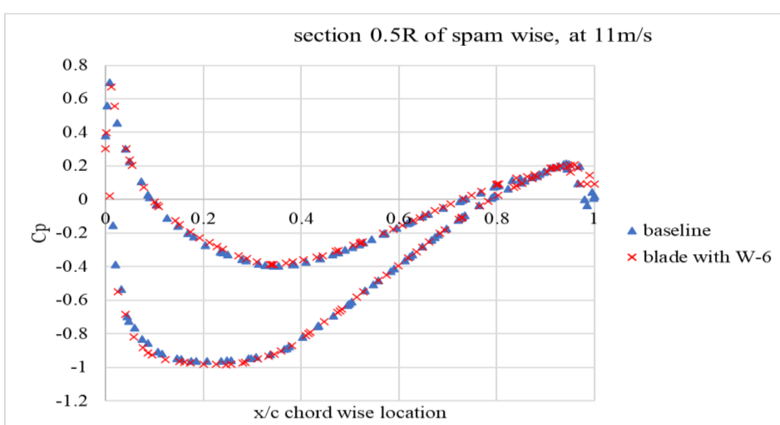

(a)

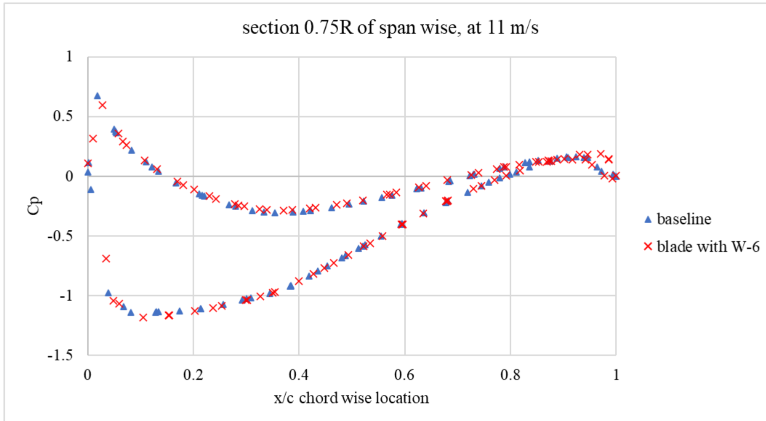

(b)

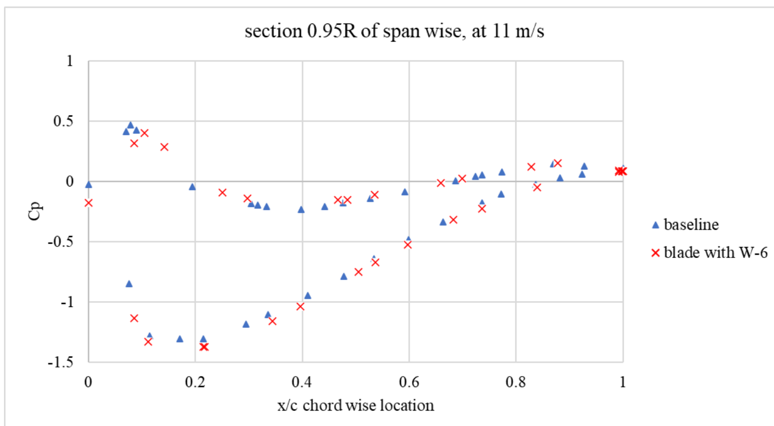

(c)

Figure 4.34 Pressure coefficient of baseline and blade with W-6 at 11 m/s (a) 0.5R, (b) 0.75R and (c) 0.95R span wise location.

(a)

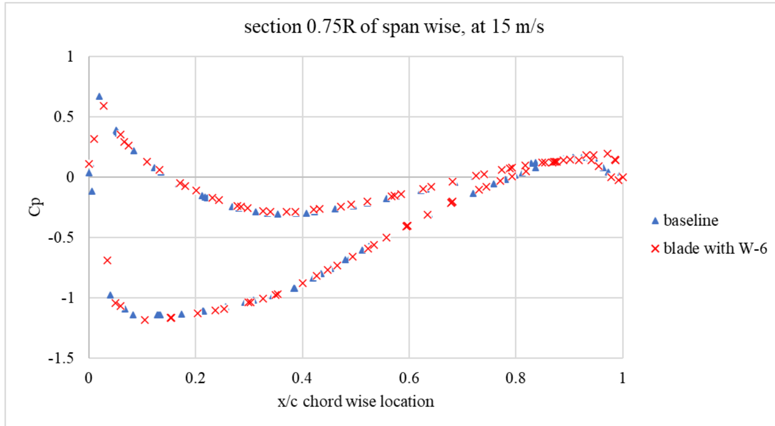

(b)

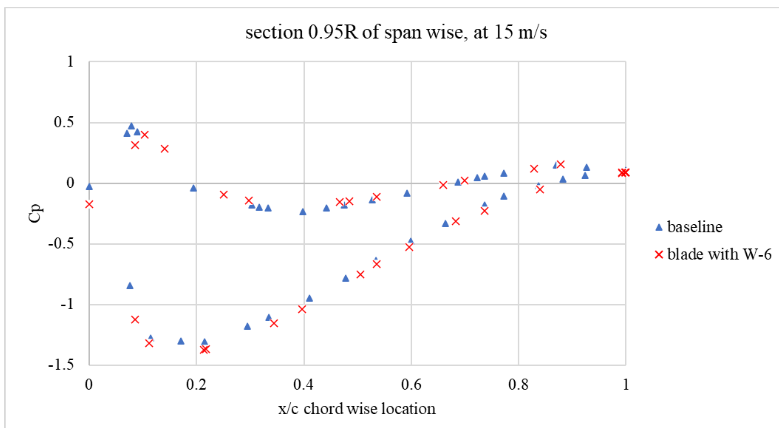

(c)

Figure 4.35 Pressure coefficient of baseline and blade with W-6 at 15 m/s (a) 0.5R, (b) 0.75R and (c) 0.95R span wise location.

Flow Over Split Winglet

Flow over the split winglet was to be maximize the aerodynamic performance of the blade by minimizing drag over the tip of the baseline blade. As shown in figure 4.36 the split winglet maximizes the flow velocity of air over the suction side and this makes the blade to experience less pressure at the suction side of blade tip. Figure 4.36 a, b and c also demonstrates that, as wind speed increases the flow velocity over suction side the winglet increases. The minimized pressure could be expressed as the minimized darg which was induced at the tip of blade.

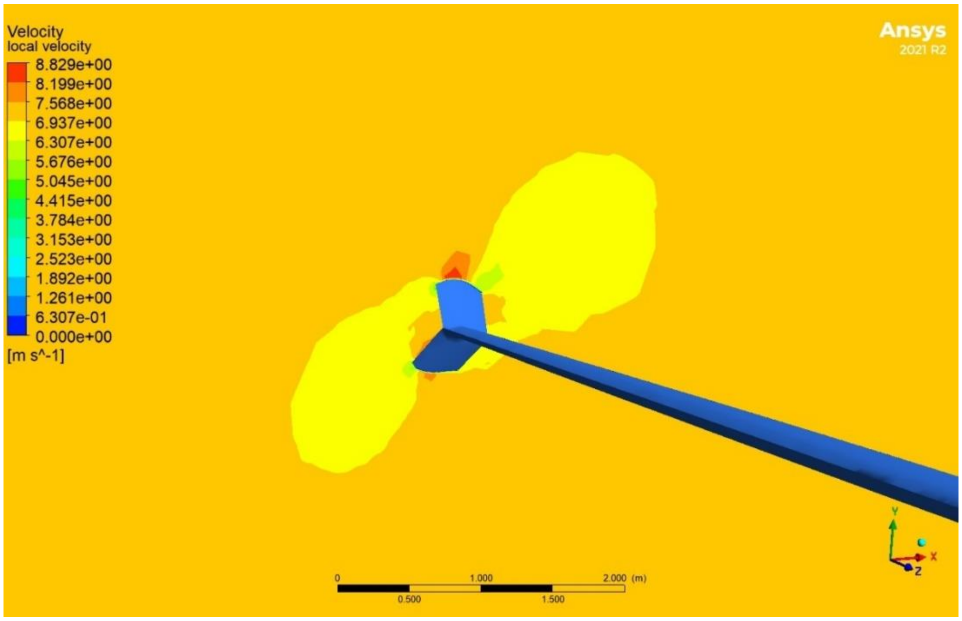
Velocity
local velocity
8.829e+00
8.199e+00
7.568e+00
6.937e+00
6.307e+00
5.676e+00
5.045e+00
4.415e+00
3.784e+00
3.153e+00
2.523e+00
1.892e+00
1.261e+00
6.307e-01
0.000e+00
[m s^-1]
Ansys
2021 R2
0
1.000
2.000 (m)
0.500
1.500
Y
X
Z

(a)

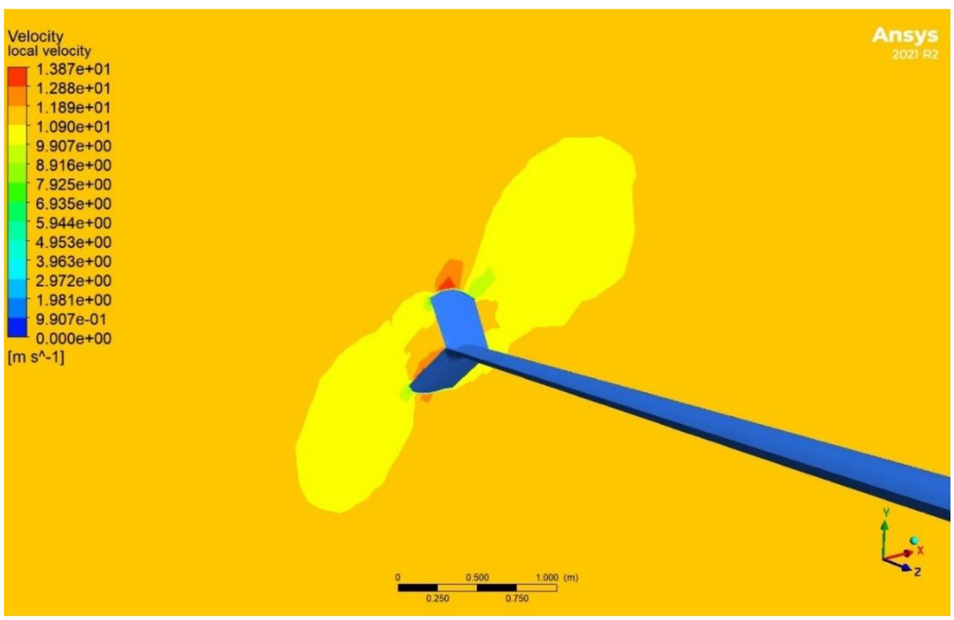
Velocity
local velocity
1.387e+01
1.288e+01
1.189e+01
1.090e+01
9.907e+00
8.916e+00
7.925e+00
6.935e+00
5.944e+00
4.953e+00
3.963e+00
2.972e+00
1.981e+00
9.907e-01
0.000e+00
[m s^-1]
Ansys
2021 R2
0
0.500
1.000 (m)
0.250
0.750
Y
X
Z

(b)

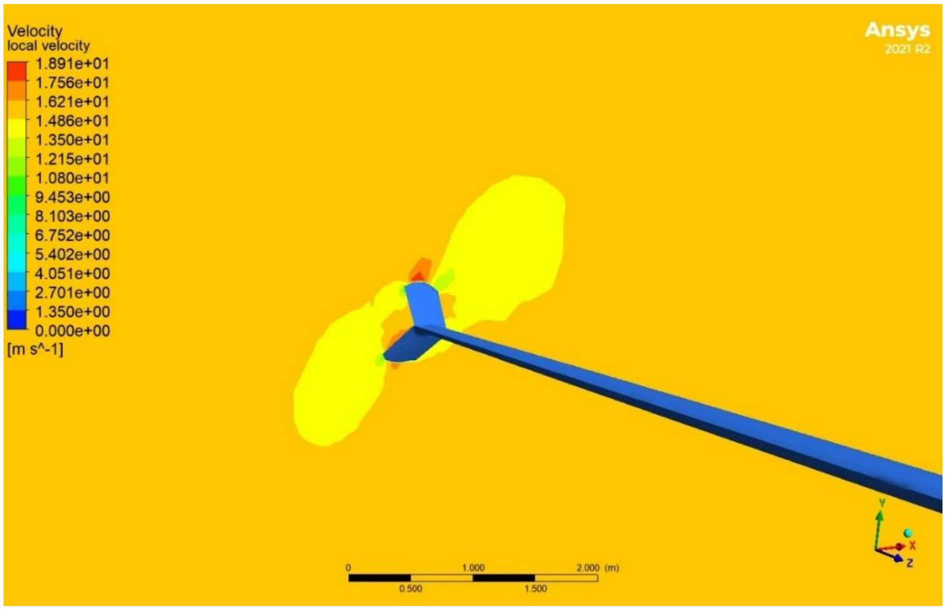

(c)

Figure 4.36 Velocity on split winglet at (a) 7 m/s, (b) 11 m/s and (c) 15 m/s

In this chapter key finding of the research had been discussed as explained in each section of the chapter. The initial gaol of the study was to improve the aerodynamic performance of the blade by adding split winglet at the tip of the blade. Six different types of wiglet configurations labelled using two different airfoil profiles and three different cant angles with the same parametric values of other winglet parameters. Each winglet improved the performance with different values. It was clearly seen that when cant angle of split winglet increases, the aerodynamic performance improvement of the blade increases then reach maximum value after start decreasing. Maximum lift to drag coefficient ratio had recorded at 50º cant angle, In addition to this the aerodynamic performance improvement shows same variational behaviour with twist angle as it shows with cant angle and its maximum value recorded at 10º twist angle. The effect of split winglet was also varied with different wind speed and angle of attack. The aerodynamic performance improvement increased with wind speed. This implies that the split winglet creates an additional load on the blade, so at smaller wind speeds the effect is smaller than higher wind speeds. The improvement which got from this winglet decreases as angle of attack increases and the was due to that the winglet creates more drag at higher angle of attacks than smaller ones. Generally, blades with split winglet could able to produce more energy than blade without split winglets.

CHAPTER FIVE

CONCLUSION AND RECOMMENDATION

5.1 Conclusion

In this thesis, Adama I wind turbine blade were tested with and without split winglet to evaluate aerodynamic performance effect of adding split winglet at tip of turbine blade. These tests were conducted by keeping in mind that one way of improving aerodynamic performance of a wind turbine is to reducing blade tip vortex, those are source of drag.

The study conducted on six types of split winglets by using three different cant and two different airfoil profiles. Other parameters of winglet were kept constant for all winglets. The first three were NACA 634-421 airfoil profile with 30^o, 40^o and 50^o cant angles, 4%R height, 10^o twist angle, and 0^o toe and sweep angles. The rest three were S813 airfoil profile with the same other cant angle, height, twist angle, toe angle and sweep angle. The aerodynamic performance improvement of up to 7.149% and decrement of -1.495% was recorded as those winglets are compared with baseline blade. The blade with split wiglets perform better at lower angle of attacks than upper one. This is due to winglets at higher angle of attacks cause more drag than smaller ones.

The maximum aerodynamic performance was recorded at 15 m/s wind speed and 0^o angle of attack with winglet 6. Addition of winglet 6 on the blade tip of baseline blade had 5% aerodynamic performance (lift to drag coefficient ratio) improvement than baseline blade.

A comparison of winglet parameter was conducted on blade with winglet 6 by changing its cant and twist angles. Additional cant angle of 60^o was tested to check if the aerodynamic performance keeps increasing with cant angle. Twist angles of winglet 6 were also tested at 0^o, 5^o, 10^o, 15^o and 20^o to check their performance. But from all these cases blade with winglet 6 (50^o cant angle and 10^o twist angle) performed better than all other tested designs.

The baseline blade and blade with winglet 6 were tested at different wind speeds. Besides to its aerodynamic improvement, as the wind speed increases the effect of winglet also increased. Therefore, adding split winglet on Adama I wind turbine blade is gives an aerodynamic performance improvement than conventional wind turbine blade.

5.2 Recommendation

Besides to the works caried out in this thesis there are some future works to be conducted in future studies. Researchers to the future should be assessed properly this thesis, they may be also some works to be done beyond the following recommendations:

- From all winglet parameters cant angle and twist angle were studied at different values, so for future, it is recommended to study effects of changing values of other parameters like height, sweep angle and toe angle.
- This study was conducted on two types of airfoil profiles for winglet design. For future studies, investigate the effect of more winglet's airfoil profile.
- For future studies effects of split winglets can be evaluated experimentally using a proper wind tunnel test or with field studies.
- Investigate aero-elastic (deformation and vibration), Wake interface and aero-acoustic (noise) effects of the split winglet.
- The study had been caried out by RANS (k-ω SST turbulence model) method, though researchers should conduct the study using LES or DNS method for more accuracy.

REFERENCE

Abdelghany, E. S., Sarhan, H. H., Alahmadi, R., & Farghaly, M. . (2023). Study the Effect of Winglet Height Length on the Aerodynamic Computational Investigation. *Energies*, *16*. https://doi.org/10.3390/en16135138

AirfoilTools.com. (2024). *Airfoil Tools*. http://airfoiltools.com

ANSYS, I. (2021). *Ansys Fluent Theory Guide*. http://www.ansys.com

Aravindkumar, N., Karthick, P., Karan, M., Manoj, Y., Nagaraj, G., & Babu, C. (2021). Optimization of Winglet of a Wind Turbine Blade Retraction Retraction : Optimization of Winglet of a Wind Turbine Blade. *In IOP Conference Series: Materials Science and Engineering*, *1145*(1), 012028. https://doi.org/10.1088/1757-899X/1145/1/012147

Burton, T., Sharpe, D., Jenkins, N., & Bossanyi, E. (2001). *Wind Energy HandBook*. John Wiley & Sons.

Contreras, L. T., Lain, S., & Ilinca, A. (2022). A Review on the Estimation of Power Loss Due to Icing in Wind Turbines. *Energies*, *15*(3). https://doi.org/10.3390/en15031083

Dejene, G., Ancha, V. R., & Bekele, A. (2024). NREL Phase VI wind turbine blade tip with S809 airfoil profile winglet design and performance analysis using computational fluid dynamics. *Cogent Engineering*, *11*(1). https://doi.org/10.1080/23311916.2023.2293562

Dejene, G., Ramayya, V., & Bekele, A. (2024). Investigation of NREL Phase VI wind turbine blade with different winglet configuration for performance augmentation. *International Journal of Sustainable Energy*, *43*(1). https://doi.org/10.1080/14786451.2024.2321622

Farhan, A., Hassanpour, A., Burns, A., & Motlagh, Y. G. (2019). Numerical study of effect of winglet planform and airfoil on a horizontal axis wind turbine performance. *Renewable Energy*, *131*, 1255–1273. https://doi.org/10.1016/j.renene.2018.08.017

Fikade, G., Bekele, A., Venkatachalam, C., & Parthiban, M. (2020). Effects of Dimples on Aerodynamic Performance of Horizontal Axis Wind Turbine Blades. *International Research Journal of Engineering and Technology (IRJET)*, *07*(01), 525–539.

Goldwind. (2011). *Goldwind 1.5MW Wind Turbine Generator System Operation and Maintenance Manual*.

Goldwind, & TianYuan, C. (2011). *WTG suitability report of Adama Wind Farm , Ethiopia*.

Gupta, A., & Amano, R. S. (2012). CFD ANALYSIS OF WIND TURBINE BLADE WITH WINGLETS. *In International Design Engineering Technical Conferences and Computers and Information in Engineering Conference*, *45042*, 843–849. https://doi.org/10.1115/DECT2012-70679

Hailu, A. D., & Kumsa, D. K. (2021). Ethiopia renewable energy potentials and current state. *AIMS Energy*, *9*(1). https://doi.org/10.3934/ENERGY.2021001

He, Y., & Agarwal, R. K. (2014). Shape Optimization of NREL S809 Airfoil for Wind Turbine Blades Using a Multiobjective Genetic Algorithm. *Hindawi Publishing Corporation, International Journal of Aerospace Engineering*, *2014*. https://doi.org/10.1155/2014/864210

IEA. (2021). Renewables 2021: Analysis and Forecast to 2026. *Paris*. https://doi.org/10.1002/peng.20026

Karim, M. M., Rahman, M. M., & Alim, M. A. (2011). PERFORMANCE OF SST k- ω TURBULENCE MODEL FOR COMPUTATION OF VISCOUS DRAG OF AXISYMMETRIC UNDERWATER BODIES. *International Journal of Engineering*, *24*(2), 139–146. https://sid.ir/paper/585300/en

Khalafallah, M. G., Ahmed, A. M., & Emam, M. K. (2019). The effect of using winglets to enhance the performance of swept blades of a horizontal axis wind turbine. *Advances in Mechanical Engineering*, *11*(9). https://doi.org/10.1177/1687814019878312

Khaled, M., Ibrahim, M. M., Abdel Hamed, H. E., & AbdelGwad, A. F. (2019). Investigation of a small Horizontal–Axis wind turbine performance with and without winglet. *Energy*, *187*, 115921. https://doi.org/10.1016/j.energy.2019.115921

Khan, N A & Islam, M. Q. (2021). Study on the effects of winglets : wind turbine blades having circular arc blade section profile. *International Journal of Energy and Environmental Engineering*, *12*(4), 837–853. https://doi.org/10.1007/s40095-021-00414-z

Kulak, M., Lipian, M., & Zawadzki, K. (2020). Investigation of performance of small wind turbine blades with winglets. *International Journal of Numerical Methods for Heat and Fluid Flow*, *31*(2), 629–640. https://doi.org/10.1108/HFF-09-2019-0695

Manwell, J. F., McGowan, J. G., & Rogers, A. L. (2009). *WIND ENERGY EXPLAINED*.

Mourad, M. G., Mekhail, T. A., Shahin, I., & Abdellatif, O. E. (2020). Effect of winglet geometry on horizontal axis wind turbine performance. *Engineering Reports*, *2*(1). https://doi.org/10.1002/eng2.12101

Muiruri, P. I., Motsamai, O. S., & Ndeda, R. (2019). A comparative study of RANS - based turbulence models for an upscale wind turbine blade. *SN Applied Sciences*, *1*(3), 237. https://doi.org/10.1007/s42452-019-0254-5

Mumu, T. A., Islam, Q., & Arif, M. D. (2023). Investigation on Torque Coefficients of Horizontal Axis Wind Turbine with Symmetrical and Asymmetrical Split-tip Winglets. *International Conference on Mechanical Engineering*, *14*(12), 1–6. https://doi.org/10.2139/ssrn.4860862

Pillai, P. S., & Harikumar, A. R. (2021). The effects of winglet on hawt blade and the optimum ratio between wing and winglet dimensions The effects of winglet on hawt blade and the optimum ratio between wing and winglet dimensions. *In IOP Conference Series: Materials Scince and Engineering*, *1114*. https://doi.org/10.1088/1757-899X/1114/1/012049

Saravanan, P., Parammasivam, K. M., & S, S. R. (2013). Experimental Investigation on Small Horizontal Axis Wind Turbine Rotor Using Winglets. *Journal of Applied Science and Engineering*, *16*(2), 159–164. https://doi.org/10.6180/jase.2013.16.2.07

Sayed, M. A., Kandil, H. A., & Shaltot, A. (2012). Aerodynamic analysis of different wind-turbine-blade profiles using finite-volume method. *Energy Conversion and Management*. https://doi.org/10.1016/j.enconman.2012.05.030

Snel, H. (2003). Review of Aerodynamics for Wind Turbines. *Wind Energ*, *6*, 203–211. https://doi.org/10.1002/we.97

Sorensen, J. N., & Shen, W. Z. (2002). Numerical modeling of wind turbine wakes. *Journal of Fluids Engineering, Transactions of the ASME*, *124*(2), 393–399. https://doi.org/10.1115/1.1471361

Sy, M. S., Abuan, B. E., Angelo, L., & Danao, M. (2020). Aerodynamic Investigation of a Horizontal Axis Wind Turbine with Split Winglet Using Computational Fluid Dynamics. *Energies*, *13*(18). https://doi.org/10.3390/en13184983

Talukder, M. M. M., Islam, M. K., & Rukan, M. R. (2016). Comparative Aerodynamic Analysis of Wind Turbine Blade Profiles. *International Journal of Engineering Research & Technology (IJERT)*, *5*(01), 96–102.

Tangier, J. L., & Somers, D. M. (1995). NREL Airfoil Families for HAWTs. *National Renewable Energy Laboratory (NREL), Golden, CO (United States)*. https://doi.org/10.2172/10106095

United Nations Economic Commission for Africa. (2015). *Inclusive Green Growth in Ethiopia: Selected case studies*. ECA Publishing and Distribution Unit.

Verma, S., Paul, A. R., & Jain, A. (2021). Performance investigation and energy production of a novel horizontal axis wind turbine with winglet. *International Journal of Energy Research*, *46*(4), 4947–4964. https://doi.org/10.1002/er.7488

Versteeg, H. K., & Malalasekera, W. (2007). *An Introduction to Computational Fluid Dynamics* (Vol. 2).

Weatherguardwind.com. (2020). *Adding Winglets On Wind Turbine Blades: Worth The Cost?* https://weatherguardwind.com/winglets-on-wind-turbine-blades/

Weierman, J., & Jacob, J. D. (2010). Winglet design and optimization for UAVs. *28th AIAA Applied Aerodynamics Conference*, *1*. https://doi.org/10.2514/6.2010-4224

White, F. M. (2011). Fluid Mechanics. *McGraw-Hill Companies, Inc*.

Zhang, Z., Kuang, L., Han, Z., Zhou, D., Zhao, Y., Bao, Y., Duan, L., Tu, J., Chen, Y., & Chen, M. (2023). Comparative analysis of bent and basic winglets on performance improvement of horizontal axis wind turbines. *Energy*, *281*, 128252. https://doi.org/10.1016/j.energy.2023.128252

Zhu, B., Sun, X., Wang, Y., & Huang, D. (2016). Performance characteristics of a horizontal axis turbine with fusion winglet. *Energy*, *120*, 431–440. https://doi.org/10.1016/j.energy.2016.11.094

APPENDIX

A-1 Aerodynamic Properties of NACA 634-421, S813, S810, and S820 airfoils.

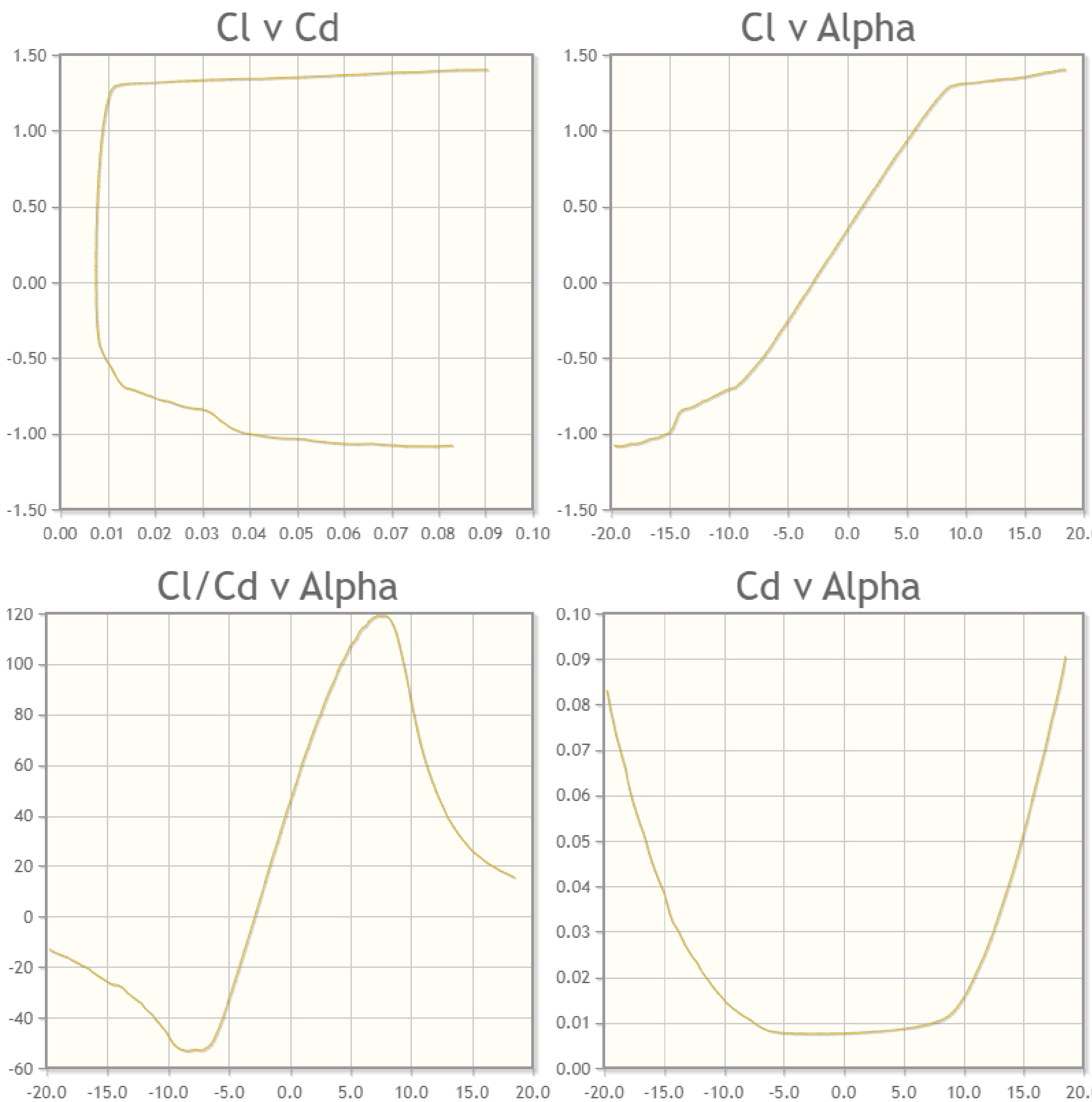

Figure: Aerodynamic Performance of NACA 634-421 airfoil (AirfoilTools.com, 2024).

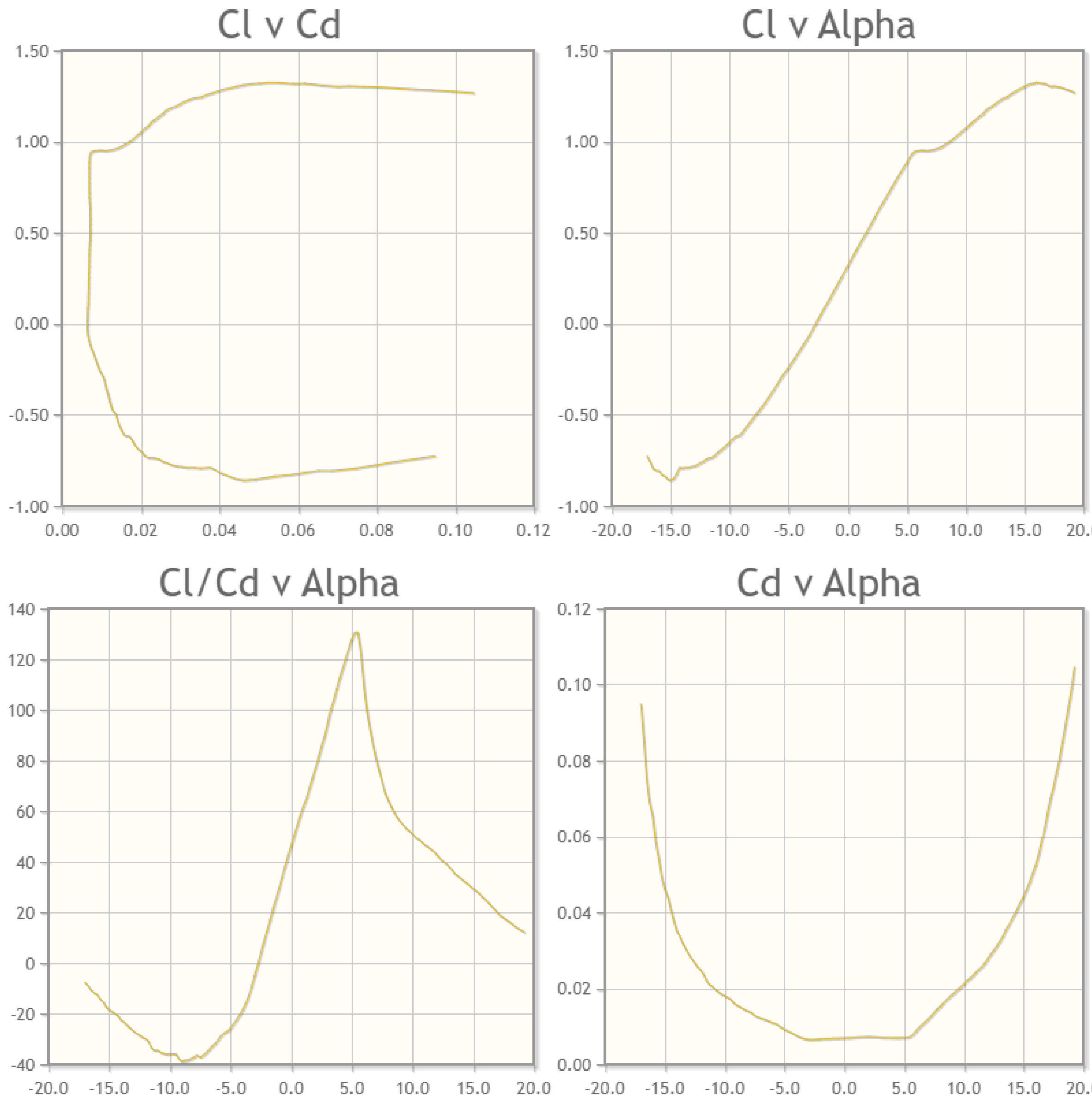

Figure: Aerodynamic Performance of S813 airfoil (AirfoilTools.com, 2024).

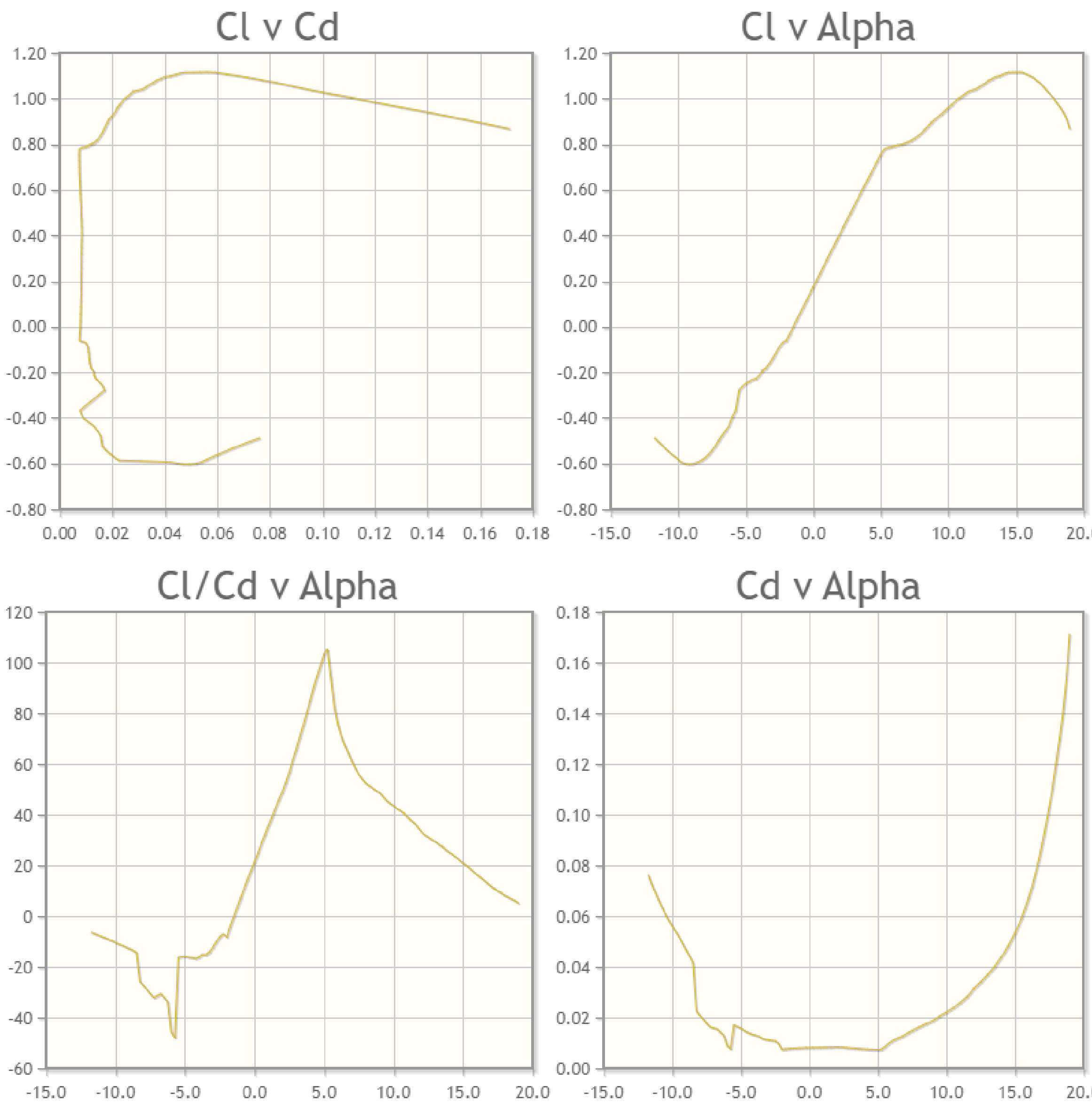

Figure: Aerodynamic Performance of S810 Airfoil (AirfoilTools.com, 2024).

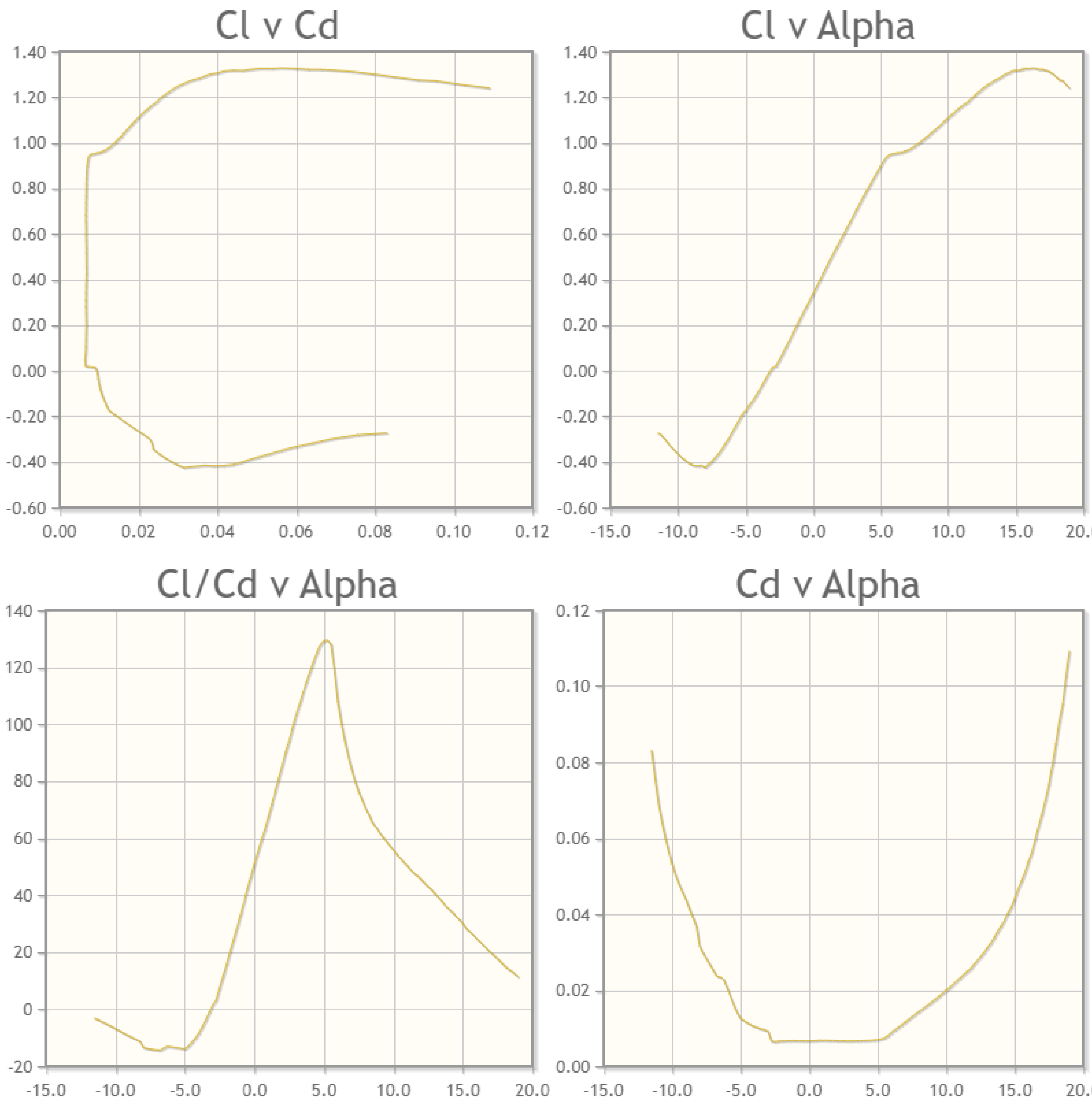

Figure: Aerodynamic Performance of S820 Airfoil (AirfoilTools.com, 2024).

A-2 Grid Independence Test Mesh-Setup

Details of "Mesh"

Display	
Display Style	Use Geometry Setting
Defaults	
Physics Preference	CFD
Solver Preference	Fluent
Element Order	Linear
Element Size	7.0 m
Export Format	Standard
Export Preview Surface Mesh	No
Sizing	
Use Adaptive Sizing	No
Growth Rate	Default (1.2)
Max Size	Default (14.0 m)
Mesh Defeaturing	Yes
Defeature Size	Default (3.5e-002 m)
Capture Curvature	Yes
Curvature Min Size	Default (7.e-002 m)
Curvature Normal Angle	Default (18.0°)
Capture Proximity	No
Bounding Box Diagonal	268.94 m
Average Surface Area	7603.8 m^2
Minimum Edge Length	1.0993e-003 m
Quality	
Inflation	
Advanced	
Statistics	
Nodes	118837
Elements	519275

Figure: mesh-1 setup

Details of "Mesh"

Display	
Display Style	Use Geometry Setting
Defaults	
Physics Preference	CFD
Solver Preference	Fluent
Element Order	Linear
Element Size	7.0 m
Export Format	Standard
Export Preview Surface Mesh	No
Sizing	
Use Adaptive Sizing	No
Growth Rate	Default (1.2)
Max Size	Default (14.0 m)
Mesh Defeaturing	Yes
Defeature Size	Default (3.5e-002 m)
Capture Curvature	Yes
Curvature Min Size	Default (7.e-002 m)
Curvature Normal Angle	Default (18.0°)
Capture Proximity	No
Bounding Box Diagonal	268.94 m
Average Surface Area	7603.8 m^2
Minimum Edge Length	1.0993e-003 m
Quality	
Inflation	
Advanced	
Statistics	
Nodes	153819
Elements	617862

Figure: mesh-2 setup

Details of "Mesh"	
Display	
Display Style	Use Geometry Setting
Defaults	
Physics Preference	CFD
Solver Preference	Fluent
Element Order	Linear
Element Size	7.0 m
Export Format	Standard
Export Preview Surface Mesh	No
Sizing	
Use Adaptive Sizing	No
Growth Rate	Default (1.2)
Max Size	Default (14.0 m)
Mesh Defeaturing	Yes
Defeature Size	Default (3.5e-002 m)
Capture Curvature	Yes
Curvature Min Size	Default (7.e-002 m)
Curvature Normal Angle	Default (18.0°)
Capture Proximity	No
Bounding Box Diagonal	268.94 m
Average Surface Area	7603.8 m^2
Minimum Edge Length	1.0993e-003 m
Quality	
Inflation	
Advanced	
Statistics	
Nodes	221816
Elements	808702

Figure mesh-3 setup

Details of "Mesh"	
Display	
Display Style	Use Geometry Setting
Defaults	
Physics Preference	CFD
Solver Preference	Fluent
Element Order	Linear
Element Size	7.0 m
Export Format	Standard
Export Preview Surface Mesh	No
Sizing	
Use Adaptive Sizing	No
Growth Rate	Default (1.2)
Max Size	Default (14.0 m)
Mesh Defeaturing	Yes
Defeature Size	Default (3.5e-002 m)
Capture Curvature	Yes
Curvature Min Size	Default (7.e-002 m)
Curvature Normal Angle	Default (18.0°)
Capture Proximity	No
Bounding Box Diagonal	268.94 m
Average Surface Area	7603.8 m^2
Minimum Edge Length	1.0993e-003 m
Quality	
Inflation	
Advanced	
Statistics	
Nodes	408741
Elements	1315878

Figure: mesh-4 setup

Details of "Mesh"

Display	
Display Style	Use Geometry Setting
Defaults	
Physics Preference	CFD
Solver Preference	Fluent
Element Order	Linear
Element Size	7.0 m
Export Format	Standard
Export Preview Surface Mesh	No
Sizing	
Use Adaptive Sizing	No
Growth Rate	Default (1.2)
Max Size	Default (14.0 m)
Mesh Defeaturing	Yes
Defeature Size	Default (3.5e-002 m)
Capture Curvature	Yes
Curvature Min Size	Default (7.e-002 m)
Curvature Normal Angle	Default (18.0°)
Capture Proximity	No
Bounding Box Diagonal	268.94 m
Average Surface Area	7603.8 m^2
Minimum Edge Length	1.0993e-003 m
Quality	
Inflation	
Advanced	
Statistics	
Nodes	587449
Elements	1790211

Figure: mesh-5 setup

A-3 ANSYS Fluent Lift and Drag Coefficient Result Plot

Baseline Blade Lift and Drag Coefficient at Different Wind Speed

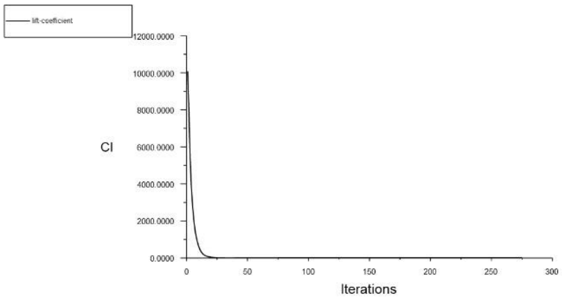

Figure: C_l at 5 m/s

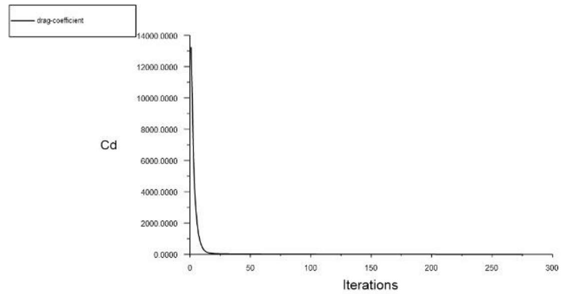

Figure: C_d at 5 m/s

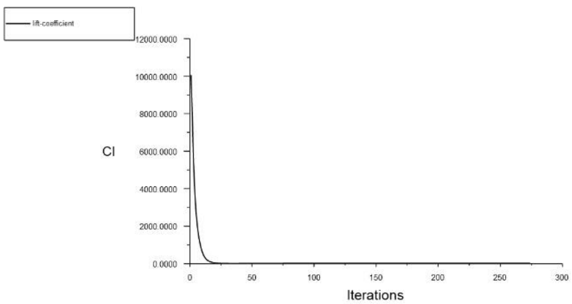

Figure: C_l at 7 m/s

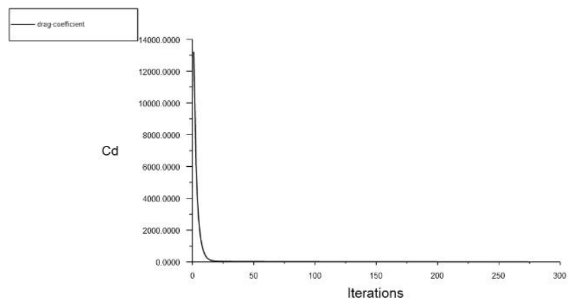

Figure: C_d at 7 m/s

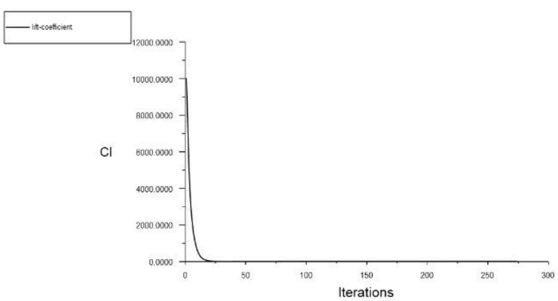

Figure: C_l at 9 m/s

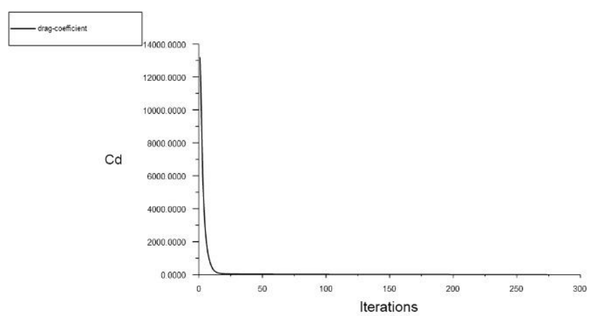

Figure: C_d at 9 m/s

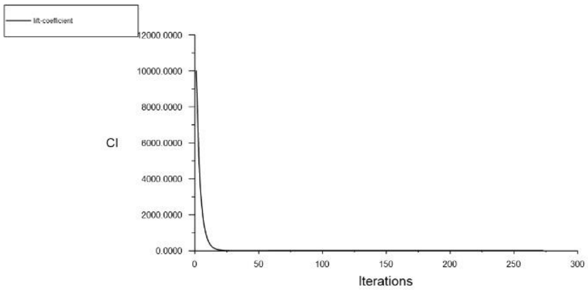

Figure: C_l at 11 m/s

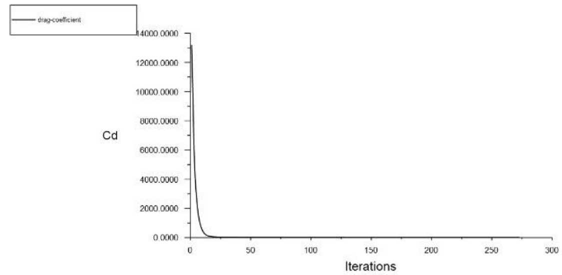

Figure: C_d at 11 m/s

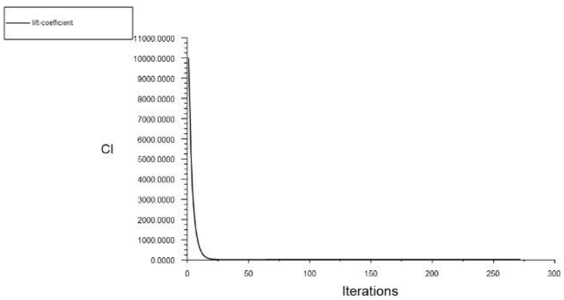

Figure: C_l at 13 m/s

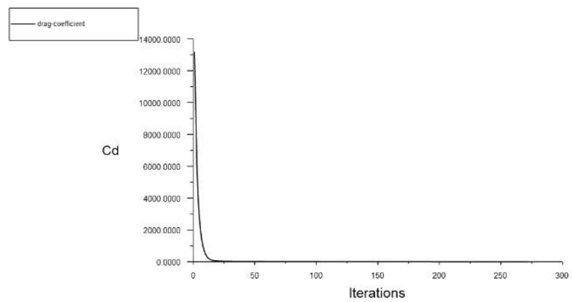

Figure: C_d at 13 m/s

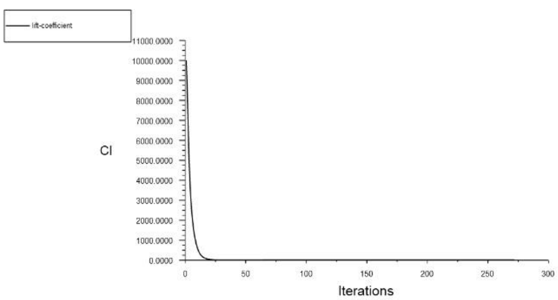

Figure: C_l at 15 m/s

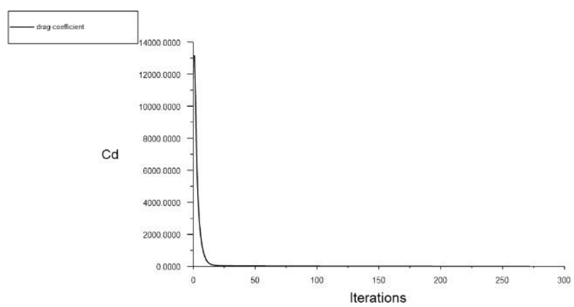

Figure: C_d at 15 m/s

Blade with winglet-6 Lift and Drag Coefficient at Different Wind Speed

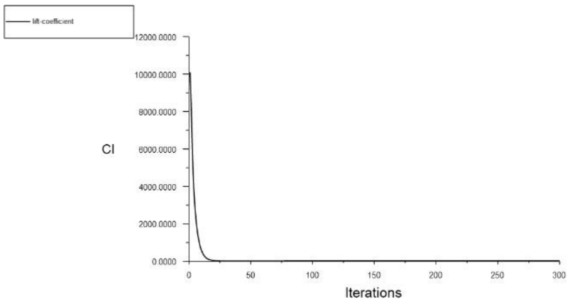

Figure: C_l at 5 m/s

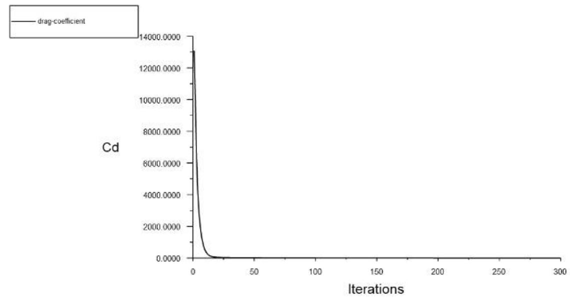

Figure: C_d at 5 m/s

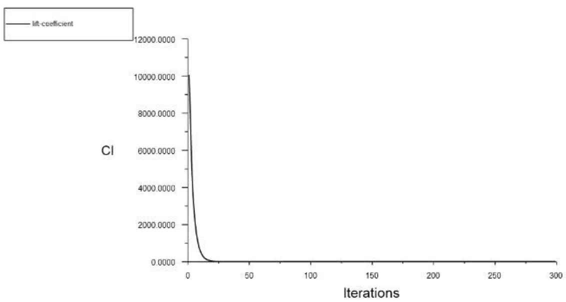

Figure: C_l at 7 m/s

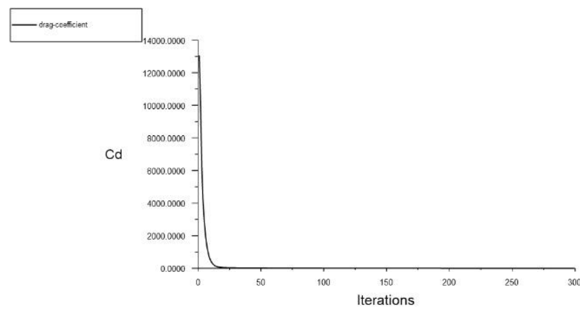

Figure: C_d at 7 m/s

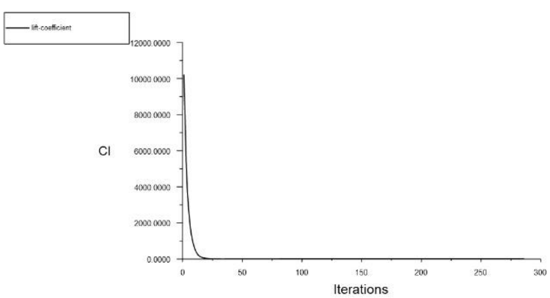

Figure: C_l at 9 m/s

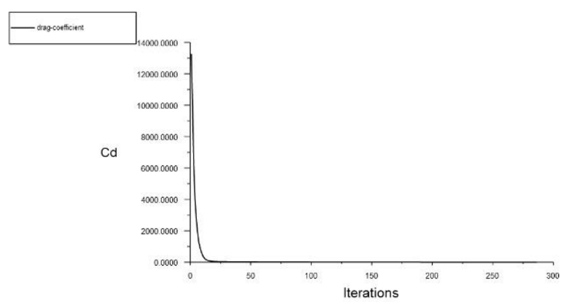

Figure: C_d at 9 m/s

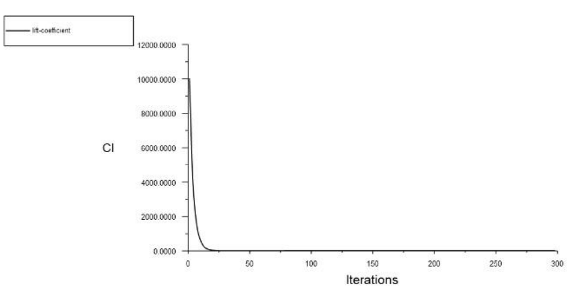

Figure: C_l at 11 m/s

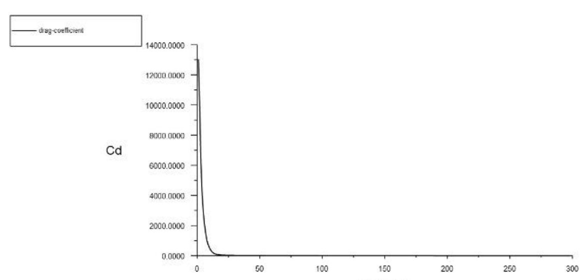

Figure: C_d at 11 m/s

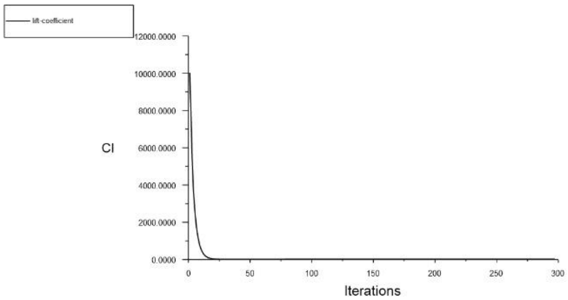

Figure: C_l at 13 m/s

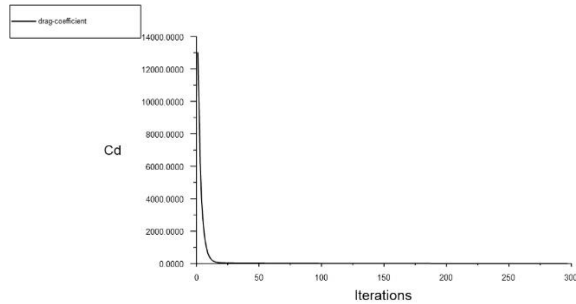

Figure: C_d at 13 m/s

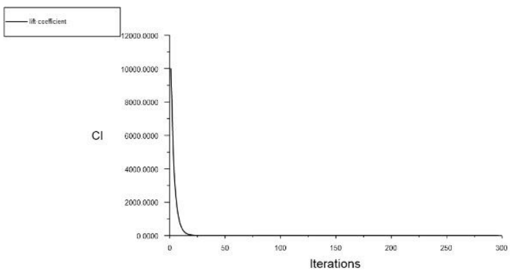

Figure: C_l at 15 m/s

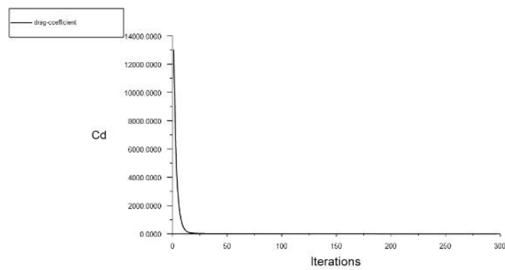

Figure: C_d at 15 m/s

Baseline Blade Lift Coefficient Plot at Different Angle of Attack

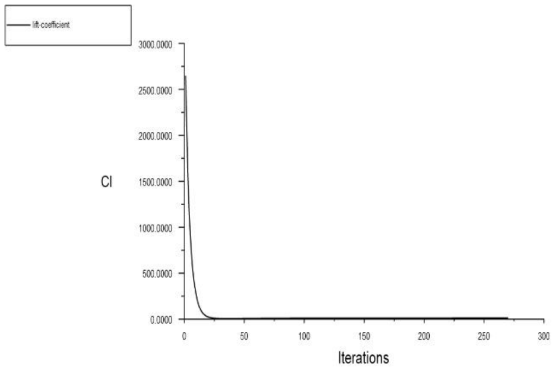

Figure: -5º AOA

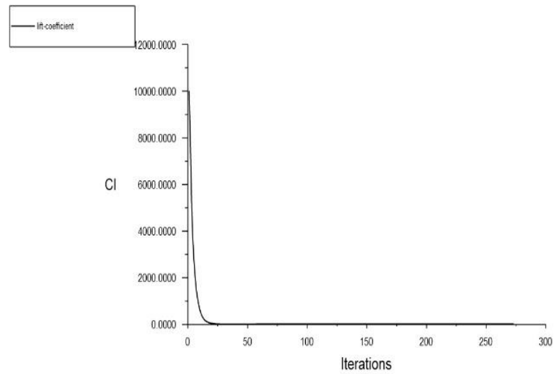

Figure: 0º AOA

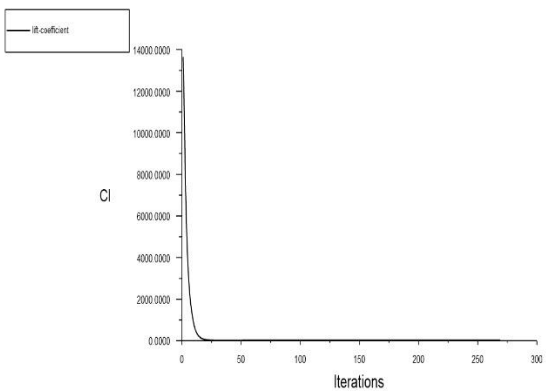

Figure: 2.5º AOA

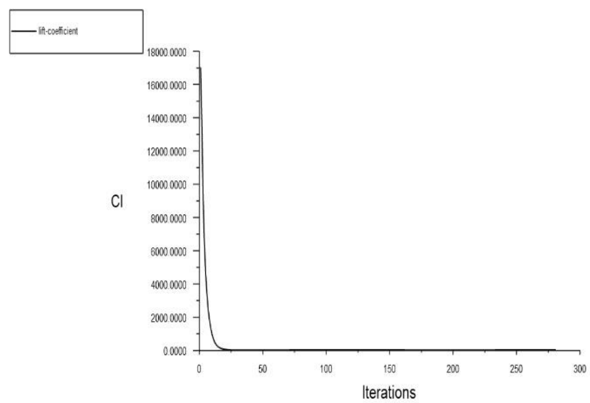

Figure: 5º AOA

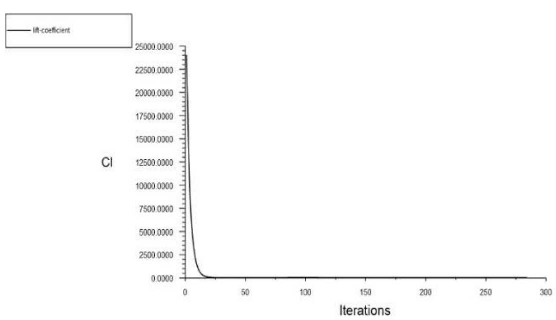

Figure: 10º AOA

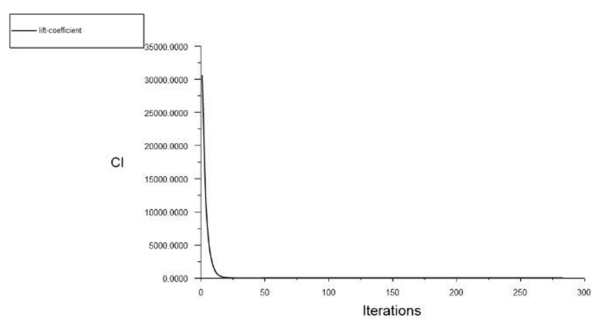

Figure: 15º AOA

Baseline Blade Drag Coefficient Plot at Different Angle of Attack

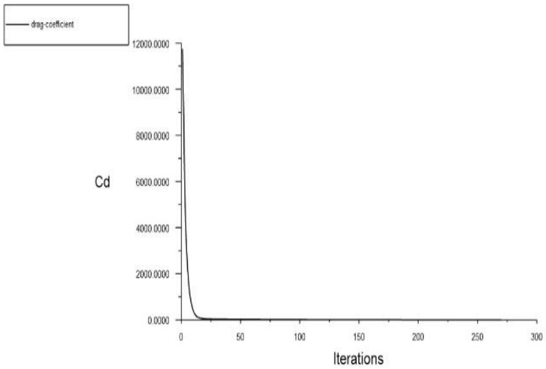

Figure: -5º AOA

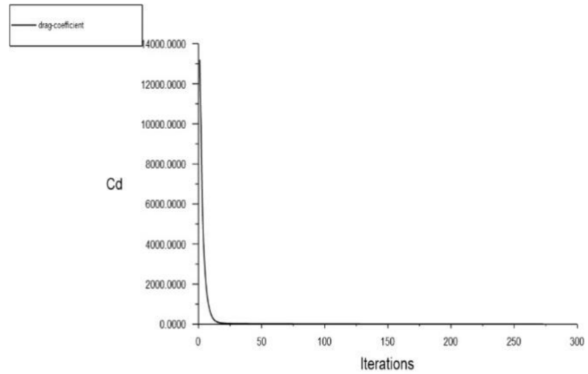

Figure: 0º AOA

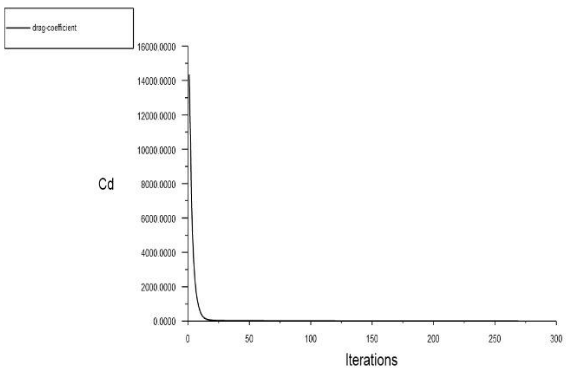

Figure: 2.5º AOA

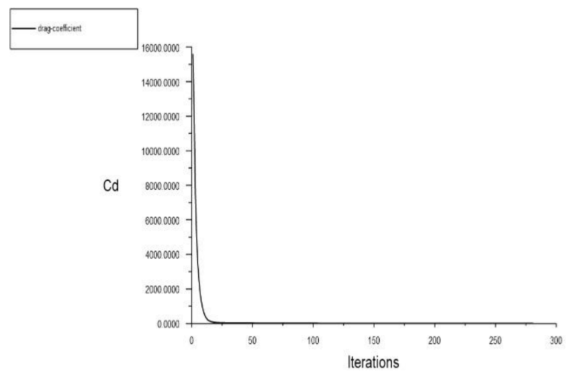

Figure: 5º AOA

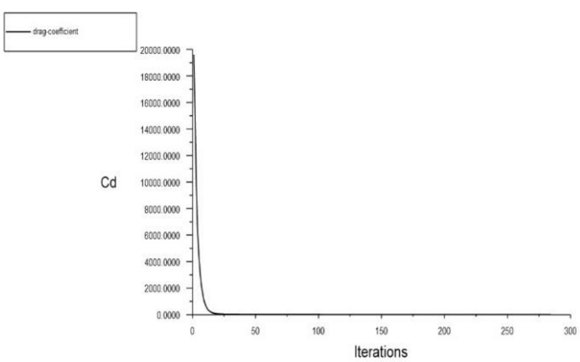

Figure: 10º AOA

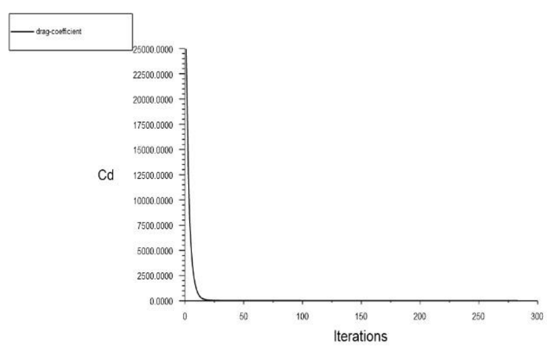

Figure: 15º AOA

Winglet-1 Blade Lift Coefficient Plot at Different Angle of Attack

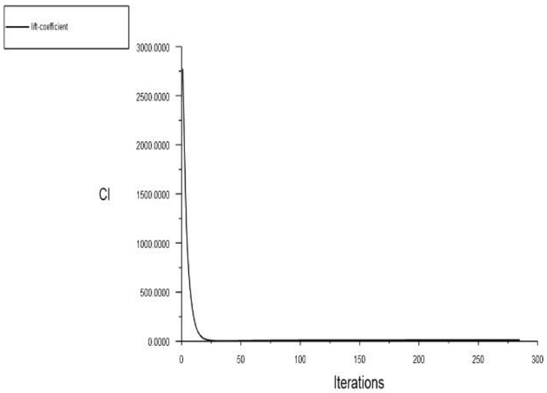

Figure: -5º AOA

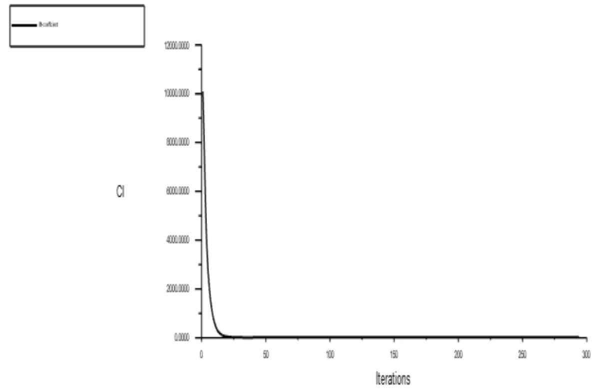

Figure: 0º AOA

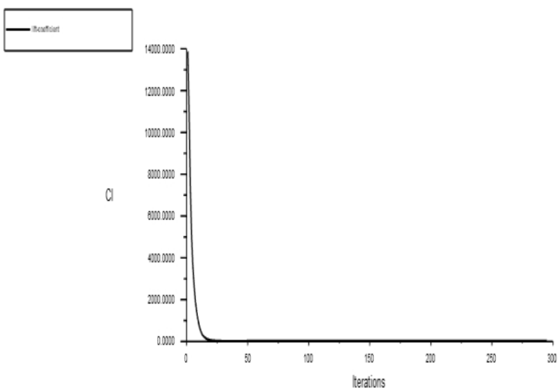

Figure: 2.5º AOA

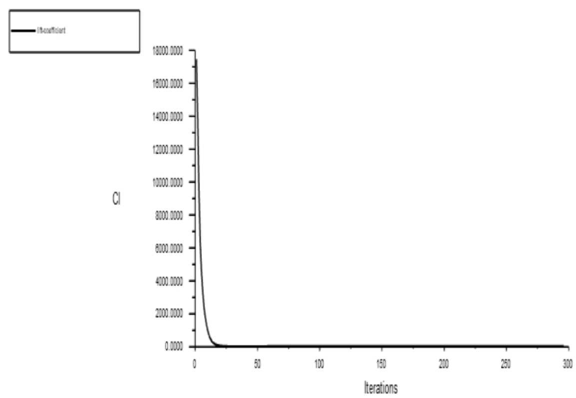

Figure: 5º AOA

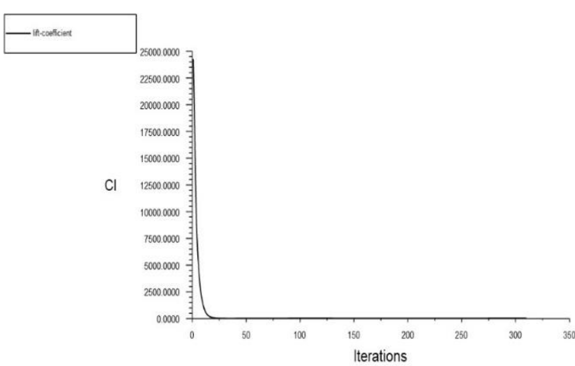

Figure: 10º AOA

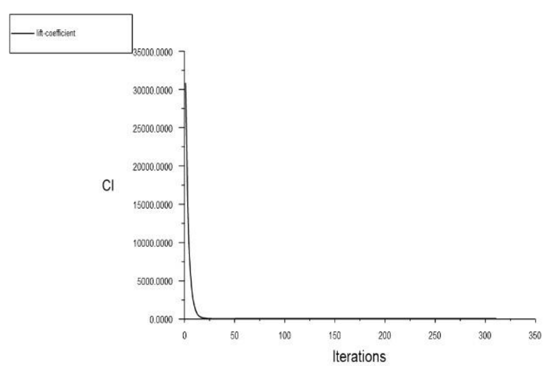

Figure: 15º AOA

Winglet-1 Blade Drag Coefficient Plot at Different Angle of Attack

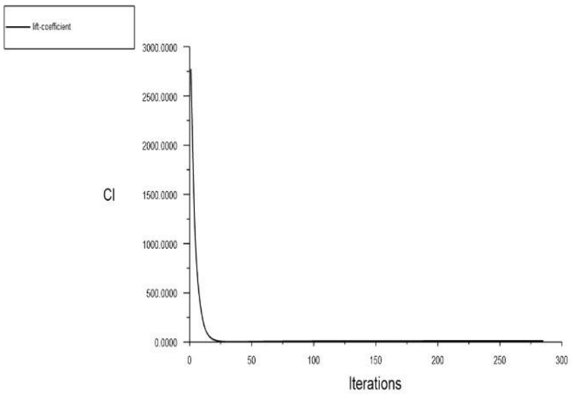

Figure: -5º AOA

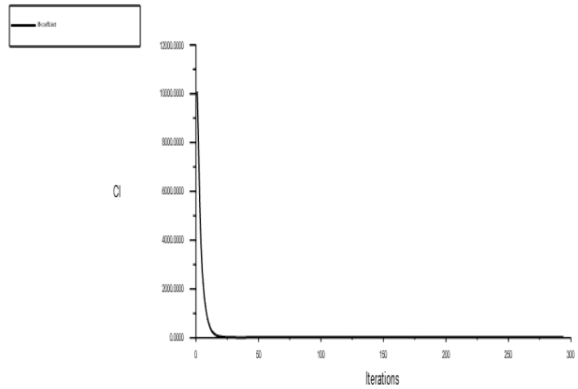

Figure: 0º AOA

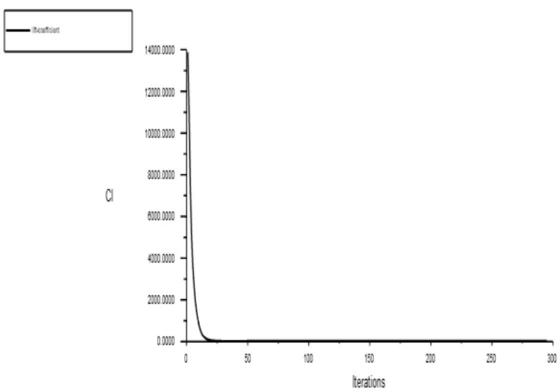

Figure: 2.5º AOA

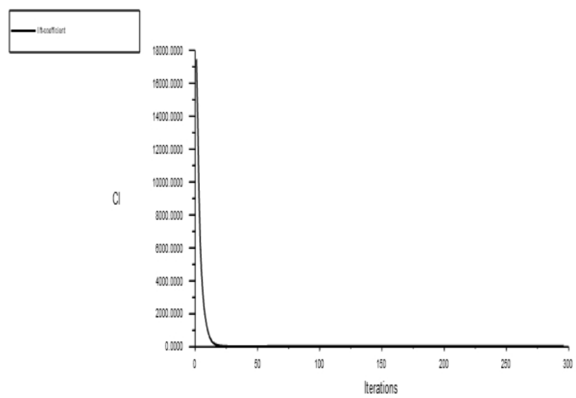

Figure: 5º AOA

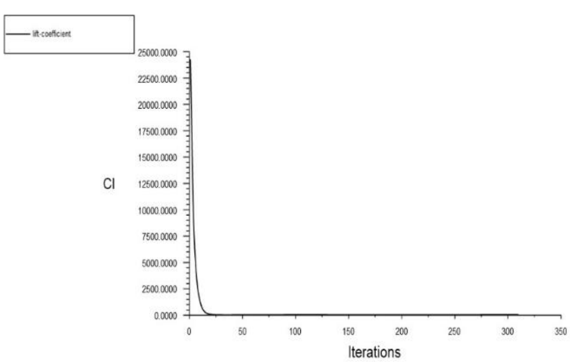

Figure: 10º AOA

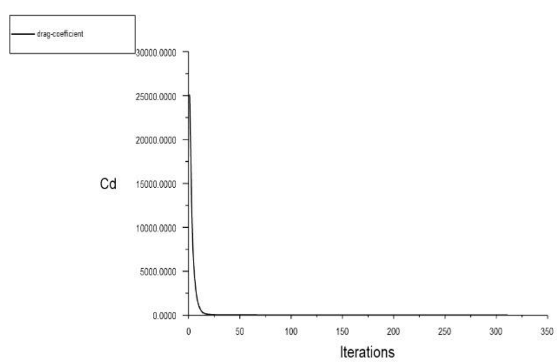

Figure: 15º AOA

Winglet-2 Blade Lift Coefficient Plot at Different Angle of Attack

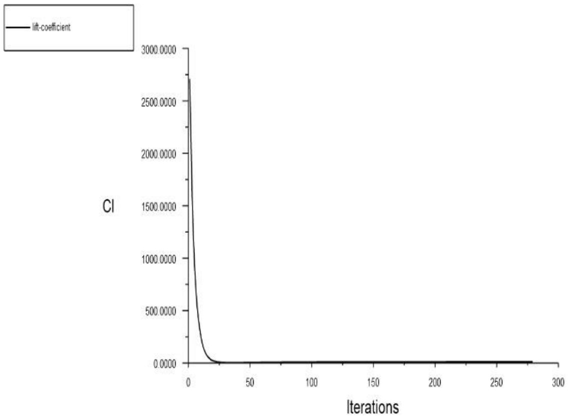

Figure: -5º AOA

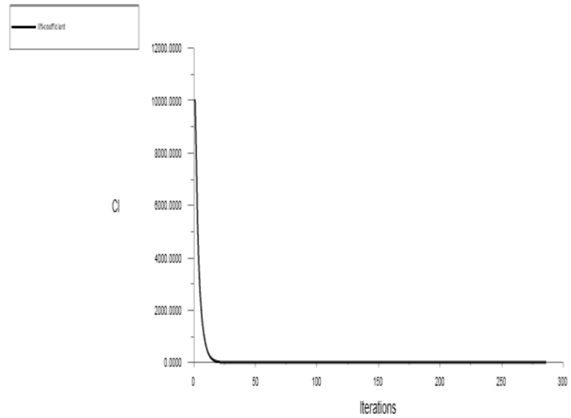

Figure: 0º AOA

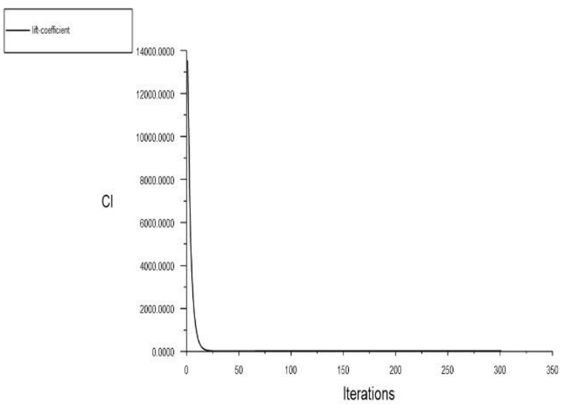

Figure: 2.5º AOA

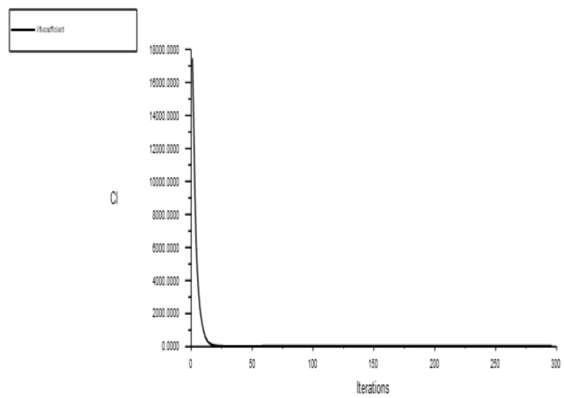

Figure: 5º AOA

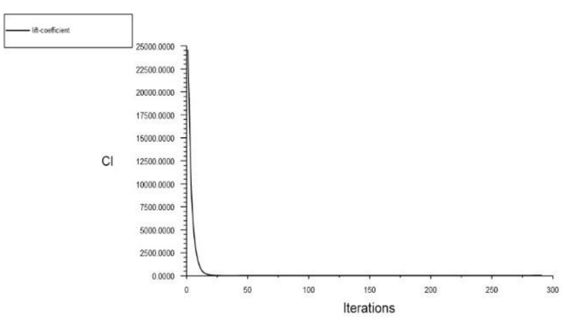

Figure: 10º AOA

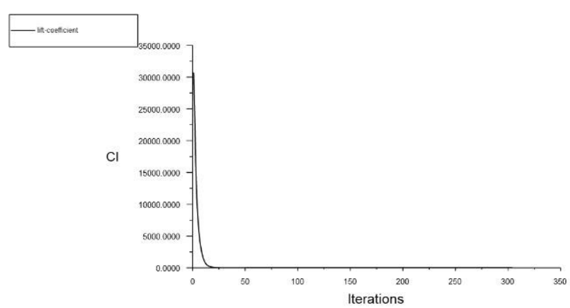

Figure: 15º AOA

Winglet-2 Blade Drag Coefficient Plot at Different Angle of Attack

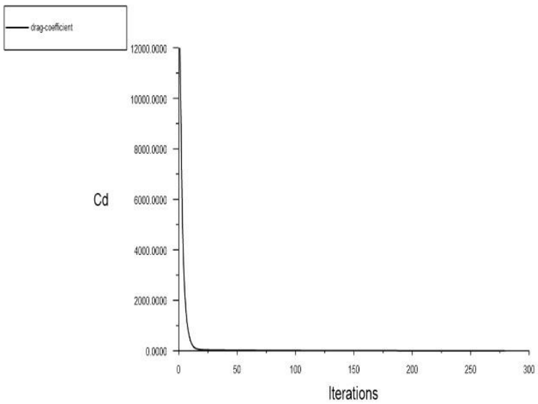

Figure: -5º AOA

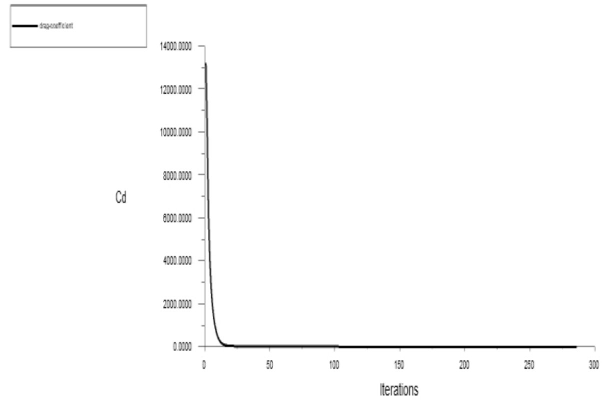

Figure: 0º AOA

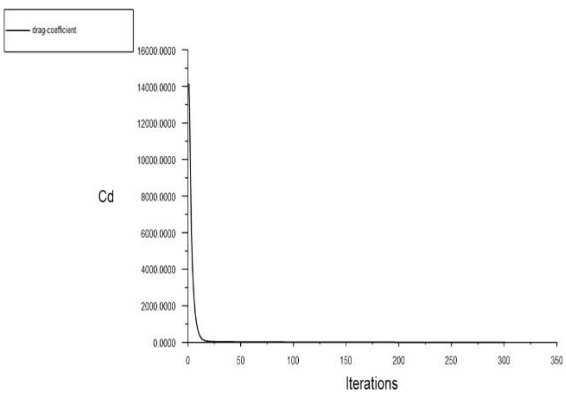

Figure: 2.5º AOA

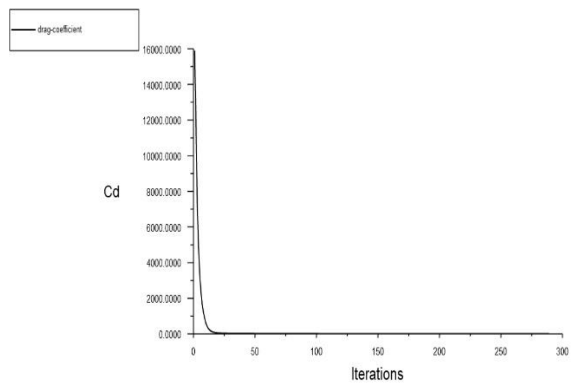

Figure: 5º AOA

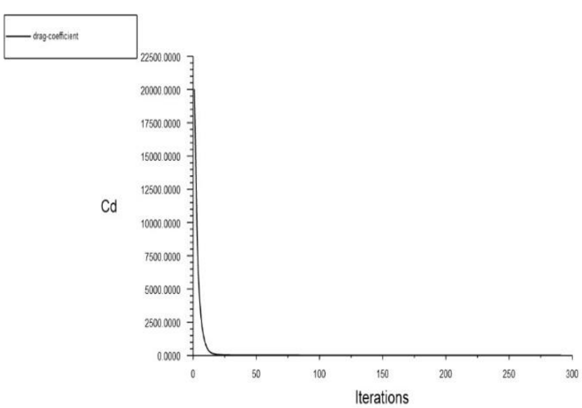

Figure: 10º AOA

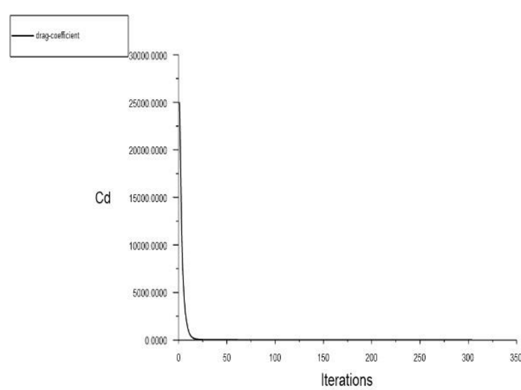

Figure: 15º AOA

Winglet-3 Blade Lift Coefficient Plot at Different Angle of Attack

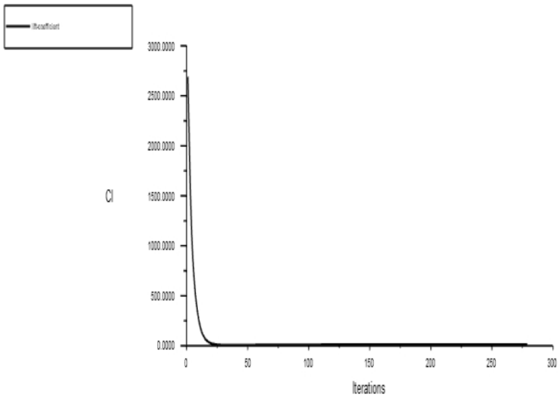

Figure: -5º AOA

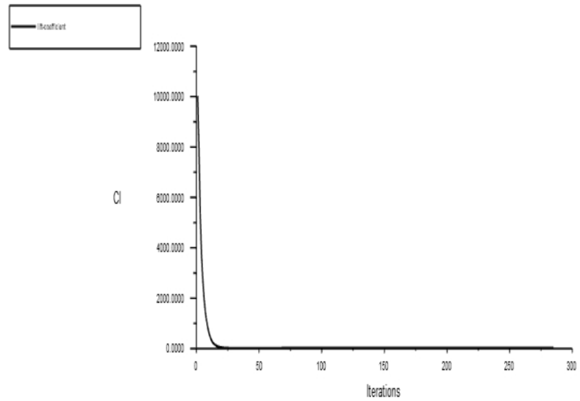

Figure: 0º AOA

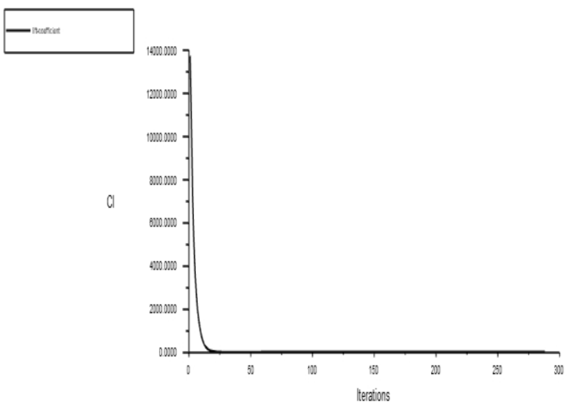

Figure: 2.5º AOA

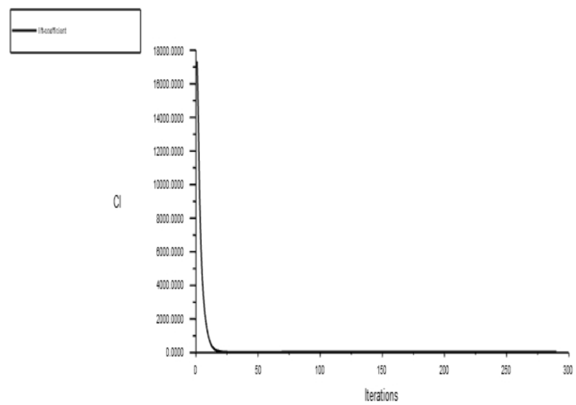

Figure: 5º AOA

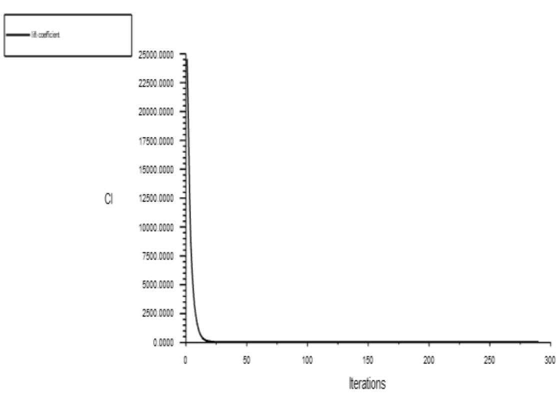

Figure: 10º AOA

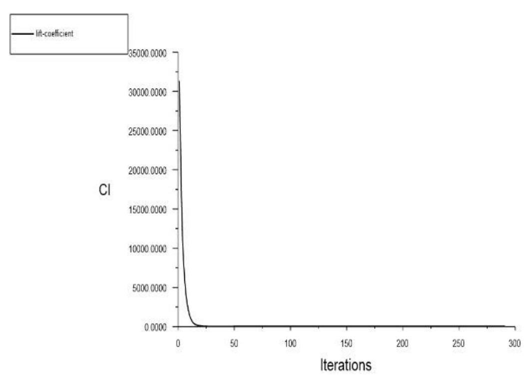

Figure: 15º AOA

Winglet-3 Blade Drag Coefficient Plot at Different Angle of Attack

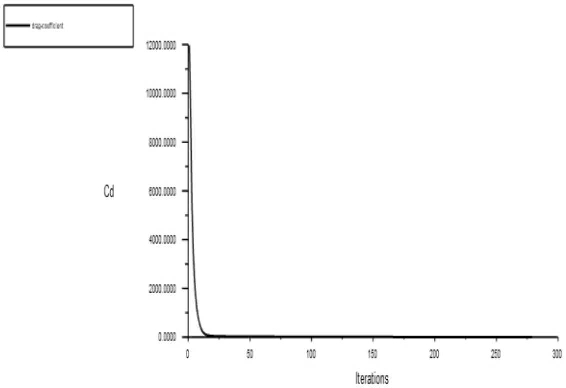

Figure: -5º AOA

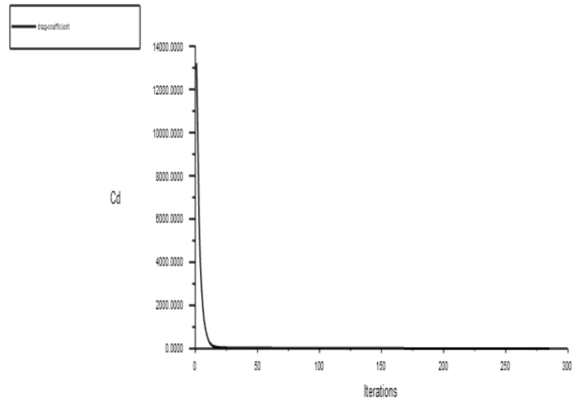

Figure: 0º AOA

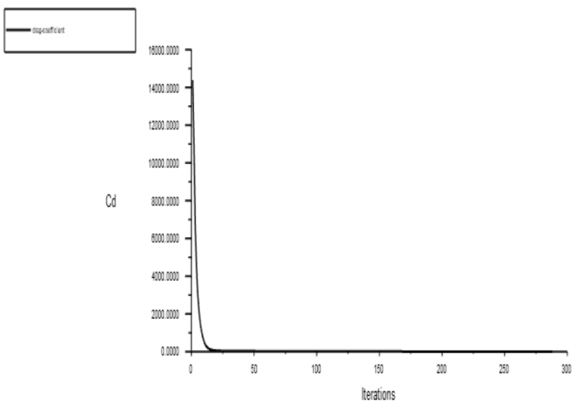

Figure: 2.5º AOA

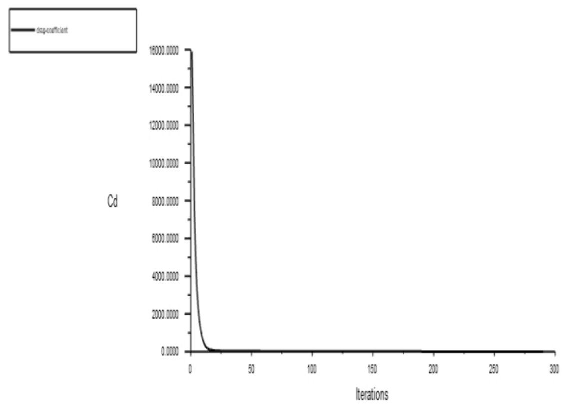

Figure: 5º AOA

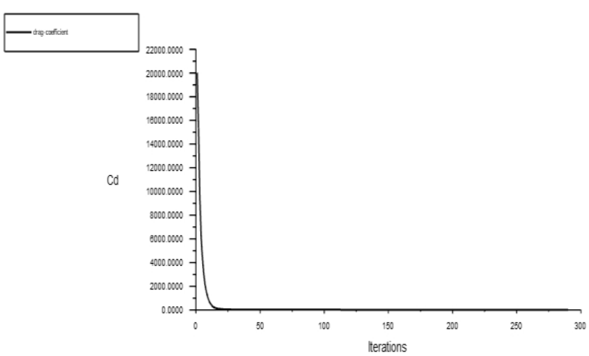

Figure: 10º AOA

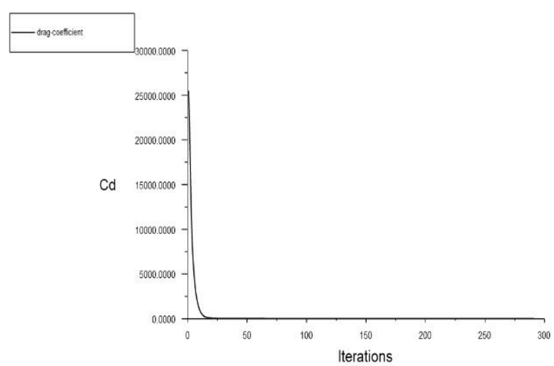

Figure: 15º AOA

Winglet-4 Blade Lift Coefficient Plot at Different Angle of Attack

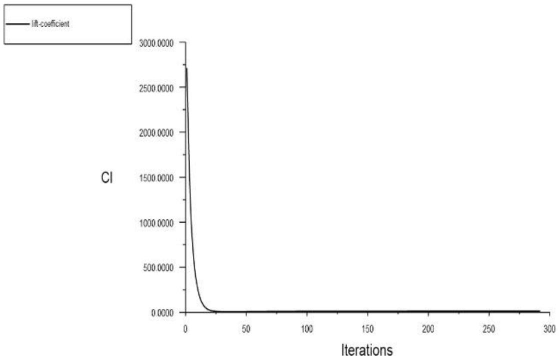

Figure: -5º AOA

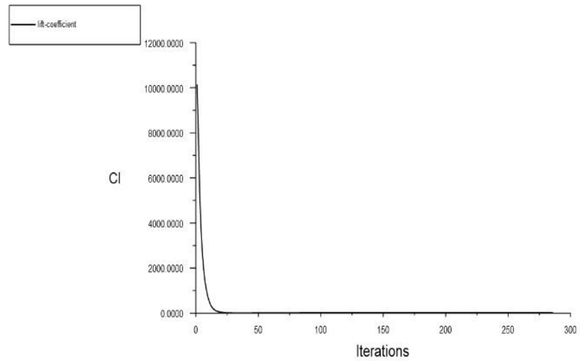

Figure: 0º AOA

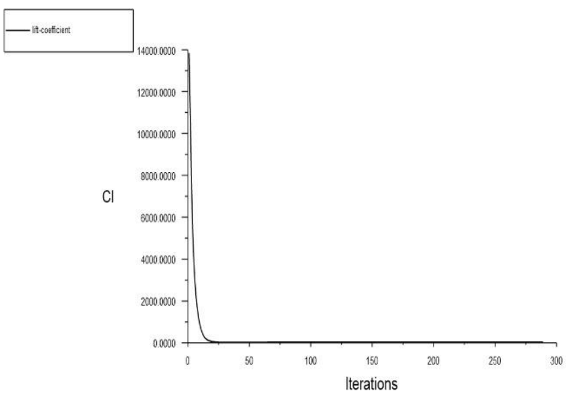

Figure: 2.5º AOA

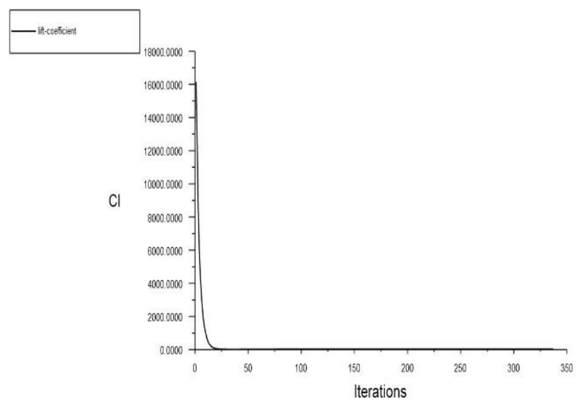

Figure: 5º AOA

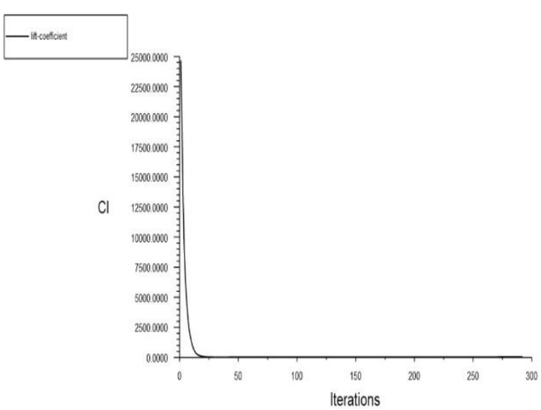

Figure: 10º AOA

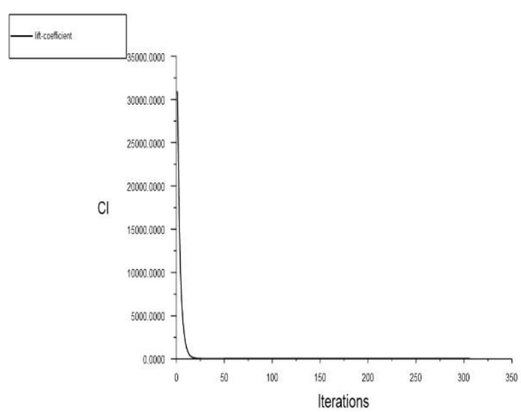

Figure: 10º AOA

Winglet-4 Blade Drag Coefficient Plot at Different Angle of Attack

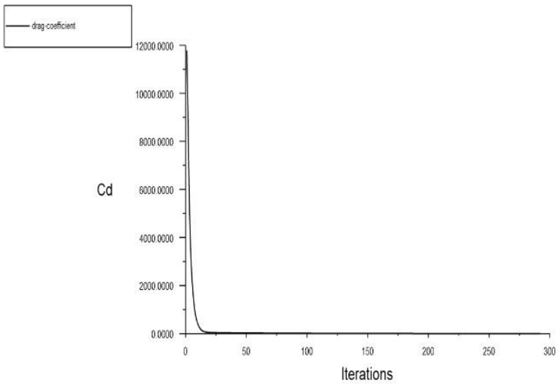

Figure: -5º AOA

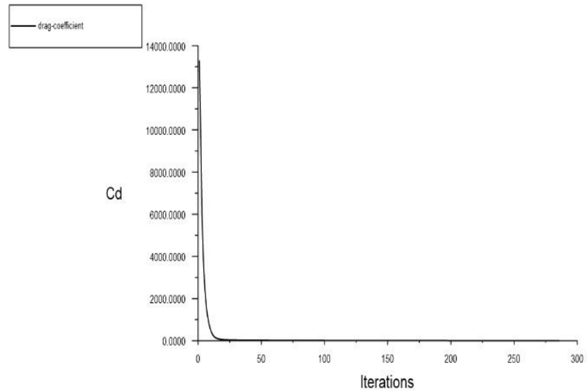

Figure: 0º AOA

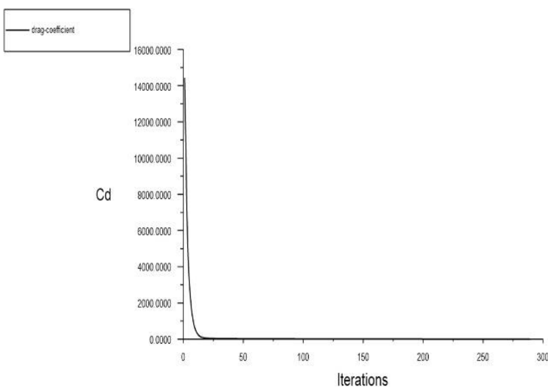

Figure: 2.5º AOA

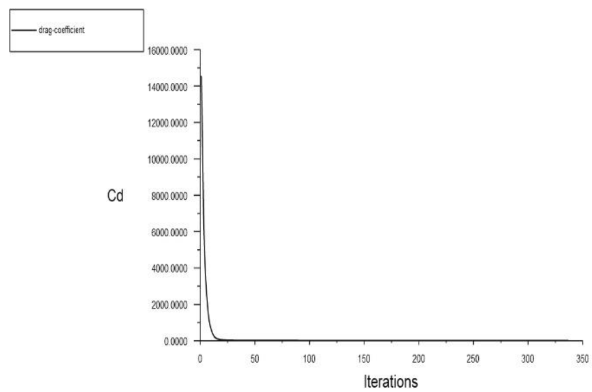

Figure: 5º AOA

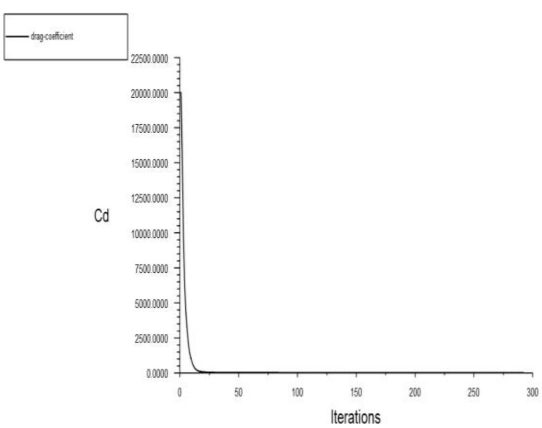

Figure: 10º AOA

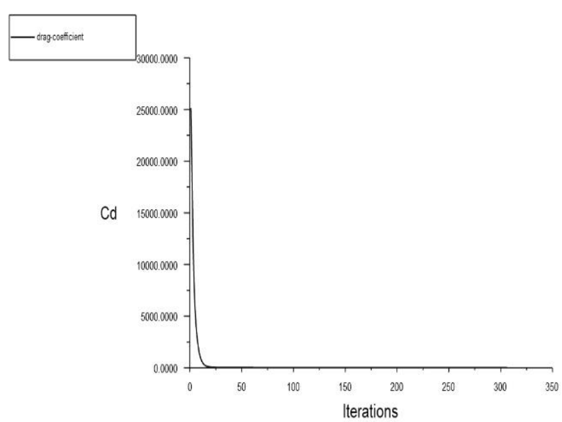

Figure: 15º AOA

Winglet-5 Blade Lift Coefficient Plot at Different Angle of Attack

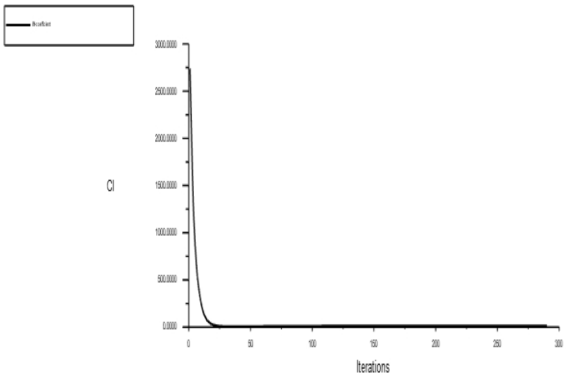

Figure: -5º AOA

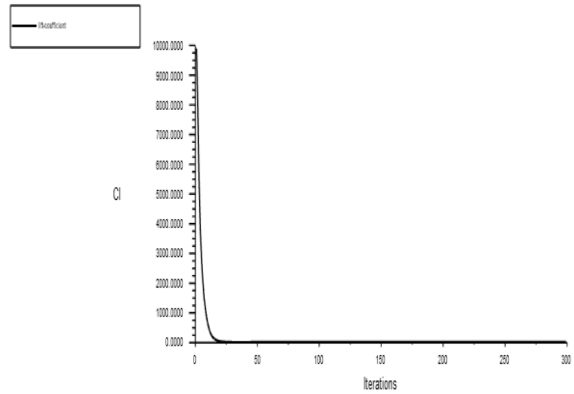

Figure: 0º AOA

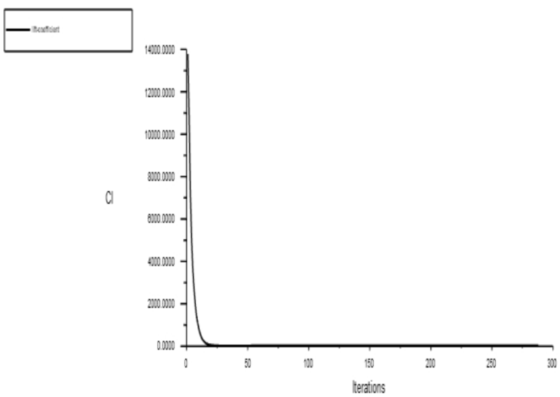

Figure: 2.5º AOA

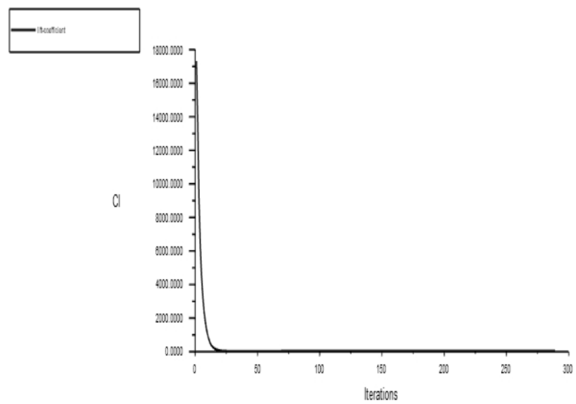

Figure: 5º AOA

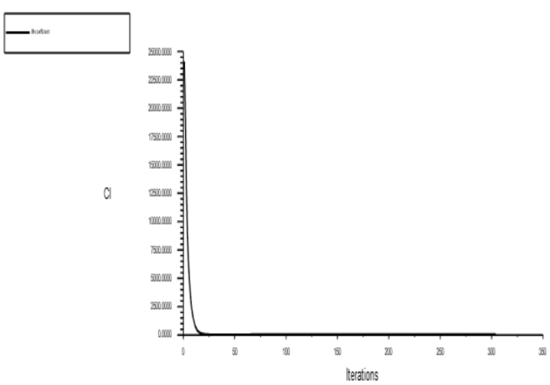

Figure: 10º AOA

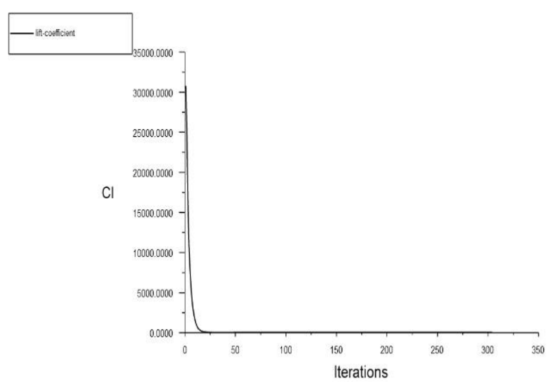

Figure: 15º AOA

Winglet-5 Blade Drag Coefficient Plot at Different Angle of Attack

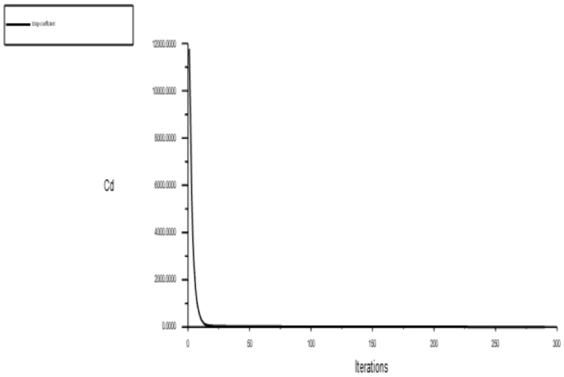

Figure: -5º AOA

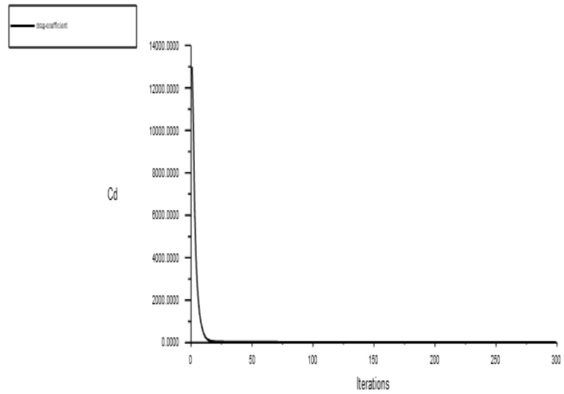

Figure: 0º AOA

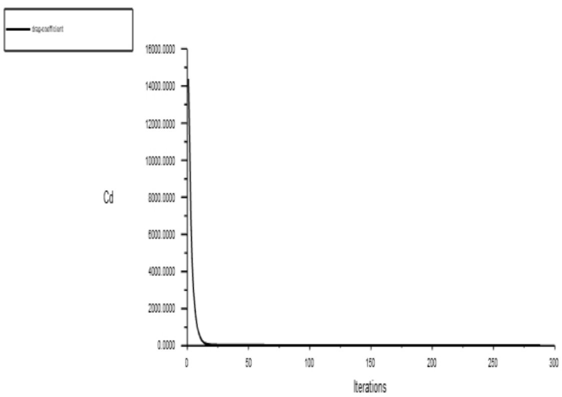

Figure: 2.5º AOA

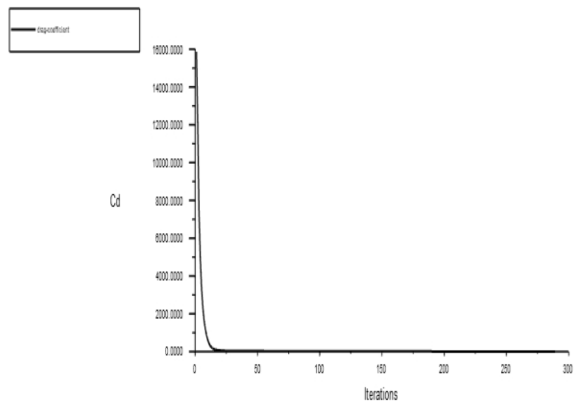

Figure: 5º AOA

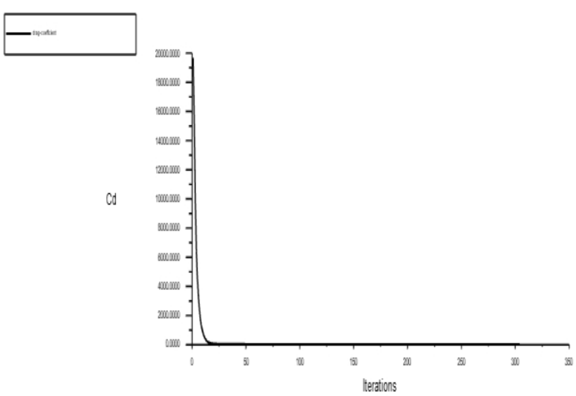

Figure: 10º AOA

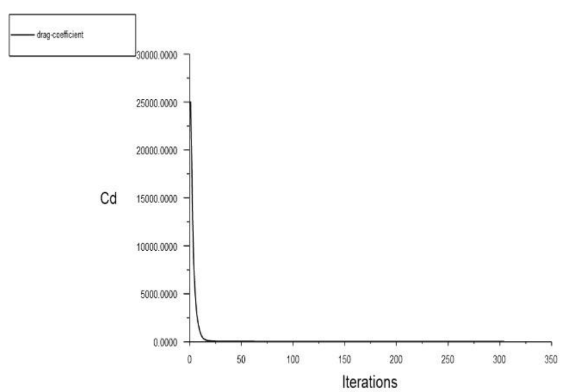

Figure: 15º AOA

Winglet-6 Blade Lift Coefficient Plot at Different Angle of Attack

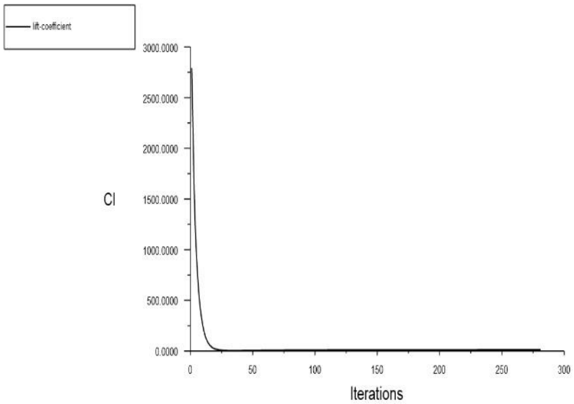

Figure: -5º AOA

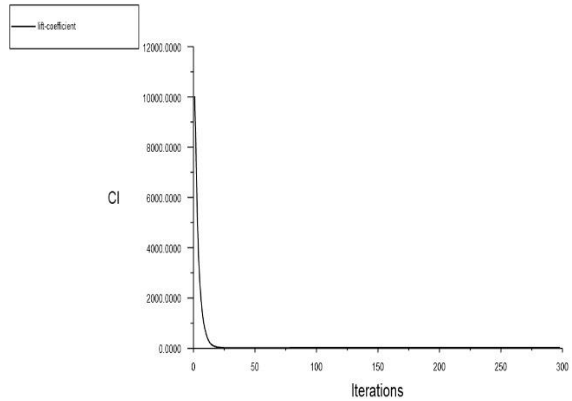

Figure: 0º AOA

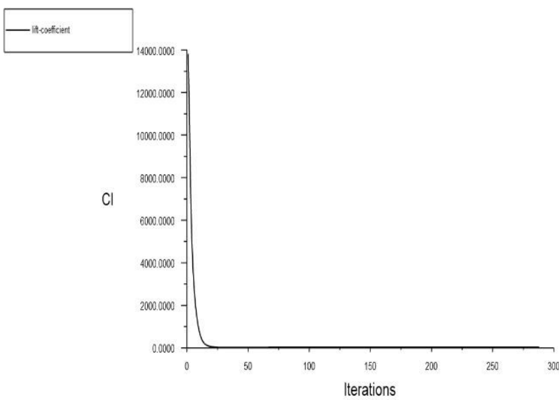

Figure: 2.5º AOA

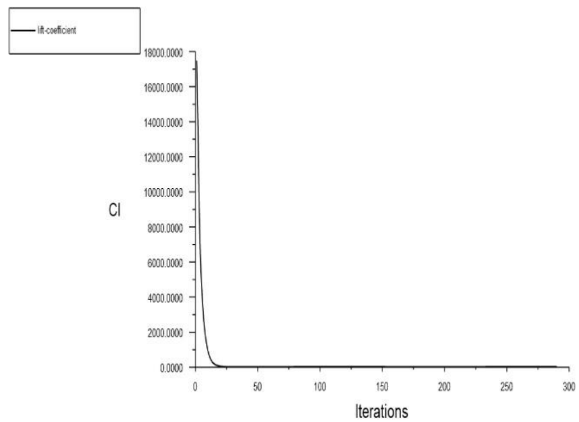

Figure: 5º AOA

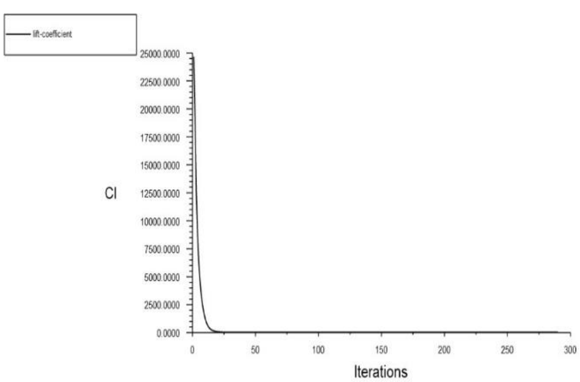

Figure: 10º AOA

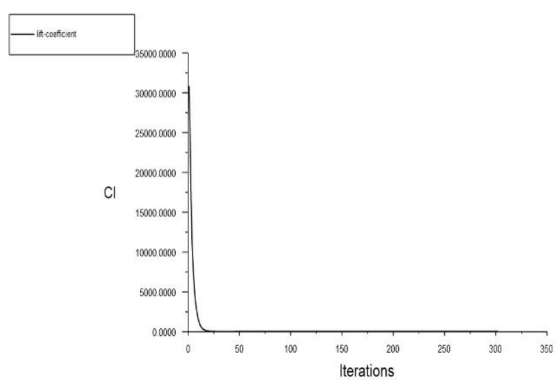

Figure: 15º AOA

Winglet-6 Blade Drag Coefficient Plot at Different Angle of Attack

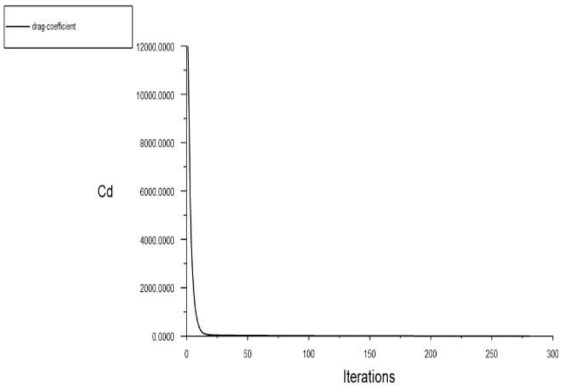

Figure: -5º AOA

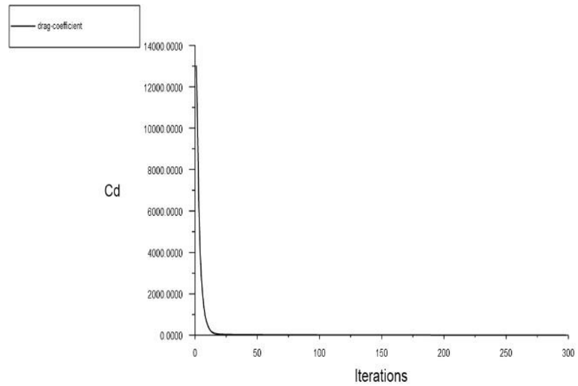

Figure: 0º AOA

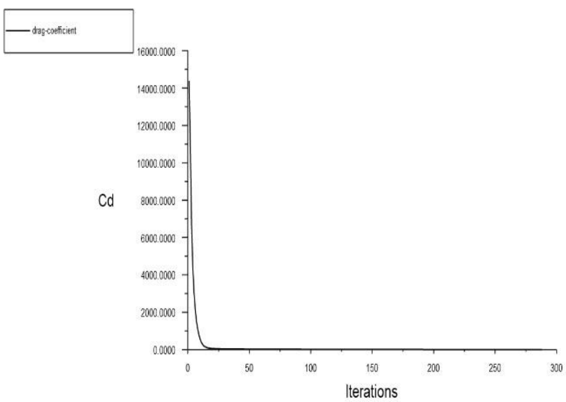

Figure: 2.5º AOA

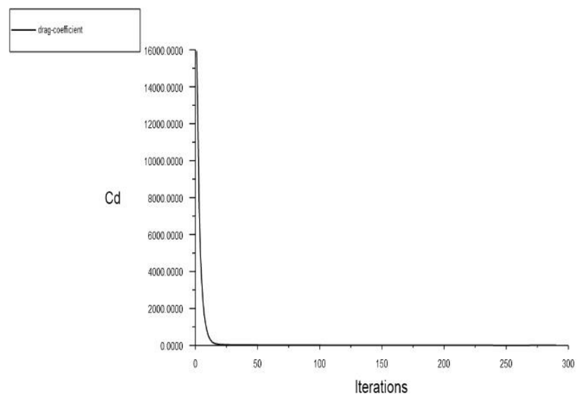

Figure: 5º AOA

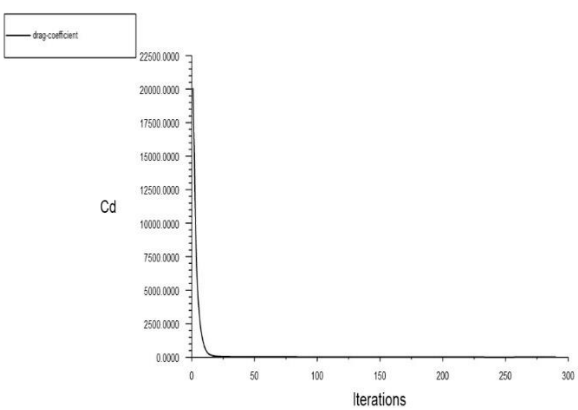

Figure: 10º AOA

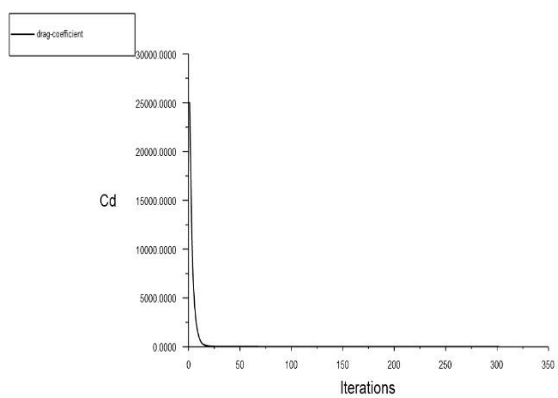

Figure: 15º AOA